Properties and Phase Transitions in Lead Free Piezoelectrics: $(K,Na)NbO_3$-$LiNbO_3$ and $(Bi,Na)TiO_3$-$BaTiO_3$

THÈSE N^{O} 4528 (2009)

PRÉSENTÉE LE 6 NOVEMBRE 2009

À LA FACULTÉ SCIENCES ET TECHNIQUES DE L'INGÉNIEUR

LABORATOIRE DE CÉRAMIQUE

PROGRAMME DOCTORAL EN SCIENCE ET GÉNIE DES MATÉRIAUX

ÉCOLE POLYTECHNIQUE FÉDÉRALE DE LAUSANNE

POUR L'OBTENTION DU GRADE DE DOCTEUR ÈS SCIENCES

PAR

Naama KLEIN

acceptée sur proposition du jury:

Prof. P. Stadelmann, président du jury
Prof. N. Setter, Prof. D. Damjanovic, directeurs de thèse
Dr M. Demartin Mäder, rapporteur
Dr S. Mischler, rapporteur
Prof. J. Trodahl, rapporteur

ÉCOLE POLYTECHNIQUE
FÉDÉRALE DE LAUSANNE

Suisse
2009

In memory of Savta Irma, Savta Tobi, Saba Miki and Saba Andor

My grandparents who survived hell

This is our revenge

Abstract

Piezoelectric materials are used in a wide range of applications, with lead zirconate titanate (PZT) ceramics being the dominant family of materials, due to high piezoelectric coefficients, dielectric permittivity and coupling factors. The high properties have been found in compositions in the proximity of a morphotropic phase boundary (MPB). The MPB exhibits a weak temperature dependence so that the stability of the properties is attained over a large temperature range. However, environmental problems rising from the toxicity of lead have driven scientists around the world to search for lead free piezoelectric materials. These new materials should exhibit properties comparable to those of PZT and the efforts are at the present concentrated on solid solutions with an MPB.

In this thesis an emphasis was made on constructing the phase diagrams and detecting an MPB in two of the most promising families of lead-free solid solutions: bismuth sodium titanate based and potassium sodium niobate based ceramics and single crystals. By investigating the structure of the phases, using X-ray and neutron diffractions and Raman spectroscopy, and measuring the dielectric and piezoelectric properties at temperatures from -266°C to 550°C, the phase transitions were assigned and phase diagrams constructed.

Both systems $(1-x)(Bi_{0.5}Na_{0.5})TiO_3$-$xBaTiO_3$ $(0\leq x\leq 0.09)$ (BNBT) and $(1-x)(K_{0.5}Na_{0.5})NbO_3$-$xLiNbO_3$ $(0.02\leq x\leq 0.1)$ (KNLN), reveal similar MPBs to the one found for PZT. However, in PZT the MPB is pseudovertical up to about 350°C whereas the MPB in BNBT is vertical only till 75°C and in KNLN is till -50°C. This difference in the temperature stability range is crucial in most applications.

Other interesting findings in the BNBT phase diagram correspond to the phase sequence at the temperature range from 200 to 300°C, where ferroelectric phase transforms into a mixed phase (antiferroelectric or paraelectric) with polar regions. As temperature rises, the polar regions gradually disappear.

Whereas dielectric and piezoelectric properties of BNBT could compete with those of PZT in some compositions, and fairly simple processing of the ceramics is used, the fabrication of KNLN ceramics has shown to be complex and reproducible properties difficult to obtain. Even after the critical processing conditions were identified in this thesis, and reproducibility was achieved, properties were significantly lower than for PZT.

Exceptional values of the thickness coupling coefficients were measured on potassium niobate (KN) and KNLN single crystals rotated away from the Z axis by θ=45° about the orthorhombic Y axis, $[001]_C$-cut. Monodomain and domain-engineered single crystals cut at this angle showed very high coefficients ($k_t \leq 70\%$), which are extremely stable over a large temperature range and after thinning to thickness below 60μm. Together with low permittivity, these properties make KN single crystals a good candidate for high-frequency applications. The higher permittivity of KNLN makes it an attractive crystal for applications at lower frequencies.

Another possible application of lead free piezoelectrics could be in biological systems. For this reason, preliminary *in-vitro* biocompatibility study of KNLN and PZT ceramics was conducted, showing similar microscopic attachment of cells to the two ceramics and slightly lower viability values when compared to non coated tissue culture plates. Laboratory attempts to introduce KNLN ceramics as an implant in the mineral of the bone, hydroxyapatite (HA), ended with a strong chemical reaction between the two. However, some piezoelectric response could be measured from the composite of HA and KNLN.

Key words: Lead free piezoelectric, ceramic, single crystals, morphotropic phase boundary (MPB), phase diagram

Résumé

Les matériaux piézoélectriques sont utilisés dans une vaste gamme d'applications; les céramiques à base de titanate-zirconate de plomb (PZT) constituent la famille la plus importante de ces matériaux, grâce à leurs coefficients piézoélectriques, leur permittivité diélectrique et leurs facteurs de couplage élevés. Les propriétés les plus favorables ont été trouvées dans des compositions proches de la frontière de phase morphotropique (MPB). La MPB n'est que faiblement dépendante de la température, de sorte que la stabilité de ses propriétés se maintient sur une large gamme de températures. Cependant, les problèmes environnementaux liés à la toxicité du plomb ont conduit les scientifiques du monde entier à rechercher des matériaux piézoélectriques ne contenant pas de plomb. Ces nouveaux matériaux devraient posséder des propriétés comparables à celles du PZT et les efforts sont actuellement orientés vers des solutions solides contenant une MPB.

Dans cette thèse l'accent est mis sur la construction de diagrammes de phases et la détection de la MPB dans deux des familles les plus prometteuses de solutions solides sans plomb : les céramiques et monocristaux à base de titanate de sodium et de bismuth et ceux à base de niobate de potassium et de sodium. Les conditions de transition de phases ont été déterminées et les diagrammes de phases construits suite à l'étude des structures par diffraction de rayons X et diffraction de neutrons, par spectroscopie de Raman et mesure des propriétés diélectriques et piézoélectriques à des températures situées entre -266° et 550°C.

Les deux diagrammes, (1-x) (Bi0.5Na0.5) TiO3-xBaTiO3 (0=x=0.09) (BNBT) et (1-x) (K0.5Na0.5) NbO3-xLiNbO3 (0.02=x=0.1) (KNLN), révèlent des MPB proches de celle trouvée pour PZT. Cependant, la MPB du PZT est pseudo-verticale jusqu'à environ 350°C, tandis que la MPB du BNBT est vertical seulement jusqu'à 75°C et la MPB du KNLN seulement jusqu'à -50°C. Cette différence de stabilité sous diverses températures est cruciale dans la plupart des applications.

Le diagramme des phases du BNBT présente la propriété intéressante d'une séquence entre 200° et 300°C où la phase ferroélectrique se transforme en une phase mixte (antiferro-électrique, ou para-électrique) à régions polaires. Ces régions disparaissent graduellement avec l'augmentation de la température.

Alors que les propriétés diélectriques et piézoélectriques du BNBT s'avèrent équivalentes à celle du PZT dans certaines compositions et lorsque le traitement des céramiques est relativement simple, l'élaboration de céramique à base de KNLN à propriétés stables est complexe. Quand bien même les conditions d'élaboration des céramiques à propriétés reproductibles ont été définies dans cette thèse, leurs propriétés se sont avérées significativement inférieures à celle du PZT.

Des valeurs de coefficients de couplage exceptionnellement éleveés ont été mesurées sur le niobate de potassium (KN) et les monocristaux simples KNLN orientés hors de l'axe Z à θ=45° avec l'axe Y orthorhombique. Les monocristaux à mono-domaine et domain-engineered coupés à cet angle montrent un coefficient très élevé ($k_t \leq 70\%$), qui est extrêmement stable sur de grandes variations de température, même après une coupe d'épaisseur d'environ 60μm. Ajoutées à une faible permittivité, ces propriétés font des monocristaux KN de bons candidats aux diverses applications sous fréquences élevées. La permittivité plus élevée du KNLN rend ce cristal particulièrement intéressant dans des applications à plus basses fréquences.

Une autre application possible des piézoélectriques sans plomb pourrait porter sur des systèmes biologiques. Des études préliminaires in-vitro de biocompatibilité ont été menées, montrant le rattachement microscopique de cellules avec ces deux céramiques dont les valeurs de viabilité sont légèrement inférieures en comparaison à des cultures tissulaires. Des essais en laboratoire d'implantation de céramiques KNLN dans le minéral de l'os, hydroxyapatite (HA), ont débouché sur une forte réaction chimique entre les deux. Cependant, une faible réponse piézoélectrique peut être mesurée du composé de HA et KNLN.

Mots-clés: piézoélectrique sans plomb, céramique, monocristal, frontière de phase morphotropique (MPB), diagramme de phase

Acknowledgments

The work presented in this thesis was conducted over four and a half years. During this time I moved to a foreign country, learned a new language, spent various times in additional three laboratories, traveled in fourteen countries and conducted research. Along this challenging and exciting way, I was fortunate to receive the assistance of many.

I am grateful to Prof. Nava Setter, my thesis director, who offered me the opportunity of working with the top scientists of our field, in the best laboratory conditions. In addition, I am thankful for the professional discussions and the nice everyday conversations in Hebrew.

I would like to express my deep gratitude to Prof. Dragan Damjanovic, my thesis director, for sharing with me his huge knowledge with infinite patience and kindness, for the educating discussions and inputs, for the technical support and for the wonderful, hilarious anecdotes. I cannot imagine a better mentor than you.

I would like to thank my office-mates and friends Prof. Tomoaki Yamada, Dr. Roman Gysel and (soon to be Dr.) Jin Wang for the delightful ambiance during more than three years, for your friendship and the professional, fruitful discussions and constant support. I thank Dr. Alexandra Sarabando de Carvalho and Egidius Rwenyagila for the pleasant atmosphere while sharing the office with me in the past year.

I am thankful to the former and current LC members for the companionship and help, especially on the difficult early days in a foreign country: Dr. Marko Budimir, Dr. Matthew Davis, Dr. Su Dong, Dr. Guido Gerra, Dr. Tomas Sluka, Dr. Scott Harada, Dr. Janine Conde, Sebastian Riester, Dr. Viktor Porokhonskyy, Dr. Yongli Wang, Dr. Andy Noeth, Li Jin, Dr. Arsen Sukiasyan, Dr. Tadej Rojac, Dr. Guochu Deng, Dr. Vladimir Sherman, Dr. Alexander (Sasha) Tagantsev, Dr. Enrico Colla, Dr. Igor Stolitchnov, Prof. Paul Muralt, Dr. Marco Cantoni, Dr. Cosmin Sandu, Yan Yan,

Dr. Samuel Rey-Mermet, Dr. Evelyn Hollenstein, Evgeny Milyutin, Alvaro Artieda, Maxim Gureev, Mahamudu Mtebwa and Monika Iwanowska.
I thank our lab secretaries Eva Favre and Yuko Kagata Spitteler for the kind help in all administration issues, and our technicians Lino Olivetta and Jacques Castano for their technical help.

I thank my collaborators abroad for their significant contributions and their kind hospitality: Prof. Joe Trodahl from University of Wellington in New Zealand, Dr. Daniel Rytz from FEE in Germany, Dr. Brahim Dkhil from Ecole centrale Paris in France, Prof. Jurgen Roedel and Eva Anton from University of Darmstadt in Germany and Dr. Martin Kuball from University of Bristol in the UK.

I thank the jury of my thesis: Prof. Pierre Stadelmann, Dr. Stefano Mischler, Dr. Marlyse Demartin Maeder and Prof. Joe Trodahl.

I would like to thank the wonderful friends I met during my time here: Ori Alkalay, Tal Von der Valde, Dr. Mor Mishkovsky, Simone Chiesa, Dr. Iva Tkalcec, Dr. Stuart Jackson, Severine Louis, Dr. Jean and Tikva Neyroud, Romain Humbert, Dr. Fred Didier and Dr. Harm Cronie. Life would seem very pale without you.

I would like to thank my great friends from back home for sending me their support all this time: Osnat Shaposhnikov, Liat Ben Yosef, Oz and Ornit Lavi, Nira Rabin, Dr. Tehila Gross and the Lesman family.

I would especially like to thank Yael (Yaya) Neyroud and Dr. Ayelet (Ayeli) Lesman for their friendship, love and support, which have no limits. I owe you more than I could ever pay you back.

Finally, I thank my family: my parents Eva and Naphtali, my brothers Nadav and Eyal, my sisters-in-low Marit and Inbal, and my amazing nieces and nephews: Shira, Tama, Eilon and Dotan. You have been my back when I doubted my strength and the shoulder I could lean on in good and bad times. I could never have done any of it without you on my side. You are my heart and soul.

Contents

Chapter 1 - Introduction

The use of piezoelectric materials today covers vast areas of applications, including fuel injection actuators, motors, printing machines, micropositioning systems, ultrasonic transducers and more[1]. Lead zirconate titanate ceramics have been the dominant piezoelectric material in these applications for a long time due to high piezoelectric coefficients, dielectric permittivity and coupling factors[2].

Lead is considered as a toxic element[3-5] and is released into the environment during calcinations and sintering of PZT, and hard machining of PZT components. In addition, recycling and waste disposal of lead-containing devices could be hazardous for the health and environment. As a consequence, in 2003 the European Union included lead zirconate titanate in its legislature as hazardous substance[6, 7]. However, as there are presently no lead-free replacements for PZT, the material is exempted from the ban for medical and electronic applications until adequate replacement can be found. This decision is reviewed periodically.

A major effort has been put in recent years in the development of lead free piezoceramics, which would compete and replace lead based materials. The families of bismuth based materials as well as potassium sodium niobate materials, appear promising to substitute lead zirconate titanate in at least part of the application range.

1.1. Piezoelectric materials

1.1.1. Piezoelectricity and ferroelectricity

Piezoelectrics are a family of organic and inorganic materials, and even biological matter, that hold the ability to translate linearly mechanical stress into electric charge and vice versa. Materials exhibiting piezoelectricity are non-centrosymmetric[1], in which electric dipole moments can be induced as a result of applied stress.

Only in materials belonging to the subgroup of pyroelectrics, dipoles are created spontaneously in the material even in the absence of external field. In ferroelectrics, a subgroup of pyroelectrics, these dipoles can be switched by an electric field or stress (poling).

One of the most utile crystalline structures is perovskite[2], of the chemical composition ABO_3. The structure is a network of corner-linked oxygen octahedra, with the smaller cation filling the octahedral holes (A-site) and the larger cation filling the dodecahedral holes[8] (B-site) (Figure 1-1). Dipole moments cause a distortion of the cubic perovskite unit cell along one of the [100], [110], [111] and [hk0] directions, defining several phases: tetragonal, orthorhombic, rhombohedral and monoclinic, respectively.

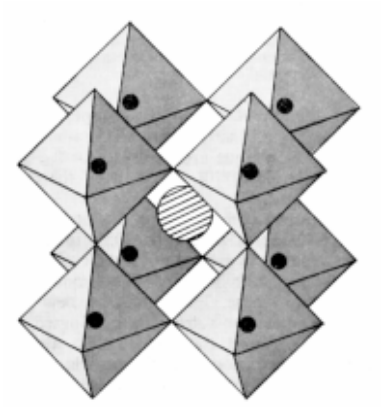

Figure 1-1 - Perovskite structure with chemical formula ABO_3. A site cations are presented by the black circles, B site cation by the hatched circle and the oxygen anions are at the vertices of the octahedra[8]

Piezoelectric and ferroelectric materials take an important role in many applications, such as sensors, actuators and transducers, which integrate in a variety of disciplines ranging from medical instrumentation to information systems, communication and many more.

1.1.2. Lead containing ceramics – PZT and the morphotropic phase diagram

Lead zirconate titanate, $Pb(Zr_xTi_{1-x})O_3$, (PZT) is a solid solution of perovskite lead titanate and lead zirconate displaying very high dielectric and piezoelectric properties in certain range of compositions (Figure 1-2). It has been shown that ions with a lone electron pair (two electrons paired by their anti-parallel spin in a filled subshell and not involved in chemical bonding), such as lead, form a dumbbell-like extrusion of the electron density on one side of the ion, increasing the polarizability and the distortion of the unit cell. These electrons tend to hybridize very easily with the orbitals of other ions, enhancing the ferroelectric distortion[9]. In addition, lead containing compounds tend to induce ionic dipole moments by elongating the "ionic radius" rather than keeping it spherically shaped[10]. Thus, the unit cell is distorted by the non-spherical ions even in the absence of an external electric field. Since the involved lead ions have high polarizability, the ferroelectric distortion tends to be large and thus the ferroelectric response and measured properties are high. These high ferroelectric properties, as well as the low cost and the facile processing turned PZT into the most widely used piezoelectric material.

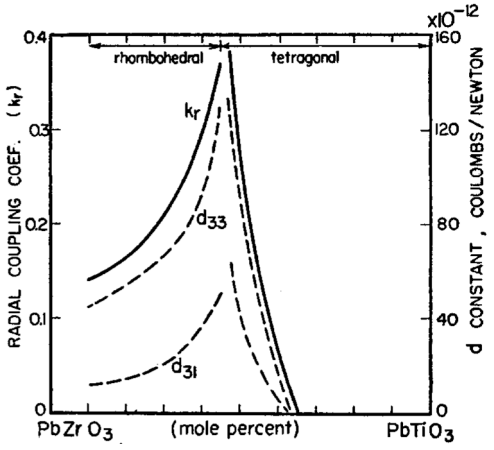

Figure 1-2 - Piezoelectric coefficients and coupling factor of PZT as function of the composition[11]

The phase diagram of PZT (Figure 1-3) has been studied for the last half century, presenting a nearly perpendicular phase boundary, called "morphotropic", at the composition range x=0.48-0.54, separating rhombohedral, monoclinic[12] and tetragonal phases.

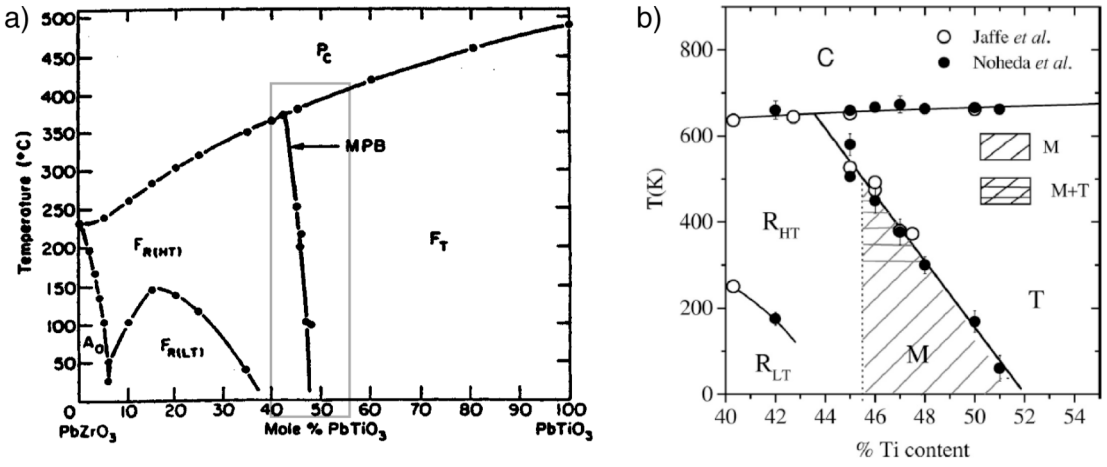

Figure 1-3 - (a) Phase diagram[2] of $PbZrO_3$-$PbTiO_3$ and (b) the enlarged area of the MPB[13]

Crossing any phase boundary involves re-orientation of the dipoles, which may result in depolarization. As opposed to a polymorphic phase transition (PPT), which involves temperature changes, the morphotropic phase boundary (MPB) depends only on changes in composition (Figure 1-4). As demonstrated by the dashed lines, temperature changes in the case of a PPT (Figure 1-4a), would lead to crossing of a phase boundary, as opposed to temperature changes in compositions near an MPB (Figure 1-4b). Hence, MPB is especially important for applications requiring a broad temperature range.

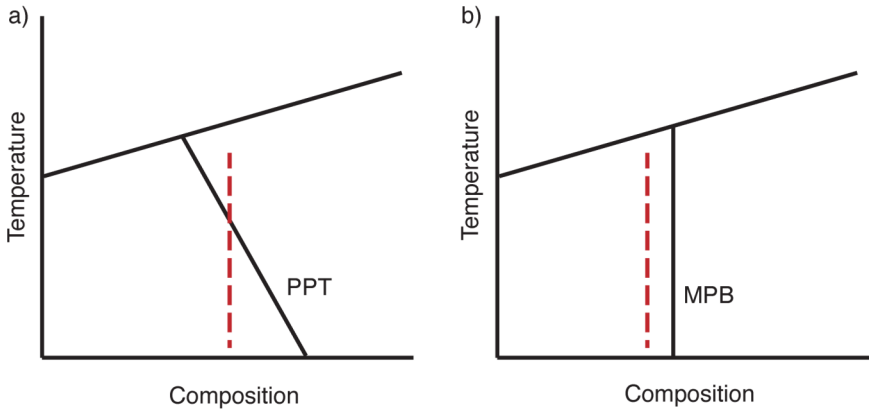

Figure 1-4 - (a) Polymorphic phase transition (PPT) and (b) morphotropic phase boundary (MPB)

High values of properties measured at the composition range x=0.48-0.54 of PZT[13-15] have been associated with the presence of a boundary separating two phases[16-18] (the type of boundary, PPT or MPB, is of no importance to the properties measured at a constant temperature). Calculations using the Landau-Devonshire-Ginzburg theory provide that the Gibbs free energy profile for the rhombohedral and tetragonal phases exhibits anisotropic flattening at the MPB[17, 19]. Therefore, the polarization vector could easily switch or rotate in the presence of a small field, between many different polarization orientations[20] (24 possible monoclinic orientations, 6 possible tetragonal orientations, and 8 rombohedral possible orientations).

The major drawbacks of PZT concerns its lead content. Lead toxicity has been recognized thousands of years ago and is well documented. Lead interferes with many enzyme systems of the body, thereby affecting the function of virtually every organ. Clinical manifestations of lead toxicity include symptoms referable to the central nervous system, the peripheral nervous system, the hematopoietic (blood) system, the renal system, and the gastrointestinal systems[21].

Lead poisoning occurs as a result of ingestion or inhalation of inorganic lead particles or through transdermal absorption of organic alkyl lead. Hence, environmental problems raise during the production and disposal of PZT ceramics.

Considering the large amount of applications using PZT, it is surprising that only little research was done on the toxicity of the ceramic product, since one could assume that lead in sintered PZT is stable and would not decompose to the

environment. Only one publication was found, presenting some results for biocompatibility of PZT plates[22]. In this research mouse fibrous-tissue were observed for their proliferation rate (production of new cells). Results show that PZT has little effect on the proliferation rate of cells compared to the control group, but the number of dead white cells increased with time, and the survival time of a cell was shortened extremely by the presence of PZT.

1.2. Motivation

The amount of electrical and electronic equipment waste generated in the world is rapidly growing. Safe disposal of hazardous substances contained in these wastes is a major concern, therefore as of July 1st 2006 the European Parliament has adopted the directives WEEE (Waste Electrical and Electronic equipment) and RoHS (Restriction of the use of certain Hazardous Substances in electrical and electronic equipment) to prevent generation of new waste, and re-use or recycle electrical waste and electronic equipment. In order to protect human health and environment, the hazardous substances should be substituted by safe or safer materials[6, 7].

The RoHS applies to the specified categories of electrical and electronic equipment used in households and industries. Medical devices, monitoring and control instruments and spare parts for older devices are currently excluded. Hence, the use of lead containing materials in piezoelectric devices is still allowed in the EU, but will be prohibited as soon as practicable substitution is available. Activities to establish similar regulations are currently taking place in countries all over the world. Environmental friendly piezoelectric materials, which could compete with lead containing piezoceramics, are therefore needed.

Besides these societal and environmental concerns, lead based piezoelectrics pose several important scientific problems, including: is lead cation essential for large piezoelectricity, can lead free materials exhibit a vertical morphotropic phase boundary and is domain wall contribution in lead free materials as large as in lead based materials.

In this thesis two of the most promising ceramic lead-free systems, bismuth sodium barium titanate and potassium sodium lithium niobate, were studied. These systems were chosen because of their atomic and electronic similarity to lead (in case

of bismuth) and previously published results showing comparable properties to some lead containing piezoelectrics (in the case of potassium sodium lithium niobate).

Due to the importance of reproducibility of components during industrial manufacturing, and the diversity of published properties for potassium sodium lithium niobate ceramics, the ceramic processing of this system was addressed and modifications were studied.

Since phase sequences and types of phase boundaries have shown to highly influence properties in lead containing systems, the phase diagrams of both systems were constructed. Properties of both systems, ceramics and single crystals, were studied and discussed with regards to their phases. Extrinsic and intrinsic contributions were investigated in order to understand the origin of the piezoelectric properties.

In addition, lead free piezoelectrics could be used in biological implants, stimulating tissue growth in their surrounding, and as implanted sensors. For these potential applications, biological aspects of potassium sodium lithium niobate ceramics are discussed.

The results presented in this thesis are finally discussed with respect to lead containing systems.

1.3. Thesis plan

Figure 1-5 illustrates the correlation between the different chapters of this thesis:

Literature survey on recent developments in lead free piezoelectrics (BNT-BT and modified KNLN) is presented in the first part of chapter 2. The second part of this chapter introduces structure and piezoelectric properties of the bone and bone component, hydroxyapatite.

Basic terms and experimental techniques are presented shortly in chapter 3.

Chapter 4 and chapter 6 present properties measured on BNT-BT and KNLN ceramics, respectively. The data collected using X-Ray diffractions, hysteresis loops, dielectric properties (temperature and frequency dependent), resonance measurements and Raman spectroscopy were used to construct phase diagrams of both systems.

Chapter 5 presents the improvement of reproducibility in properties of KNLN ceramics, when modifications in sintering are used as opposed to the conventional processing.

High coupling coefficients of KN and KNLN single crystals are discussed in chapter 7. Temperature stability is demonstrated, appropriate for high frequency medical applications.

Chapter 8 presents preliminary results of *in-vitro* biocompatibility of KNLN and PZT. Following the encouraging results, chapter 9 discusses surface interactions between KNLN and hydroxyapatite.

Discussion on the results obtained from both systems with respect to PZT, the conclusions of the thesis and out look are given in chapter 10.

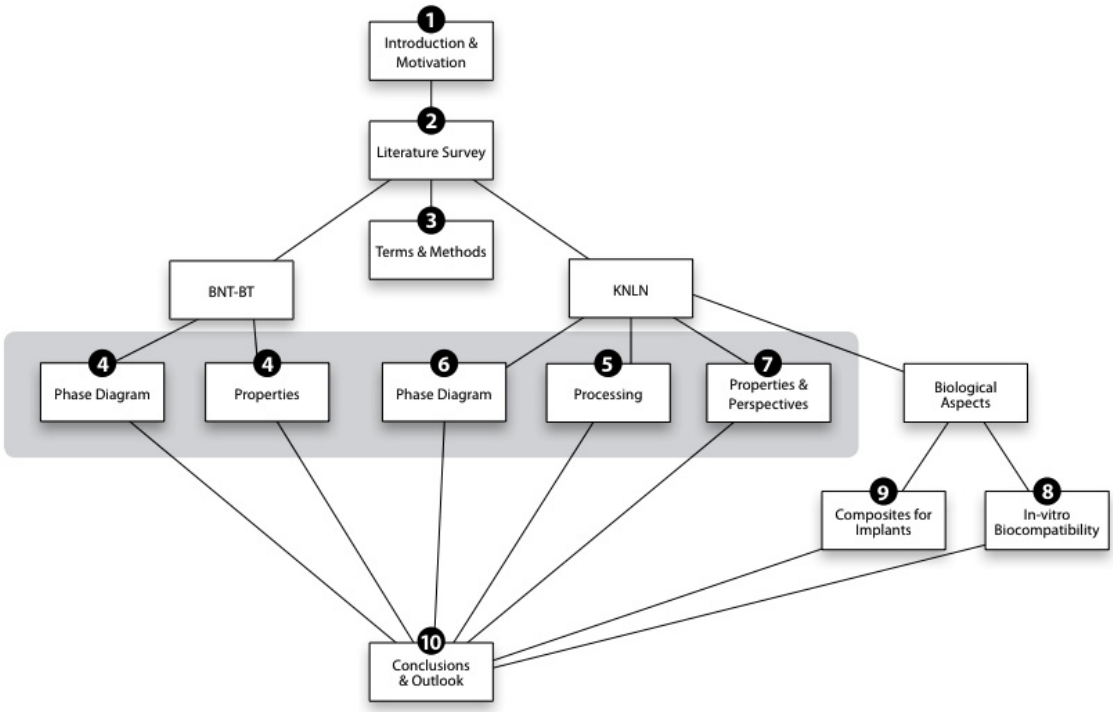

Figure 1-5 - Flow diagram illustrating the correlation between the different parts of the thesis

Chapter 2 - Literature survey

In this chapter, a literature survey is given presenting the updated knowledge on bismuth sodium barium titanate ceramics and potassium sodium niobate ceramics. In addition, a short introduction to piezoelectricity for implant applications is presented.

2.1. Lead free materials

Difficulties in recycling and disposal of devices containing lead, as well as environmental problems which rise during processing due to toxicity of lead oxide, provoked the hardening of legislations against lead containing materials in many countries (see Chapter 1).

Therefore, there is great need for lead free materials in the various applications. A good deal of work has been invested in number of materials, out of which the most promising properties were found in bismuth sodium titanate and potassium sodium niobate groups of materials.

2.1.1. Bismuth Sodium Titanate $(Bi,Na)TiO_3$ and Bismuth Sodium Barium Titanate $(Bi,Na,Ba)TiO_3$

As mentioned in section 1.1.2, lead containing materials are believed to exhibit good ferroelectric and piezoelectric properties due to both high polarizability (large radius and a high effective number of electrons) and a lone electron pair in the outer shell in Pb, which could hybridize with oxygen ions. One of the element that meets both requirements is bismuth. From the atomic point of view, bismuth containing compounds thus seem to be the most likely successors to lead based piezoelectrics[23]. It is interesting to note that bismuth is a non-toxic heavy metal that has practically no harmful effect on the living organisms[24-26].

Bismuth sodium titanate (BNT) is a perovskite type structure exhibiting a controversial sequence of phase transitions. Most papers agree on the following two transitions: at 530°C a transition from paraelectric cubic phase to paraelectric tetragonal phase takes place and below approximatly 200°C a ferroelectric rhombohedral phase is present. There is no controversy on the determined properties and nature of the high temperature and the low temperature phases, but many different views could be found concerning the nature of the transient phase, especially in the temperature range 200-320°C. At room temperature, BNT ceramics show the following piezoelectric properties[27]: P_r=33.3μC/cm^2, Ec=80 kV/cm, d_{33}=92pC/N, k_p=18.6% (definition of the different propertie in chapter 3).

The phase diagram of $(Bi_{0.5}Na_{0.5})_{1-x}Ba_xTiO_3$ (BNT-xBT) system was presented by Takanaka et al[28] (Figure 2-1), exhibiting a morphotropic phase boundary (MPB) between rhombohedral and tetragonal phases at x=0.06-0.07. However, this boundary is defined by only one point.

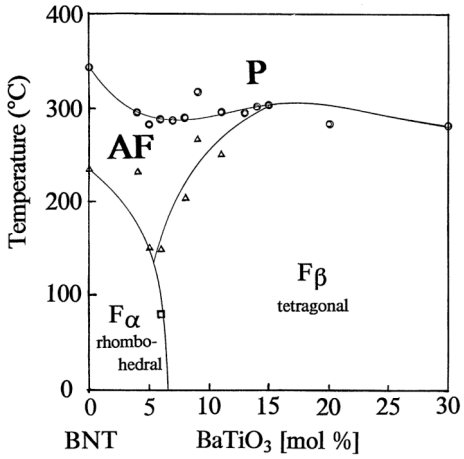

Figure 2-1 - Phase diagram of BNT-BT (F_α: ferroelectric rhombohedral, F_β: ferroelectric tetragonal, AF: antiferroelectric phase, P: paraelectric phase)[28]

A second phase diagram was later published by Hiruma et al[29] for the similar system barium sodium potassium, titanate (BNT-BKT) (Figure 2-2). This phase diagram was based on Takenaka's phase diagram, showing five phases as follows: phase I - ferroelectric rhombohedral, phase II - anti parallel domain configuration rhombohedral, phase III - pseudocubic ferroelectric relaxor, phase IV - ferroelectric tetragonal and phase V - cubic.

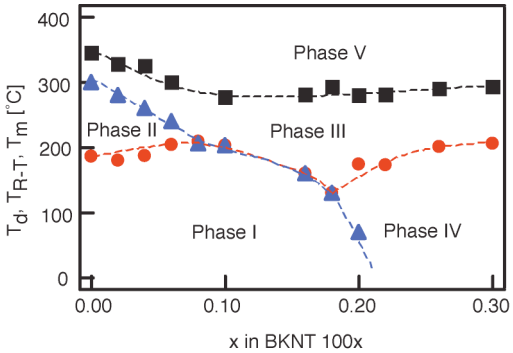

Figure 2-2 - Phase diagram of BNT-BKT (similar type as BNT-BT)[29].
Phase I - ferroelectric Rhombohedral, phase II - anti parallel domain configuration rhombohedral, phase III - pseudocubic ferroelectric relaxor, phase IV - ferroelectric tetragonal and phase V - cubic

Poled samples near the presumed MPB were measured[28, 30] to give P_r=20μC/cm^2, k_{33}=55%, k_{31}=19% and d_{33}=110-125pC/N when conventionally prepared, and P_r=37μC/cm^2, k_{33}=28%, Ec=43kV/cm and d_{33}=180pC/N when powders were prepared with the citrate method[27]. An enlargement in the lattice parameters[31], as well as a peak in properties, were seen around x=0.06 at room temperature[28, 32] (Figure 2-3), all of which indicate the proximity of a phase transition.

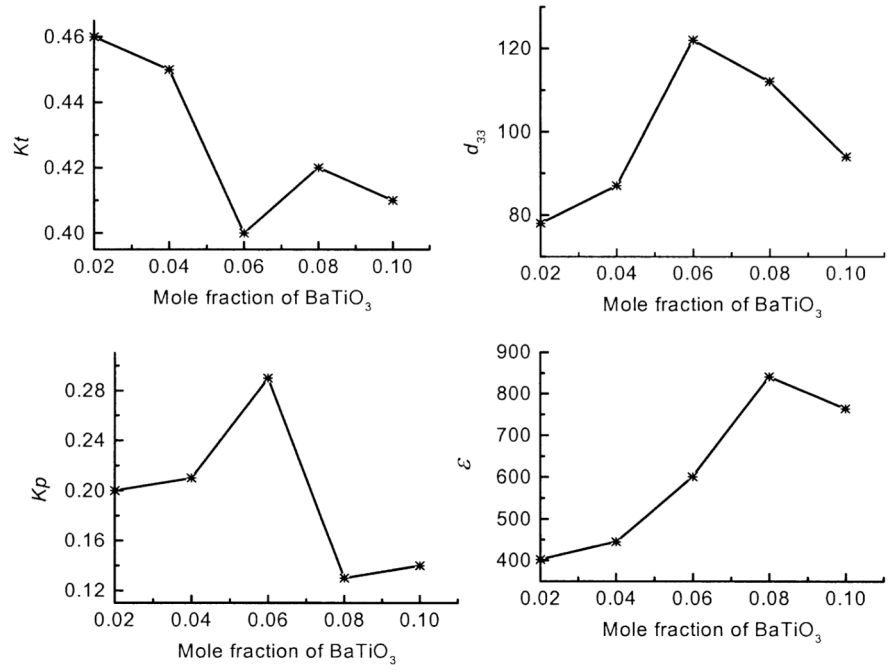

Figure 2-3 - Dielectric and piezoelectric properties of BNT-BT ceramics at room temperature[32]

Temperature dependent permittivity plots[33, 34] of BNT show a maximum at 320°C and a hump around 200°C. Double hysteresis loops[33] around 200°C and their complete disappearance[35] above 200°C, in addition to changes in the domain structure and darkening of single crystal[35] which disappears above 295°C, all suggest that two phase regions exist in the temperature range of 200°C -320°C: above 300°C a tetragonal paraelectric phase, and below 300°C an antiferroelectric phase or a phase containing polar regions.

Kittel[36] postulated antiferroelectric to be a phase where subcells show a polar arrangement, but in which adjacent subcells were oppositely polarized, giving a net zero polarization and a center of symmetry. Switching of the polar subcells is possible

by application of field, however as the field is removed, polarity would switch back producing pinched (double) hysteresis loops.

Such loops were measured at high temperatures (Figure 2-4) and were used to support the antiferroelectric hypothesis[28, 30]. In their papers, Takenaka et al and Zhang et al claim that near the MPB of BNT-BT at 100°C two phases co-exist, ferroelectric and antiferroelectric phases, both of which contribute to the strain (Figure 2-5). By heating the sample beyond 100°C, the strain originating from ferroelectric domain switching gradually disappears, and so does the observed total strain.

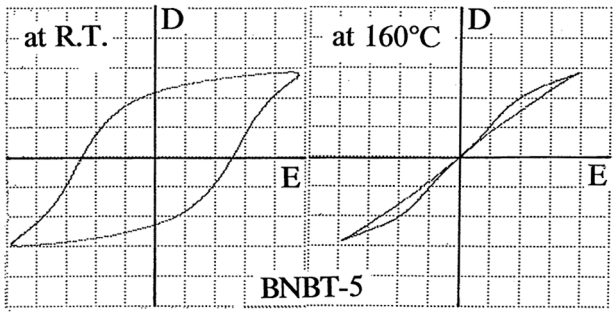

Figure 2-4 - D-E hysteresis loops[28] of BNT-5BT at room temperature and at 160°C, corresponding to ferroelectric and antiferroelectric phases, respectively

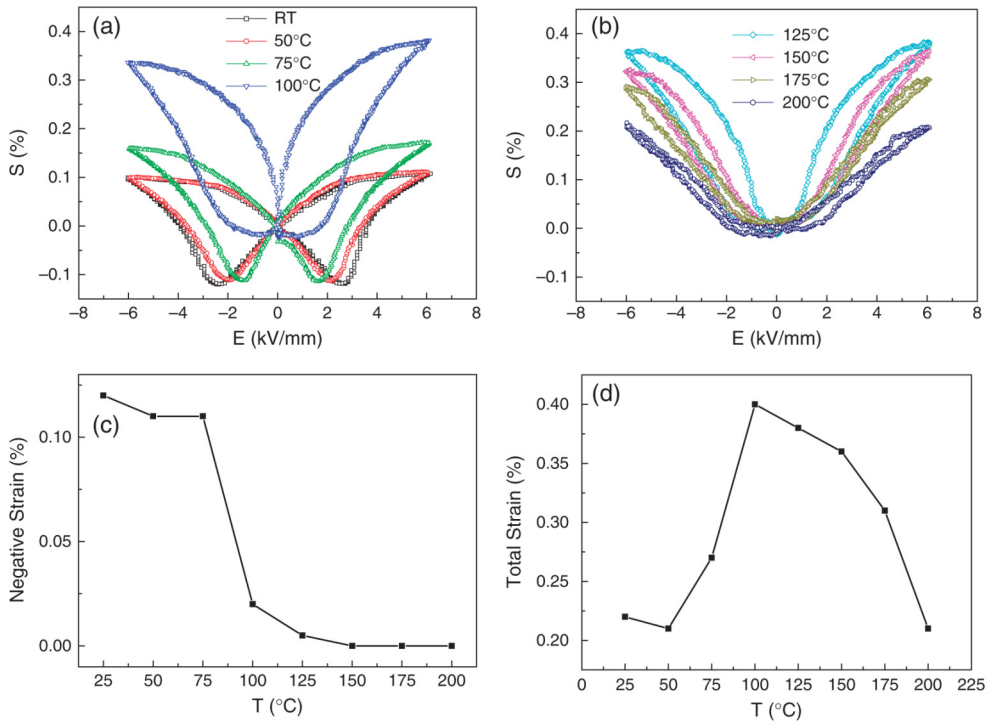

Figure 2-5 - Temperature dependent (a), (b) bipolar S(E) curves, (c) negative strain and (d) total strain of BNT-6BT ceramic[30]

But other data question the claim of antiferroelectricity: no super structure was detected by x-ray diffraction (XRD)[33, 34, 37] and neutron diffraction[37]; Raman spectra show that the phase separating paraelectric tetragonal and ferroelectric rhombohedral phases is remarkably similar to, and probably isomorphic with, the ferroelectric tetragonal phase of BaTiO3, showing no extra phonon features in the tetragonal phase, in comparison with the rhombohedral phase[38].

These data suggest that the paraelectric tetragonal phase and the ferroelectric rhombohedral phase actually coexist in this temperature range. This has been further supported by pyroelectric measurements, showing weak current pulses explained by the remaining polar micro-regions, and electrostrictive strain measurements displaying anomalies in the examined temperature range[39].

Roleder et al. reached the same conclusion from the study of time dependant electric permittivity[40]. The size and dynamics of the regions varied when temperature was changed, but the possibility of ordering the polar regions with an external electric field below 280°C confirmed that below this temperature the regions are stable. Moreover, the maximum in permittivity and electrostrictive strain at 320°C (cubic transition temperature) could exclusively be result of changes in dynamics and sizes of the polar regions[39].

2.1.2. Potassium Sodium Niobate – $(K,Na)NbO_3$

A solid solution of ferroelectric $KNbO_3$ with the antiferroelectric $NaNbO_3$, $(K,Na)NbO_3$ (KNN), creates a system with three MPBs, with ferroelectric phases up to about 90% $NaNbO_3$ (Figure 2-6). Over most of the phase diagram the phase transition sequence is similar to that in barium titanate[2]: paraelectric cubic phase - tetragonal - orthorhombic - rhombohedral, the last three being ferroelectric. Except for the orthorhombic-rhombohedral phase transition, other phase transitions vary little in temperature over the composition range[2, 41, 42].

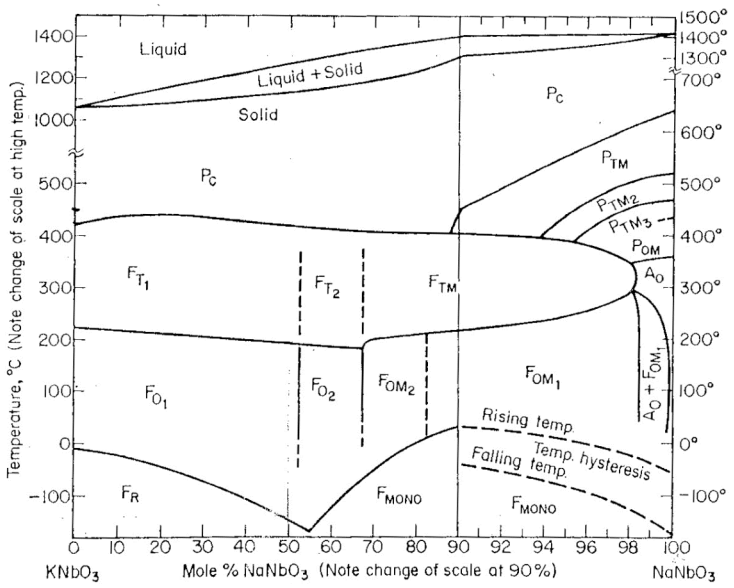

Figure 2-6 – Solid solution phase diagram[2] of $KNbO_3$-$NaNbO_3$

Near the 50-50 ratio of $KNbO_3$-$NaNbO_3$ an MPB separates two tetragonal phases at high temperatures and two orthorhombic phases at room temperature, with different tilting of the oxygen octahedra[43].

Recent studies[44-46] identified monoclinic phase in all compositions, co-existing at times with the rhombohedral phase. Attia et al[47] suggest that the low temperature rhombohedral phase forms unusual clusters within an orthorhombic matrix in ceramic samples, showing continuous transition in XRD. Raman spectroscopy study of single crystals[48] show similar spectra to those reported in $KNbO_3$ (KN), with only modest shifts in the frequencies of the prominent lines, and thus confirming that KNN and KN adopt the same series of crystal structures through all of their ferroelectric phases. Clear and abrupt transitions between the rhombohedral and orthorhombic phases do not support a mixed-phase region in single crystals.

Crossing the orthorhombic-orthorhombic phase boundary at room temperature, showed a peak in the piezoelectric properties (Figure 2-7). Hence, many studies focus on this region of concentrations.

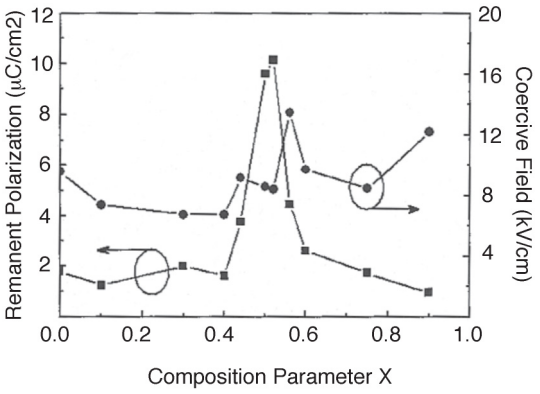

Figure 2-7 - Ferroelectric properties of KNN at room temperature accross the MPB[49]

Conventionally sintered KNN ceramics were reported[50-52] to have d_{33}=100pC/N, k_t=45%, k_p=39% and ε=200 [53]. Since KNN ceramics are difficult to process to full densities by conventional sintering[54], hot pressing techniques have been successfully employed[55, 56], giving a rather high piezoelectric longitudinal response[55] d_{33}=160pC/N, a value which is between those of modified lead titanate and hard PZT, k_p=48% and a relatively low dielectric constant (around 400 at room temperature)[57, 58]. These properties suggest that KNN ceramics could therefore be considered as a viable alternative to PZT materials for selected applications.

2.1.3. Potassium Sodium Lithium Niobate – (K,Na,Li)NbO_3

Excellent piezoelectric and electromechanical properties were reported in 2004 by two groups for Li doped $K_{0.5}Na_{0.5}NbO_3$ ((1-x)($K_{0.5}Na_{0.5}$)NbO_3-x$LiNbO_3$ KNLN). Both Saito et al[59] and Guo et al[60] observed a perovskite structure which is orthorhombic for x≤0.05 and becomes tetragonal at x≥0.07 (Figure 2-8a). They claimed that an MPB between orthorhombic and tetragonal phases is the reason for the enhanced properties measured near the phase boundary at room temperature: d_{33} reaches 200–235 pC/N, k_p in the range of 38%–44% and k_t of 44%–48% (Figure 2-8b).

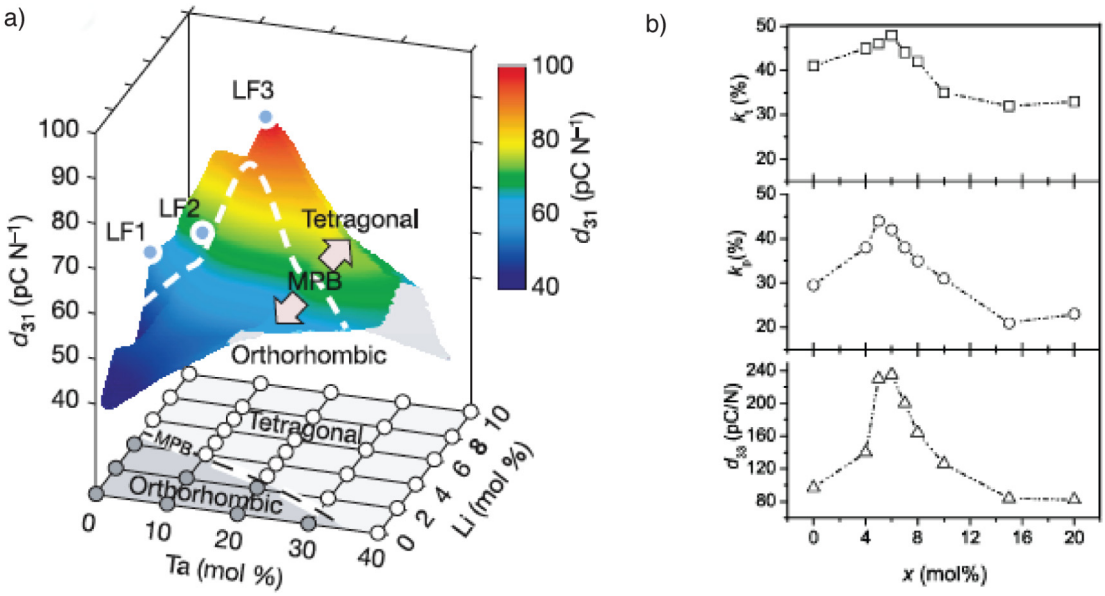

Figure 2-8 - (a) Phase diagram of KNN with Li and Ta doping[59] and (b) coupling and piezoelectric properties of KNN with Li doping[60]

In recent years, many publications claimed to have optimized the processing conditions to give the best properties: the sintering heat rate[61] and sintering temperature[62, 63]. But no two papers seem to agree on the processing conditions. Even papers by the same authors, published in the very same year do not necessarily coincide, as can be seen in the example of the papers published by Du et al[64, 65], where poling conditions were presumably optimized to be 3.5kV/mm, at 120°C for 30 minutes in one paper, and 4kV/mm, at 50°C for 30 minutes in another,

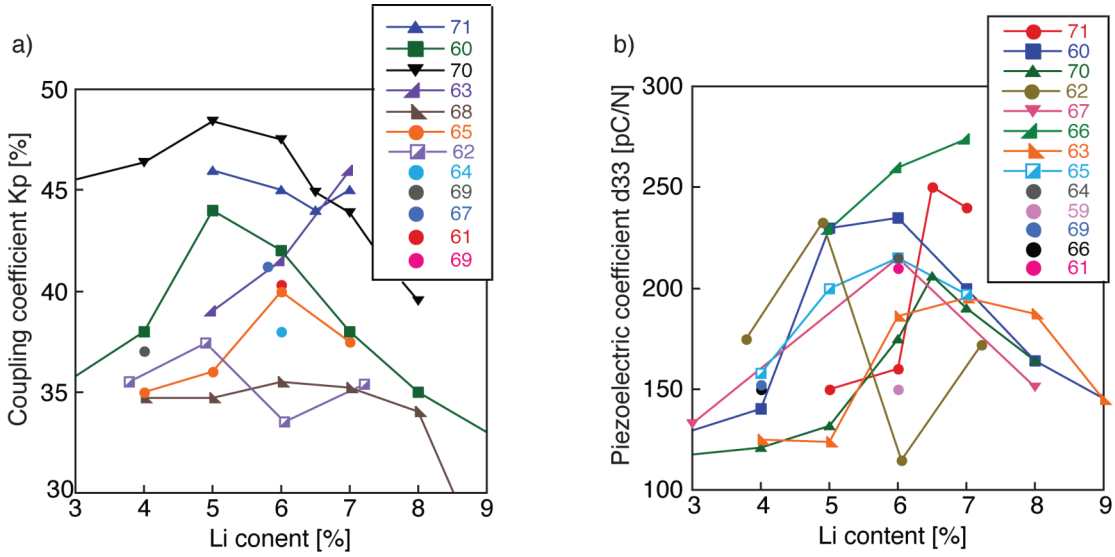

Figure 2-9 summarizes published coupling coefficients and piezoelectric properties. As can be seen in the figure, properties are not reproducible between

authors, indicating that the processing critically influences the properties. However, the acute step was not identified and non reproducibility is not addressed in the literature.

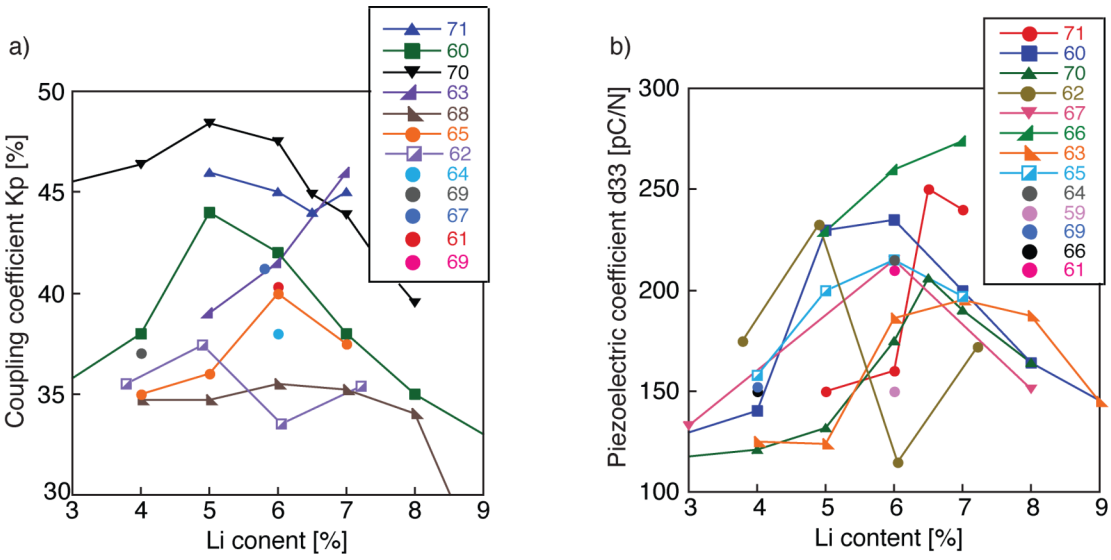

Figure 2-9 - Summary of published (a) coupling coefficients and (b) piezoelectric properties of KNLN ceramics[59-71]

2.2. Biological system

Various tissues and organs of the human body including bones[72-75], eyes[76] , pineal gland[77], and dentin[78] are known to exhibit piezoelectric properties.

2.2.1. The bone

The structure of the bone, in a simplified layout, comprises a network of collagen fibers that are impregnated with crystals of hydroxyapatite, $Ca_5(PO_4)_3(OH)$, and calcium carbonate[79] (Figure 2-10). Collagen is a flexible, tough protein that dictates the shape of the bone, to which the hydroxyapatite phase is bonded via polar functional groups on the protein molecules and provides additional strength.

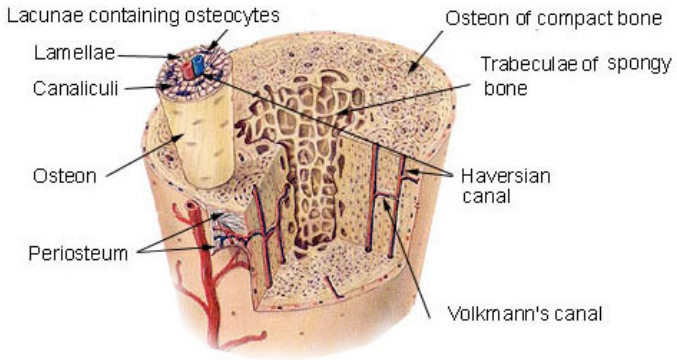

Figure 2-10 - Compact and spongy bone structure[80]

The structure and the function of bone are maintained by a balance between the activities of bone forming cells and the bone resorbing cells, which are produced by cell division from a population of undifferentiated "stem" cells[79]. Two major stimuli, hormonal and mechanical, seem to be responsible for the activation of these "stem" cells. It is not completely clear what mediates this activation, but some evidence show electrical phenomena may be involved.

Many studies show that bones exhibit piezoelectric properties[74, 75]. It was demonstrated[73] that the piezoelectric effect is generated in the collagen constituent of bone, and not in the hydroxyapatite phase (Figure 2-11). Measurements reveal that maximal potential differences occur when the shear plane is displaced about 10° from the true long axis[81]. This is in fact the amount by which the mean direction of the long collagen fibers deviates from this true axis, corresponding to the argument that the piezoelectric effect is due to the collagen component. However, another study[82] shows macroscopic piezoelectricity in hydroxyapatite ceramics, by measuring low shear piezoelectric coefficient (d_{14}=14pC/N).

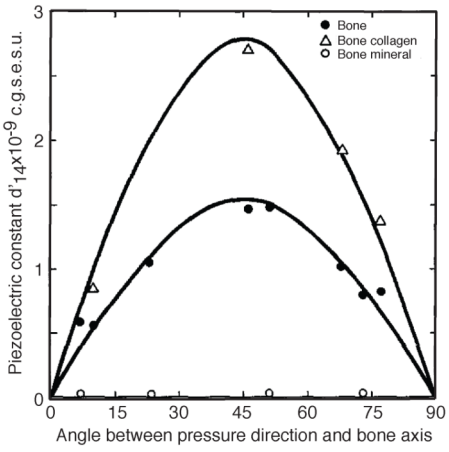

Figure 2-11 – Bone, hydroxyapatite and collagen piezoelectric coefficients[73]

It should be mentioned that other mechanisms other than piezoelectricity were postulated to explain the existence of potentials in the bone, one of which is the concept of streaming potentials. Biological tissues are comprised of many components that possess inherent surface charges, such as cell membranes. Thus at a tissue-liquid interface, ions within the liquid which are of opposite polarity to the tissue charge, could be attracted to that tissue. If the liquid is in motion, some of the more loosely bound ions will be carried along, which constitutes current flow, and which can result in a measurable potential difference[81].

2.2.2. Influence of current and charges on osteogenesis (recreation) of bones

The measured potentials in the bone led to the idea it could be possible to artificially stimulate bone growth using electrical phenomena.

Many experiments studying bone growth via electric currents were initiated following the report of Bassett et al[83] who concluded bone growth is stimulated in regions of relative electronegativity. An interesting work by Friedenberg et al[84] investigated whether electric currents were efficient in accelerating fracture healing. Strong evidence was obtained showing bone growth was stimulated very close to the cathodes when placed within the fracture gaps.

Different groups have then progressed to clinical treatments conducted on patients having nonunion fractures. From the review paper by Watson[81], it is clear that statistically the bones show good healing after the current treatment, but it is still not clear whether it is the threshold current density, voltage gradient, or the membrane that lines on the outer surface, which mediate bone growth stimulation.

Not only the effect of current on bone healing was studied but also the effects of electric and magnetic fields[81]. Electric field experiments have resulted in growth of new bone oriented towards the positive electrode, or in other words, where induced charge on the bone was negative. The magnetic field seems to result in an organization of the osteoblasts (bone forming cells) rather than their stimulated response.

In the past few years, experiments using poled hydroxyapatite enabled investigation of the influence of charges on the growth of bone. The hydroxyapatite

polarization mechanism was demonstrated by Nakamura et al[85] to be controlled by the transportation of the protons in the OH^- columnar structure (Figure 2-12). The polarization charge of 14.9μC/cm^2 for hydroxyapatite ceramics[85] was nearly twice as large[2] as that of ceramic $BaTiO_3$ (8μC/cm^2).

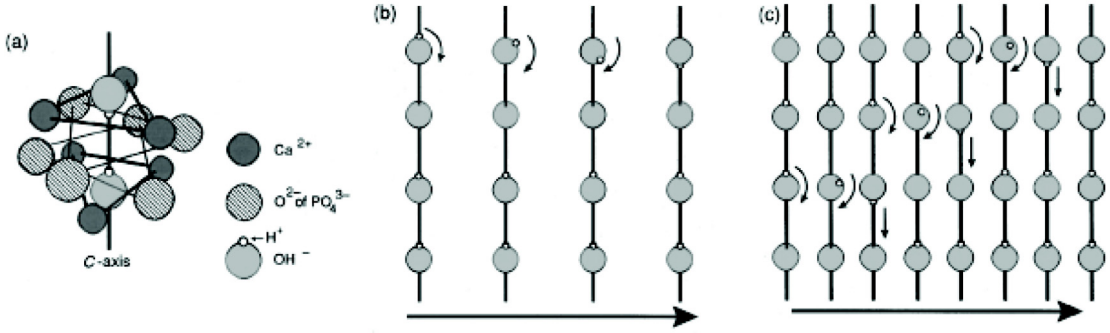

Figure 2-12 - Poling of hydroxyapatite[85]

Negative surface charges of electrically polarized hydroxyapatite ceramics have been proven to enhance the activity of bone forming cells, osteoblast[86, 87] and the adsorption of Ca^{+2} ions[88]. Itoh et al[89, 90] commented that the bone demineralizing cells are suppressed near the negatively charged surface and therefore may enhance bone formation. In contrast to the general agreement about the constructive influence of the negatively charged hydroxyapatite, the positively charged surface is controversial.

2.2.3. Hydroxyapatite

Since calcium phosphate is a natural bioactive component of the bone, constituting for 65% of the total bone mass, it is clearly a promising candidate for implant fabrication and fixation.

The most used calcium phosphate in implant fabrication is hydroxyapatite, $Ca_{10}(PO_4)_6(OH)_2$, since it is the most similar material to the mineral component of bone. It exhibits good properties as a biomaterial, such as biocompatibility, bioactivity, osteoconductivity and direct bonding to bone. Within the wide range of available calcium phosphates, it is important to control the Ca/P ratio. The lower the Ca/P ratio, the larger the acidity and solubility of the mixture. For Ca/P < 1, both acidity and solubility are extremely high, and both parameters decrease substantially

for Ca/P ratios close to 1.67, which is the value of stoichiometric hydroxyapatite, $Ca_{10}(PO_4)_6(OH)_2$. The lattice parameters of some of these phosphates are quite similar, leading to overlapping of reflection maxima, which makes difficult adequate interpretation of the powder XRD pattern[91].

Hydroxyapatite and β-tricalcium phosphate (β-TCP), $Ca_3(PO_4)_2$, often coexist in distinct proportions, depending on synthesis conditions. Moreover, when hydroxyapatite is heated over 1050°C it converts partially to β-TCP[92-95].

Currently, there is an increasing interest on preparation of two or more calcium phosphates mixtures. These materials are commonly prepared with hydroxyapatite and a more resorbable material such as tricalcium phosphate (α or β) or calcium carbonate in different properties depending on the characteristics required for a specific application.

2.2.4. BaTiO3-Hydroxyapatite system

On the basis of the piezoelectric effect of human bone, namely the piezoelectric collagen in hydroxyapatite mineral, a ceramic mixture of hydroxyapatite and ferroelectric $BaTiO_3$ has been studied.

The first paper on this system was presented by Feng et al[96], claiming the following properties of the composite: d_{33}=60pC/N, ε≈4700, k_{33}=0.21, C_{33}^D=1.1x10^8 N/m^2, density=5.6x10^{3}Kg/m^3. After testing the composite on mice, it was concluded that the composite possess the suitable piezoelectric properties and can accelerate the growth of bone cells, and the biological compatibility.

But much experimental data is missing in this report, such as the ratio of the two components and the processing method. In addition, raw powders like ZrO_2 and Li_2CO_3 are mentioned with no explanation to their use and concentration. No XRD data of the final composite is given and the biological experiments are poorly described.

A later paper[97] describes a set of experiments on 8 dogs, measuring the osteogenesis of bone on hydroxyapatite-$BaTiO_3$ composite implants, possessing d_{33}=6pC/N, k_{33}=0.12. Again, no information is given regarding the composition or the phases in this composite. Hydroxyapatite-$BaTiO_3$ composite has been claimed to

encourage the growth of new bone tissues when the polarization direction was vertical to the surface, rather then parallel to it. Collagen fibers were organized on the surface, vertically to the polarization direction.

A compositional study[98, 99] claimed that hydroxyapatite-$BaTiO_3$ composite would show piezoelectric effect only when the composite contains above 90vol% of $BaTiO_3$, suggesting the composition studied by Feng et al. consisted more then 90vol% of $BaTiO_3$. These studies do not contain any structural analysis.

A detailed structural research[100] tested the influence of sintering temperatures and atmospheres of various ratios hydroxyapatite-$BaTiO_3$ on the composition of the sintered composites. XRD peaks of BaTiO3 have disappeared when sintering above 900°C, which is an evidence for a reaction between hydroxyapatite and $BaTiO_3$. $BaTiO_3$ was completely consumed in the reaction after sintering at 1100°C. DT/TGA analysis supports these results. The reaction between hydroxyapatite and $BaTiO_3$ was observed in composites sintered under nitrogen, oxygen, helium, argon, carbon dioxide and dry air leading the formation of $CaTiO_3$, $Ca(PO_3)_2$ and Ba_2TiO_4 as byproducts. Only at composite containing 97.5wt% $BaTiO_3$, the d_{33} value was 20pC/N. Increasing hydroxyapatite concentration to 5wt%, no d_{33} value could be observed.

Chapter 3 - Definition of terms and experimental methods

This chapter presents terms (hysteresis loops and poling) and experimental methods (dielectric and piezoelectric measurements, Raman spectroscopy, X-ray diffraction, scanning electron microscopy, energy dispersive X-ray microanalysis, piezoelectric force microscopy and methods for composition analysis and biological cell visualization) all of which are used throughout this thesis.

3.1. Hysteresis loops

Under applied fields the dipole moment in each unit cell of ferroelectric materials can be reversed in direction by 180° or other discrete smaller angles that correspond to various axes of the cell. The dipoles can remain aligned in any of these allowed orientations. By definition, it is this reversibility of dipoles by an electric field that constitutes ferroelectricity. Regions of at least few unit cells with dipole moments oriented in the same direction are called domains, and the region separating two domains is called domain wall. During the field application and switching of domains, the movement of domain walls could be observed.

The easiest and most frequently used approach to measure changes in the polarization is by investigating charge-field hysteresis, generated by the simple Sawyer-Tower method. Charge density (D_i) of linear dielectrics is correlated to the polarization with the following relation:

$$D_i = \varepsilon_0 E_i + P_i \tag{3.1}$$

ε_0 being the permittivity of free space, and E the field. Since for most ferroelectrics the polarization is much larger then the first term ($\varepsilon_0 E$), polarization could be expressed using charge density (D).

Figure 3-1 presents a typical hysteresis loop. As field is applied (1) dipoles start switching, until (2) maximum of the polarization is reached for given conditions. When the field is reduced (E=0) a remnant polarization is observed (Pr). Application of field to the opposite direction (E<0) would cause switching of the domains to the reversed direction until saturation is reached (3). Changing the field direction once again, the dipoles would switch and eventually saturation would be reached (2). The filed at which majority of the dipoles start switching, P=0, is defined as the coercive field (Ec).

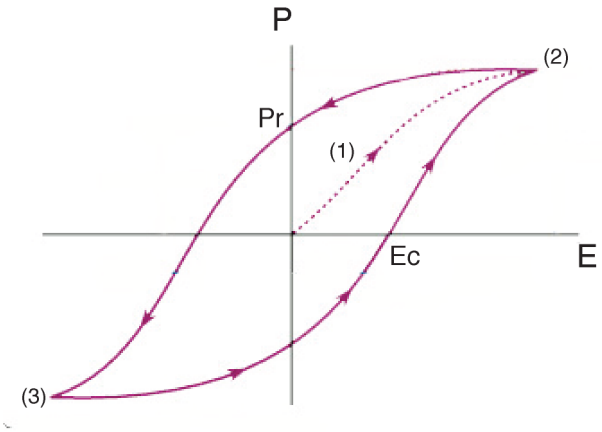

Figure 3-1 - D-E hysteresis loop

In this thesis, half hysteresis loops (application of positive field only) were used to compare the switching behavior of different ceramic samples and establish reproducibility of samples within the same composition. In addition, half and full hysteresis loops were compared at various temperatures showing "opening" of loops or "pinching" of loops, both indicating changes in the crystal phases (for more discussion, see Chapter 4).

3.2. Poling

Single crystals tend to develop domains in order to reduce stresses and depolarization field. Due to these domains, often the overall polarization of the crystal is zero and no piezoelectric response can be measured. Therefore it is desirable to orient the domains to one general direction. This can be done by applying a sufficiently large field (above the coercive field Ec) that would bring about switching of the polarization vector of each domain to the nearest permitted direction according to the symmetry (Figure 3-2). In polycrystalline materials, where the crystallographic orientation of the grains is random with respect to one another, optimized poling conditions are of great importance.

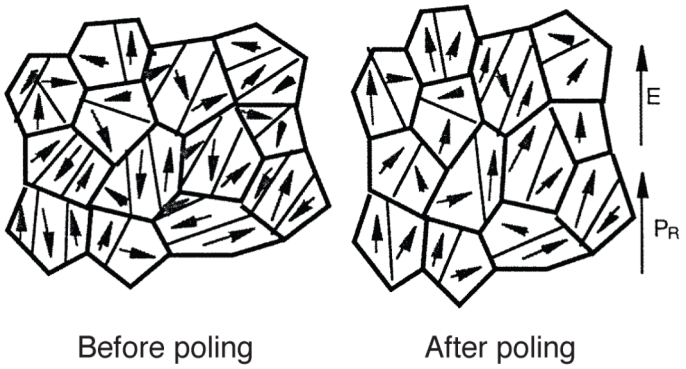

Figure 3-2 - Polycrystalline ferroelectric with random orientated grains before and after poling[101]

Since orientation of domains include dimensional modifications, clamped sample would be harder to pole. As the temperature is increased, atoms vibrate stronger and the structure becomes softer mechanically and electrically and therefore, poling is easier. However, the same thermal vibrations increase conductivity in the sample that may lead to breakdown when high field is applied.

Consequently, it is necessary to optimize poling temperature, time and the electric field for each material. In most cases the field should be at least as large as the coercive field in order to maximize the remnant polarization.

Poling conditions in this thesis, summarized in Table 3-1, were either specially optimized (detailed description in the relevant chapter) or taken from the literature. Poling was made in silicon oil.

Material	Chapter	Field [kV/cm]	Temperature [°C]	Time [Minutes]
BNT-BT	4	40	60	20
KNLN	5,6	50	50	5-30
PZT	9	30	100	30

Table 3-1 - Poling conditions for the materials used in this thesis

3.3. Dielectric measurement

Relative permittivity ε was determined from the sample capacitance, C, measured using an HP 4284A LCR bridge.

$$C = \varepsilon_0 \varepsilon A / t \qquad (3.2)$$

A being electrode surface, t the thickness of the sample (with A>t), and ε_0 being the permittivity of free space (8.8514×10^{-12}F/m). Loss tangent values were collected during the same measurements.

In this thesis, the samples used for the measurements were in form of thin disks of 0.2-0.7mm in thickness and about 5-7mm in diameter. Using liquid nitrogen and a home-made furnace dielectric measurements were conducted in temperatures ranging from -150°C and up to 550°C. The sample's temperature was recorded using a thermocouple placed as closely as possible to the sample. Measurements were conducted at five frequencies between 100Hz and 1MHz.

In addition, real and imaginary permittivities were calculated from measured impedance (using an HP 4396A impedance analyzer) or resonance frequency and quality factor (using an HP 8722D vector network analyzer) as described in the literature[102]. Measurements were conducted on cylinder shaped samples, with typical dimensions of about 1mm in diameter and 5mm in length, at room temperature from 1KHz to 1.8GHz and from 3.3 and up to 7.8GHz respectively.

3.4. Piezoelectric measurements

3.4.1. Resonance measurements – coupling coefficients

Piezoelectric materials convert electric energy into mechanical energy and vice versa. The electromechanical coupling factor (k) expresses the fraction of the electrical energy converted to mechanical energy (and the other way around), when an electric field is applied.

The electromechanical coupling factors are dimensionless measures proportional to the strength of the piezoelectric effects. They depend on the poling degree, and are extremely useful as a figure of merit[1, 2].

When an alternating electric field is applied on a piezoelectric element, elastic waves are created. The element can be excited to produce mechanical resonances at frequencies that are related to the geometry (l, the dimension of the sample which controls the resonance), density (ρ) and elastic constants (s). At the resonance the element vibrates, the impedance of the element is minimal and the fundamental resonant frequency, f_r, is given by:

$$f_r \propto 1/\left(2l\sqrt{\rho s}\right) \tag{3.3}$$

At the antiresonant frequency the admittance becomes very small (close to zero), and the impedance becomes large (infinite if no losses present).

Elements of different geometry are used to obtain different resonance modes. The samples measured in this thesis were disk shaped with radius to thickness ratio bigger then 10. The series resonance frequency f_s and the parallel resonance frequency f_p were extracted from the maximum of the conductance G and resistance R, respectively ($Y = G + iB; Z = R + iX$).

The thickness coupling coefficient, k_t, is associated with longitudinal vibrations of thin plates.

$$k_t^2 = \frac{\pi}{2}\frac{f_s}{f_p}\cot\left(\frac{\pi}{2}\frac{f_s}{f_p}\right) \tag{3.4}$$

The planar coefficient, k_p, is associated with the transverse mode of thin disks.

$$\frac{k_p^2}{1-k_p^2} = \frac{\left(1-\sigma^E\right)J_1\left[\eta_1(1+\Delta f/f_s)\right] - \eta_1(1+\Delta f/f_s)J_0\left[\eta_1(1+\Delta f/f_s)\right]}{\left(1+\sigma^E\right)J_1\left[\eta_1(1+\Delta f/f_s)\right]} \tag{3.5}$$

where J_0=Bessel function of first kind and zero order; J_1=Bessel function of first kind and first order; η_1=lowest positive root of $\left(1+\sigma^E\right)J_1(\eta) = \eta J_0(\eta)$; σ^E being Poisson's ratio; $\Delta f = \left(f_p - f_s\right)$. These functions were computer calculated using Mathematica program.

In this thesis, resonant and antiresonant frequencies were measured using an HP 4194A impedance analyzer. In order to minimize external forces and clamping of the samples enforced by a sample holder, gold wires were used as connectors, keeping the sample hanging nearly free. Measurements were conducted in a Delta Chamber 9023 furnace, connected to liquid nitrogen for cooling, enabling the measurements to range from -150°C up to 250°C. Temperatures were recorded using a thermocouple placed as closely as possible to the sample.

3.4.2. Direct measurement -Piezoelectric coefficient

The longitudinal piezoelectric coefficient (d_{33}) can easily be extracted from the direct piezoelectric effect - the generation of charge (D_3) upon application of an applied stress (σ_3).

$$D_3 = d_{33}\sigma_3 \tag{3.6}$$

Using Berlincourt-type press method, charge Q_s is created on the electrode area (A) as a consequence of applied stress.

$$D_3 = Q_s / A \tag{3.7}$$

The charge is measured via a parallel sensing capacitor (C_S) placed in series to a reference piezoelectric element and capacitor (C_R) (Figure 3-3).

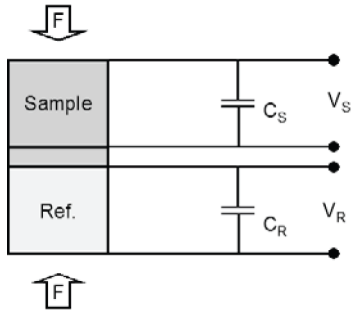

Figure 3-3 - Schematic of a Berlincourt-type meter setup used for the piezoelectric coefficient

The charges correspond to voltages V_S and V_R, and C_S/C_R can be set to unity. Since both elements feel the same force, the longitudinal piezoelectric coefficient can be extracted.

$$d_{33S} = d_{33R} \times \left(\frac{C_S}{C_R}\right) \times \left(\frac{V_S}{V_R}\right) \tag{3.8}$$

Clamping effect caused by the friction between the sample and the pressing plates, may lead to unwanted lateral stresses, and therefore reduce the measured coefficient[103, 104]. In order to minimize this effect, the top-pressing surface was designed to be round, producing a point contact with the sample.

In this thesis, a waveform generator produced an alternating voltage signal of about 200 Hz, which was then amplified by a power amplifier to drive the actuator. The voltages generated on both capacitors were measured by an oscilloscope.

3.5. Raman spectroscopy

Raman scattering is the inelastic process during which light quantum $h\nu_0$ hitting a crystal is exchanged to vibrational energy[105]. Only if the polarizability of the molecule changes during a vibration, will the vibration be Raman active[106].

The absolute intensity and the frequency of an emitted line provide information of the molecular structure. Hence, Raman spectroscopy was used in this thesis to detect phase transitions as a function of temperature and composition.

Raman spectroscopy was conducted using a Renishaw In Via Raman microscope. The samples were enclosed in a Linkam THMSG 600 variable temperature stage for data above -190°C, and a liquid He flow Oxford microcryostat for lower temperatures, down to -266°C. The 488nm line of an Ar laser was used as excitation source for the measurements. The illuminated spot at the sample was of about 0.5-0.7μm diameter. Laser power was kept to less than 1mW, which limited laser heating of the samples to less then the temperature resolution used.

3.6. X-Ray diffraction (XRD)

X-ray diffraction is one of the most trusted and used techniques for resolving crystal structures due to its sensitivity to small changes in the unit cell.

In this thesis powder XRD was used to determine the crystal structure of powders and sintered samples at different temperatures. Sintered pellets were crushed using pestle and mortar to powder with particle size smaller then 0.5mm. Crushing was used in order to avoid orientation effects on the diffraction. All powders were pressed in a glass holder and the surface was flattened to minimize scattering due to topography.

The plane spacing (d) can be calculated for each reflection using the Bragg law:

$$\lambda = 2d\sin\theta \tag{3.9}$$

where λ is the wavelength and θ is the reflection angle.

Matching of the plane spacing to Miller indices (h,k,l) depends on the structural phase (lattice parameters a,b,c and the angle β), according to the following equations[107]:

Cubic
$$\frac{1}{d^2} = \frac{h^2 + k^2 + l^2}{a^2} \tag{3.10}$$

Tetragonal
$$\frac{1}{d^2} = \frac{h^2 + k^2}{a^2} + \frac{l^2}{c^2}$$

Rhombohedral
$$\frac{1}{d^2} = \frac{\left(h^2 + k^2 + l^2\right)\sin^2\beta + 2\left(hk + kl + hl\right)\left(\cos^2\beta - \cos\beta\right)}{a^2\left(1 - 3\cos^2\beta + 2\cos^3\beta\right)}$$

Orthorhombic
$$\frac{1}{d^2} = \frac{h^2}{a^2} + \frac{k^2}{b^2} + \frac{l^2}{c^2}$$

Monoclinic
$$\frac{1}{d^2} = \frac{1}{\sin^2\beta}\left(\frac{h^2}{a^2} + \frac{k^2\sin^2\beta}{b^2} + \frac{l^2}{c^2} - \frac{2hl\cos\beta}{ac}\right)$$

Note that orthorhombic phase can be described as monoclinic with $\beta = 90^{\circ}$. This is useful when different phases are considered possible. Since the monoclinic representation is more general, it can be used as the basis for comparison.

Room temperature XRD diffractions were collected with a Siemens Kristalloflex diffractometer using Kα wavelength from a copper target. Small fringes of 0.3°/0.3°/0.3°/0.05° and long acquisition times (4-6 seconds) were used for good signal to noise ratio. Temperature dependent diffractions were carried out with goniometer Crystal equipped with nitrogen cryostat and furnace, from (-170)°C to 500°C.

3.7. Scanning electron microscopy (SEM) and Energy dispersive X-Ray microanalysis (EDX)

In this thesis a Philips XLF30 SEM and an SFEG Sirion SEM were used for surface study of sintered samples, fracture surface investigation and powder observations. In addition, both microscopes were used for chemical analysis, exploiting their energy dispersive X-ray (EDX) detectors. The data was recorded and treated with the microanalysis system INCA. In cases charging effects were observed (non conductive samples), thin carbon layer was deposited on the sample surface.

Biological samples were specially treated before examination to manage the high vacuum needed. Images of cultured cells presented in this thesis were acquired after pre-fixation with Glutaraldehyde 0.1M in Cacodylate buffer, pH 7, following dehydration with gradient of Ethanol and application of Hexamethyldisilazane (HMDS, company) solution. Thin coated layer of gold was used as conductive layer. Quanta 200 FEI SEM was operated at high vacuum, with 100μA emission current and voltage of 10kV.

3.8. Piezoelectric force microscopy - PFM

Piezoelectric Force Microscopy (PFM) uses the converse piezoelectric effect to image domain patterns and identify polarization orientations on a very small scale on the sample surface. An electric field applied to the sample by a conductively coated atomic force microscope (AFM) tip, cause domain walls to move (domains with polarization parallel to the field extend and domains with opposite polarization contract). These small displacements are detected by the AFM probe. Analysis of the amplitudes and phases of the cantilever vibrations enables reconstruction of the domain structure in the sample.

In this thesis, PFM was used to ratify the existence of regions of ferroelectricity in a ferroelectric-non ferroelectric composite (KNLN-Hydroxyapatite composite). The setup used is illustrated in Figure 3-4.

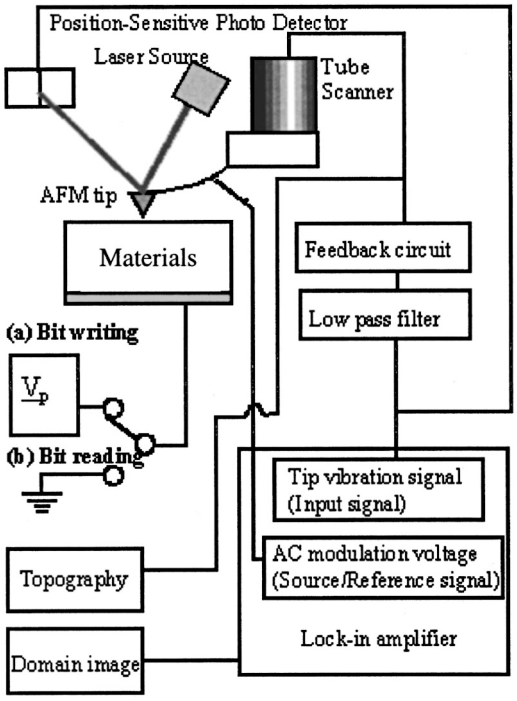

Figure 3-4 - Schematic of the PFM setup used for ferroelectricity verification[108]

3.9. Laser Ablation Inductive Coupled Plasma Mass Spectroscopy

Laser Ablation inductively coupled plasma mass spectroscopy (LA-ICP-MS) is a sensitive analytical method for rapid multi-element determination of matter such as geological, ceramic and radioactive solid materials[109, 110]. The sample is vaporized in laser plasma by focused laser radiation and transported with argon into the inductively coupled plasma ion source. The ions are separated and counted according to mass and charge in a mass spectrometer. Since laser probing uses light rather than charged particles, analysis of both conducting and non-conducting material is possible, without the need for a conductive coat or other charge balancing techniques, as in electron microprobe techniques.

The high sensitivity of the ICP-MS (detection limit in the range of parts per billion), and the small samples required, are ideal for compositional gradients investigations across a sample[111]. In addition, the possibility of detecting up to 70 elements turns LA-ICP-MS to a useful tool for characterization.

In this thesis, EXCIMER laser (193nm) coupled to a Perkin-Elmer ELAN 6100 DRC ICP-MS was used for compositional verifications of ceramic containing Li, and for homogeneity verification across these samples.

3.10. Biological cell visualization

Due to their structure and composition, observation of biological cells requires special preparation. Coloring of the cells can be adapted accordingly, so that specific characteristics of the cell could be studied. In this thesis, the following coloring methods were used to study the attachment and viability of cells to KNLN and PZT ceramic surfaces.

3.10.1. Hematoxyline and Eosin (H&E) staining

Hematoxyline and Eosin staining method involves application of the basic dye Hematoxyline, which stains the nucleus of cells with blue-purple color, and acidic Eosin, which stains the cytoplasm of cells with pink color. This staining enables simple visualization of live cells under optical microscope.

3.10.2. Alamar-blue viability assay

Alamar Blue Assay incorporates an oxidation-reduction (REDOX) growth indicator. As cells grow, innate metabolic activity results in a chemical reduction of Alamar Blue, and therefore directly connected to the viability of cells. Reduction causes the REDOX indicator to change from oxidized form (non fluorescent, blue) to reduced form (fluorescent, red), which was detected quantitatively using spectrophotometer.

3.10.3. Fluorescence cell viability assay

The live staining assay is a color fluorescence assay that determines live cells using Calcein AM (Sigma). Live cells have intracellular esterases that convert nonfluorescent, cell-permeable Calcein acetoxymethyl (Calcein AM) to the intensely fluorescent calcein. Calcein is well retained within viable cells producing intense uniform green fluorescence in live cells (ex/em ~495 nm/~515 nm) visualized by a fluorescence microscope.

Chapter 4 - BNT-BT

Phase diagram refinement and evaluation of domain wall contribution to properties

A composition - temperature phase diagram of the system $(1-x)(Bi_{0.5}Na_{0.5})TiO_3$-$xBaTiO_3$ (xBNBT) is presented for $0 \leq x \leq 0.09$. Assignment of the complex phases was addressed by investigating X-ray diffraction, hysteresis loops, dielectric and piezoelectric properties, and Raman spectroscopy of ceramic samples containing 0-9%BNBT in a temperature range of -200°C to 550°C.

Analysis of the data agrees in main lines with the phase diagram published by Hiruma et al (based on an earlier phase diagram by Takenaka et al), showing a transition at high temperatures from a paraelectric phase, believed to be tetragonal, and a second transition at lower temperatures to a ferroelectric phase. Both phase diagrams show a morphotropic phase boundary in the ferroelectric phase separating rhombohedral phase at low %$BaTiO_3$, and tetragonal phase at high %$BaTiO_3$. However, whereas only one data point near room temperature was used in the former phase diagram, indicating this transition is between 6-7%BNBT, the phase diagram presented in this chapter shows clearly that this transition appears between 5-6%BNBT, and is perpendicular on the phase diagram in the temperature range from 50°C and down to -200°C.

Another important difference between the phase diagrams focuses on the temperature range from 200°C to 300°C. Hiruma et al identified the phase sequence at low %$BaTiO_3$ from ferroelectric rhombohedral to rhombohedral with anti parallel domain configuration to pseudocubic ferroelectric relaxor, and at high %$BaTiO_3$ to be tetragonal ferroelectric to pseudocubic ferroelectric relaxor. It is postulated in this chapter that the correct phase sequence should be ferroelectric rhombohedral (or tetragonal, at high %$BaTiO_3$) to a tetragonal mixed (possibly antiferroelectric or paraelectric) with ferroelectric rhombohedral polar regions (or tetragonal, at high %$BaTiO_3$) to the tetragonal matrix at low %$BaTiO_3$.

In addition, the extrinsic contribution to room temperature permittivity was studied using high frequency dielectric measurements.

4.1. Introduction

It is believed that lead containing materials exhibit good ferroelectric and piezoelectric properties due to the unique atomic structure of lead (large radius, high effective number of electrons and a lone electron pair in the outer shell). From the atomic point of view, bismuth possesses similar structure, thus bismuth containing compounds seem to be the most likely successors to lead based piezoelectrics[23]. In addition, since bismuth is a non-toxic heavy metal[24-26], bismuth containing compounds fill the environmental considerations.

The first phase diagram of $(1-x)(Bi_{0.5}Na_{0.5})TiO_3$-$xBaTiO_3$ (xBNBT) system was constructed by Takenaka et al[28] (Figure 2-1). Based on this diagram, a slightly modified phase diagram was later published by Hiruma et al[29] (Figure 2-2), exhibiting a controversial sequence of phase transitions. A paraelectric cubic phase above 530°C and a ferroelectric rhombohedral phase below 200°C are the only phases previous reports tend to agree upon, whereas the nature of the transient phase, especially in the temperature range 200-320°C, is still in dispute (see chapter 2.1.1).

In this thesis, a composition-temperature phase diagram of xBNBT is presented for $0\% \leq x \leq 9\%$. Using polarization-field hysteresis loops, temperature and frequency dependent dielectric measurements, piezoelectric resonance measurements and Raman spectroscopy, 0-9%BNBT ceramic samples were studied over a temperature range of -200°C to 550°C, in order to shed some light on the complex sequence of phase transitions.

For convenience reasons, abbreviations will be used as given in Table 4-1.

Abbreviation	Definition
FE	Ferroelectric
AFE	Antiferroelectric
P	Paraelectric
C	Cubic
R	Rhombohedral
T	Tetragonal

Table 4-1 - Definition of abbreviations used in this chapter

4.2. Ceramic preparation

Ceramic samples of xBNBT with x=0, 2.5, 5, 6, 7 and 9% were prepared by solid state synthesis. High purity raw powders, Bi_2O_3 99.975%, Na_2CO_3 99.5%, $BaCO_3$ 99.8% and TiO_2 99.9%, were weighed according to the desired composition and mixed via ball milling (180rpm) with the aid of ZrO_2 balls for 24 hours in ethanol.

After drying the ethanol at 100°C, the powders were crushed using a pestle and mortar and transferred to a covered alumina crucible. The powders were then calcined at 900°C for 3 hours with a heating rate of 5°/min, after which they were ball milled again (250rpm) for 24 hours in ethanol and finally dried.

The final powders were pressed to 9mm diameter pellets and then sealed in a plastic wrapping. The air was vacuumed and the samples were pressed with cold isostatic pressure (CIP) under 700KN for 1.5 minutes and a release time of 1.5 minutes. The samples were then taken out from the wrapping and stacked in an alumina crucible with powder of the same composition surrounding and separating them. They were sintered in air at 1150°C with a heating and cooling rate of 5°C /min and dwell time of 3 hours.

Densities of pellets were calculated according to their measured dimensions and weight. Table 4-2 summarizes the averaged densities of 5 samples from each composition, showing small deviations between samples as well as between compositions.

Composition	0%BNBT	2.5%BNBT	5%BNBT	6%BNBT	7%BNBT	9%BNBT
Theoretical density[31] [gr/cm3]	5.99	5.96	5.96	5.96	5.97	5.98
Averaged density [gr/cm3]	5.67	5.68	5.54	5.51	5.44	5.39
Averaged density [%]	94.6	95.2	92.9	92.5	91.2	90.3
STDEV [%]	0.2	0.7	1.0	0.7	0.5	0.5

Table 4-2 - Calculated densities of x%BNBT samples

Fracture surfaces of samples of all compositions were investigated using SEM. Fairly homogenous grains were observed and their average size was estimated to be between $10\,\mu m$ for 0%BNBT and $5\,\mu m$ for 9%BNBT, as can be seen in Figure 4-1a and b, respectively.

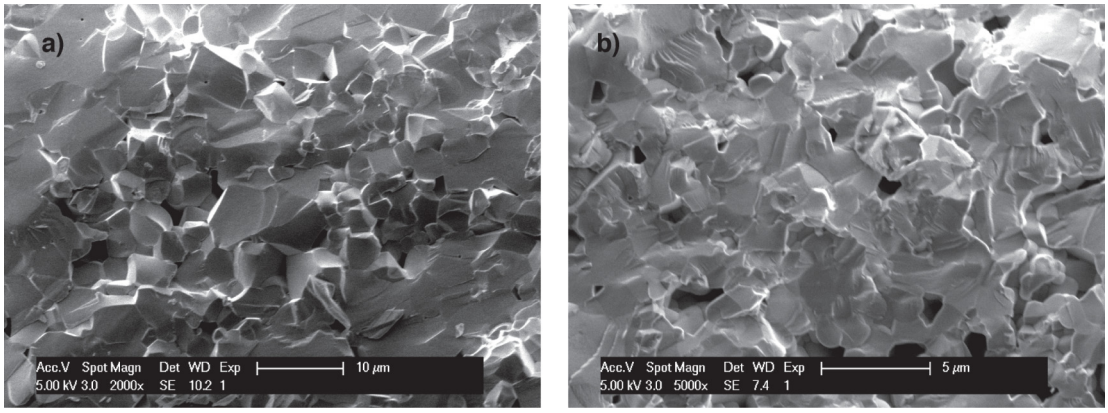

Figure 4-1 - SEM images of (a) 0%BNBT and (b) 9%BNBT fracture surface

The samples were polished to 1000 grade (~$15\,\mu m$), cleaned with acetone, coated in Ar plasma with Ag-Au electrodes, and poled according to published optimized conditions[112], at 60°C under 40kV/cm for 20 minutes. Table 4-3 presents the coupling coefficients, k_t and k_p, and the piezoelectric coefficient d_{33} measured at room temperature, showing good agreement with the literature[27, 112]. It should be noted that all three coefficients exhibit high values between 5 and 7%BNBT.

Composition	k_t [%]	k_p [%]	d_{33} [pC/N]
0%BNBT	12±2	36±5	62±2
2.5%BNBT	22±2	50±4	95±2
5%BNBT	31±0.5	51±3	101±7
6%BNBT	33±0.5	49±5	113±6
7%BNBT	17±0.5	49±3	143±15
9%BNBT	13±0.5	46±3	125±6

Table 4-3 - Piezoelectric coefficients of BNBT samples

4.3. X-Ray diffraction

X-Ray diffraction (XRD) spectra of BNT-xBT crushed samples were taken at room temperature at scanning angles 2θ=10-90° (Figure 4-2a) showing characteristic spectra of perovskite structure. In order to investigate the phases, higher resolution XRD were taken on xBNBT samples with x=0 and 9% in the interval 45-48° (Figure 4-2b). Small splitting can be observed due to the $k\alpha_1$ and $k\alpha_2$ copper wavelength.

Single peak in the interval 2θ=45-48° indicates an R phase (202), whereas in T phase this peak splits to (002) and (200) peaks[39]. However, the double peaks are not always easily seen close to the phase boundary[112]. A small double peak is seen in Figure 4-2b.

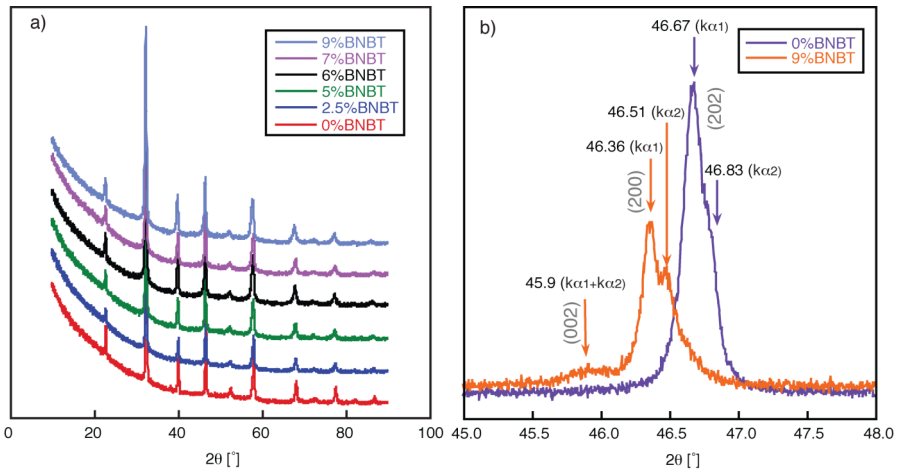

Figure 4-2 - XRD spectra taken at room temperature of (a) all compositions at 2θ=10-90° and (b) 0% and 9%BT at 2θ=45-48°

Calculation of the lattice parameters of 9%BNBT (see chapter 3.6) reveals close to C parameters with a=2.129Å and c=2.145Å, giving c/a ratio of 1.007 (as appose to ~1.02 seen for higher BT compositions[112]).

In their paper, McNeal et al[113] show that the structure of $BaTiO_3$ ceramics with fine grain size (~0.3 μm) tends towards cubic as the degree of splitting of the {200} reflections is greatly reduced. The decrease in tetragonality is attributed to the effects of internal stress on the crystal structure. In coarser grain ceramics (~15 μm), the larger grain size allows for the development of domain structure, compensating for homogenous stress. As has been shown in section 4.2, the grain size of 9%BT is smaller then 5 μm, hence might be the cause of the reduced tetragonality.

4.4. Hysteresis loops

Polarization-Field hysteresis loops of all compositions were measured under an electric field of 40kV/cm at different temperatures ranging from 22°C to 175°C (Figure 4-3).

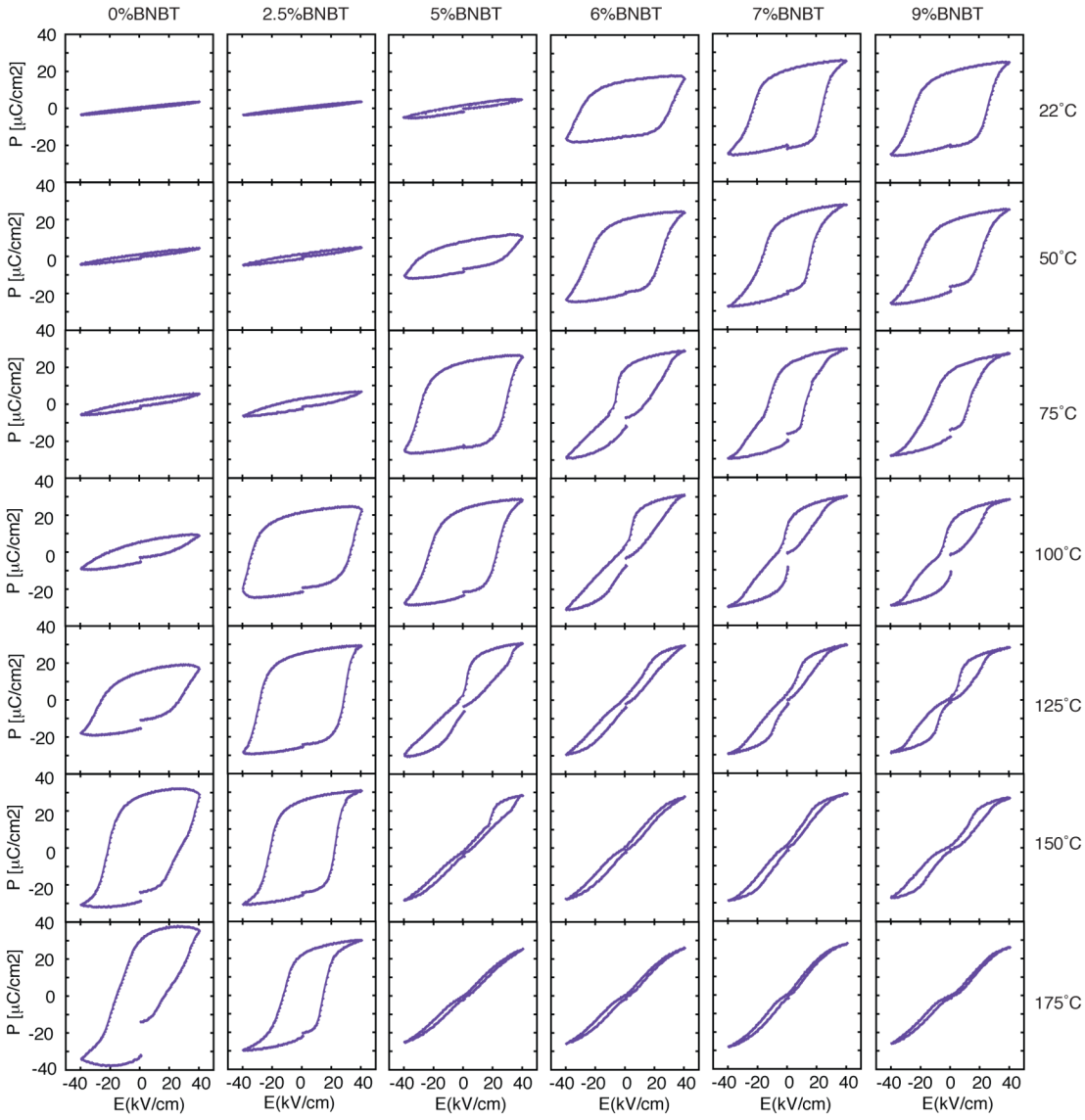

Figure 4-3 - P-E hysteresis loops of BNBT samples measured under 40kV/cm at different temperatures

A clear difference can be seen at room temperature between compositions with lower then 5%BNBT, exhibiting slant and not well developed hysteresis loops, and higher then 6%BNBT, where the loops are well saturated. As the field increased,

Figure 4-4, well-saturated loops were obtained for the low concentrations, exhibiting typical ferroelectric hysteresis loops with high coercive fields. As temperature increased (Figure 4-3), coercive fields decreased and the saturated loops were observed with lower fields (at 125°C for 0%BNBT, 100°C for 2.5%BNBT and 75°C for 5%BNBT).

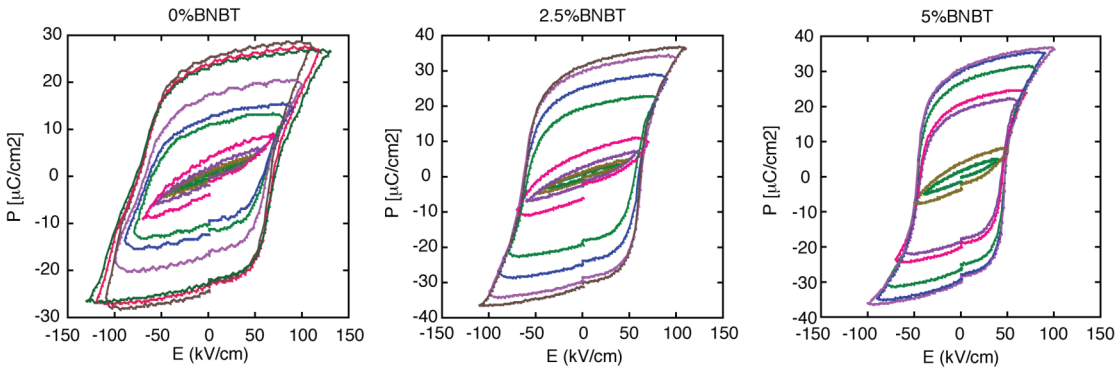

Figure 4-4 - Room temperature P-E hysteresis loops of 0%, 2.5% and 5%BNBT at varius fields

Fully developed loops become slightly slimmer as temperature increased (for example, 75°C for 7 and 9%BNBT), and gradually deformed (already at 75°C for 6%BNBT, 7 and 9%BNBT at 100°C and 5%BNBT at 125°C), in excellent agreement with the literature[112].

The appearance of double hysteresis loops was suggested to indicate a transition between a FE phase and an AFE phase[28, 30, 33, 35, 36], or to result from the interaction between polar and non-polar regions, which co-exist in the ceramics at high temperatures[114]. In both cases, applied electric field may orient neighboring regions (in a unit cell scale in the case of AFE, or in the nano/micro scale in the case of polar regions) and hence result in hysteresis. However, as the field is removed, orientation would be lost (back to AFE phase, or "flip" to the starting polar region state), resulting in double hysteresis loops. In case the polar regions were at least slightly oriented before hand, remnant polarization wouldn't be completely zero and therefore remnant polarization would exist in the mixed phase.

4.5. Dielectric properties

4.5.1. Temperature dependent dielectric properties

The relative permittivity of samples, ε_r, and loss tangent, δ, were determined from capacitance measurements. In order to determine transition temperatures with a higher accuracy[115], measurements were conducted on poled samples, aged for at least 24 hours, at frequencies of 1, 10 and 100 kHz, upon heating the samples from 30°C to 550°C at 2°C/min.

Figure 4-5 illustrates the temperature dependence of the relative permittivity for 6%BNBT. Temperature dependent permittivity data for all compositions are presented in Appendix 4-1.

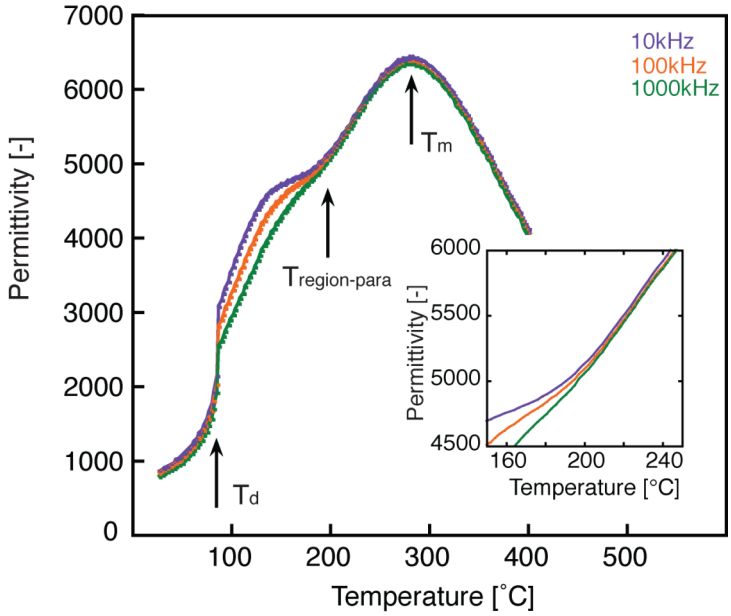

Figure 4-5 - Temperature dependence of relative permittivity of 6%BNBT. The inset offers an enlargement of the permittivity near the $T_{region\text{-}para}$ transition

The low temperature transition, indicated T_d, is the temperature above which pinched hysteresis loops have been observed (section 4.3), hence it has been associated to the depolarizing temperature. The region between T_d and $T_{region\text{-}para}$ is characterized by the dispersion of the dielectric permittivity with frequency, which is a typical behavior of relaxor ferroelectrics[116]. At these temperatures, the compositional disorder of the Bi^{+3}, Na^{+} and Ba^{+2} ions, does not allow long range ordering and therefore short rang ordering in the scale of microns create polar regions.

Each polar region has a slightly different relaxation time, determining the response the applied field. Hence maximum in the dielectric permittivity as a function of temperature is frequency dependent[117]. The anomaly indicated by $T_{region\text{-}para}$, is slightly dispersed (see enlargement in Figure 4-5) and seems to indicate the end of the relaxor region.

Many studies[28, 118-120] referred to the T_d-$T_{region\text{-}para}$ temperature zone as AFE even though inconclusive evidence of AFE phase have been found using XRD[33, 34, 37] and neutron diffraction[37]. From the beginning of the 90's, reports consider the possibility of coexistence of FE_R polar regions and T phase in BNT, acting as a relaxor material[29, 121-123]. These regions are stable at lower temperatures but diminish at higher temperatures. The existence of polar regions has been supported by pyroelectric measurements[39], time dependent electric permittivity[40], light scattering[124], as well as the diffused phase transition with frequency dispersion seen in dielectric measurements[124, 125].

The high temperature transition, indicated by T_m, is the temperature at which the permittivity reaches a maximum value and corresponds to a transition from possibly one P phase to a second P state.

4.5.2. Frequency dependent dielectric properties - Extrinsic contribution to permittivity

Non-poled cylindric samples (see chapter 3.3) were measured in the frequency range from 100Hz to about 7.8GHz and the real and imaginary parts of permittivity were measured for all compositions at room temperature (Figure 4-6). A separation between low concentration samples (below 5%BNBT) and high concentration samples (above 6%BNBT) can be clearly seen, with good agreement to the R and T phases, respectively. Both real and imaginary parts of the permittivity gradually increase with $BaTiO_3$ content, until at 6%BNBT they drastically jumps to as much as two times the value. Above this concentration, additional $BaTiO_3$ causes a slight decrease, as can be seen in Figure 4-7, for the real part at 1kHz.

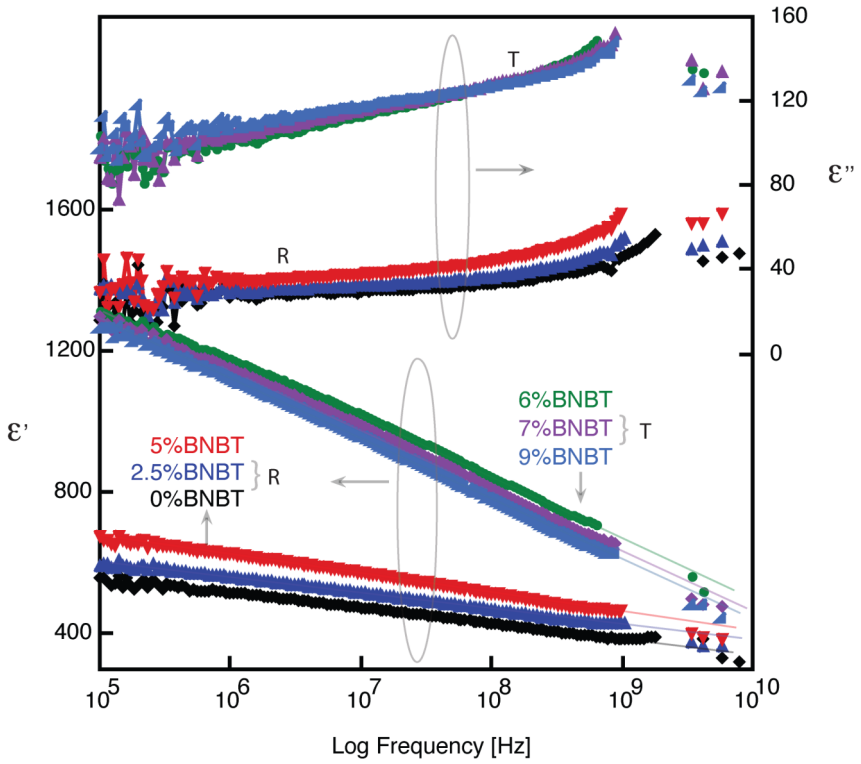

Figure 4-6 - High frequency real and imaginary parts of permittivity of BNBT samples

As frequencies increase (Figure 4-6), both the R and the T compositions show gradual decrease of the real part of permittivity and increase of the imaginary part. However, the T compositions exhibit a steeper slope in the real part then the R compositions. These slopes of the real part of permittivity, both in the R and T compositions, indicate a “soft” behavior.

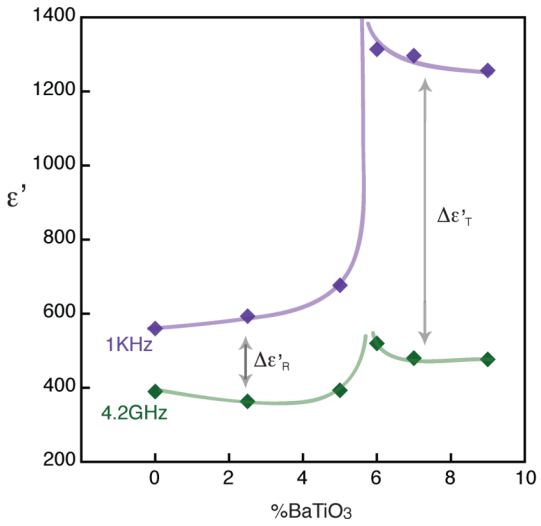

Figure 4-7 - Permittivity of all compositions at 1KHz and 4.2GHz

The lattice permittivity of ferroelectric materials, at around 10GHz, has been often observed to be significantly lower than the permittivity measured at conventionally accessible frequencies, as is seen in Figure 4-7.

The manifestation of this difference is often seen in a step-like dispersion of the permittivity accompanied by the loss peak in the frequency range 1-10GHz[113, 126].

Several mechanisms have been proposed to explain the possible origin of this dispersion ($\Delta\varepsilon'_R$ and $\Delta\varepsilon'_T$ in Figure 4-7 for R and T phases, respectively), including resonance of domain walls[127], translational vibration of domain walls[128], acoustic shear waves generation by stacks of lamellar 90° domains[129], and piezoelectric resonance of grains[130]. Large contribution of domain walls on the piezoelectric effect of $BaTiO_3$ were observed[131]. Some authors have proposed that the dispersion is related to motion of individual ions between off-center position[132].

Extrapolation of the real part permittivity measured below 1GHz to higher frequencies (plotted with light colors in Figure 4-6) shows a small deviation from the discrete measured data. In addition, imaginary part permittivity data close to 1GHz show an increase, which together with the discrete data indicate a very small peak in this frequency region. The big dispersion between the low and high frequency permittivities indicate that domain contributions to the permittivity are very big (at least $\Delta\varepsilon'_R \approx 250; \Delta\varepsilon'_T \approx 600$, compared to PZT[126] $\Delta\varepsilon'_{PZT} \approx 400$).

4.6. Resonance measurements

The piezoelectric behavior of BNBT could be studied using resonance measurements. The conductance (G) and the resistance (R) of 2.5%BNBT and 7%BNBT samples were recorded as a function of temperature from 25°C up to the temperature at which the resolution did not allow detection of the signals. Posting G_{max} and R_{max} together with permittivity data (Figure 4-8) shows clear correlations to the T_d and $T_{region\text{-}para}$ transitions discussed above.

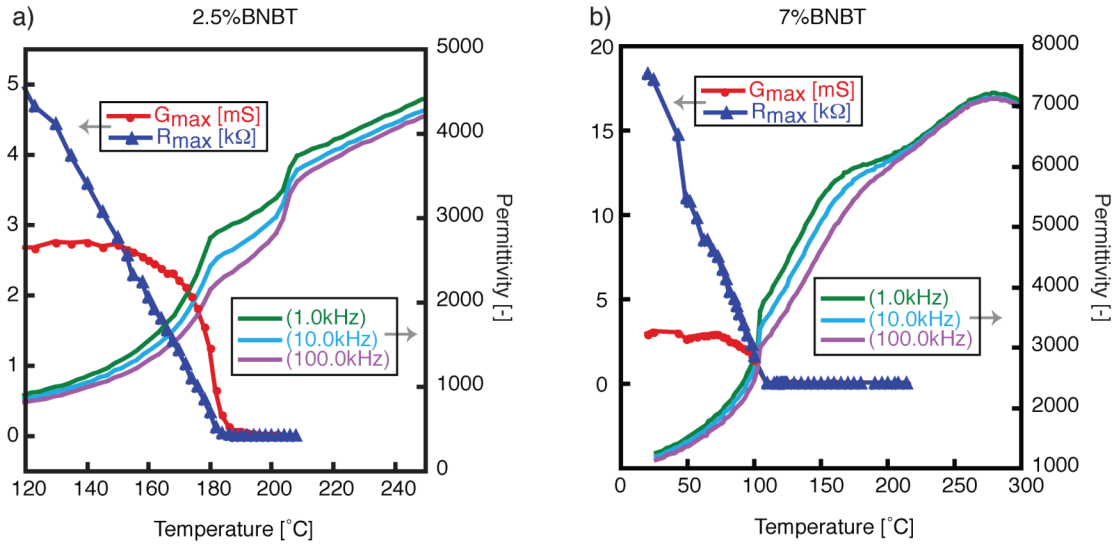

Figure 4-8 - Conductance, resistance and permittivity as a function of temperature for (a) 2.5%BNBT and (b) 7%BNBT

In good agreement to reports for BNT[133] drastic decrease of the G_{max} and R_{max} is observed as temperatures reach the T_d, and low signals could be detected up to $T_{region-para}$. Similar abrupt changes of the resonant and anti-resonant frequencies and the angle, were observed by Hiruma et al[120, 121] at the T_d and $T_{region-para}$ for xBNBT samples.

The sudden decrease of the piezoelectric resonance peak at T_d, corresponding to de-polarization, is caused by the transition from a FE phase. Traces of piezoelectricity above this transition confirm the existence of polar regions in a non polar matrix. The loss of a detectable signal at $T_{region-para}$ point to the shrinkage of the polar regions, and possibly, to their disappearance.

It should be noted that even though Hiruma at el, consider the existence of a mixed phase only up to $T_{region-para}$, they report resonance signals even above this temperature. No explanation was given to these results.

4.7. Raman spectroscopy

Raman spectra were taken on heating from (–197)°C to 320°C. Qualitative differences across phase boundaries were monitored, throwing light on the nature of the phases. No attempts were done to identify the normal modes responsible for the features ascribed to different phases.

In many cases the spectra across a phase boundary were clearly and qualitatively different, however, across some transitions the changes were more subtle. In order to characterize the changes with more sensitivity, the spectra were fitted with an appropriate number of Lorentzian lines (as can be seen in Figure 4-9 for 9%BT taken at 0°C). Signatures of phase changes were sought in the composition and temperature dependence of the line frequencies, widths and strengths.

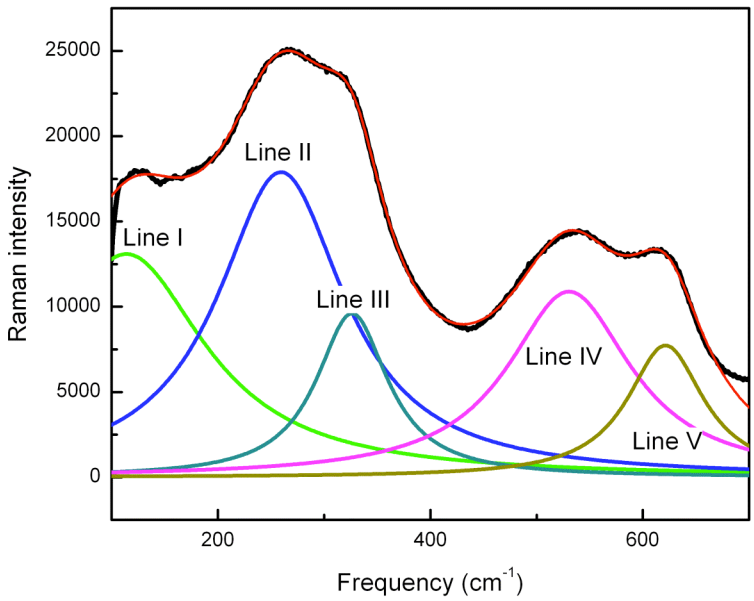

Figure 4-9 - Fitted Raman spectra of raw experimental data (upper thin red curve and thick black curve, respectively) 9%BNBT taken at 0°C, with appropriate number of Lorentzian lines (line I-V)

4.7.1. Temperature dependent cross sections

Raman spectra of all concentrations collected at constant temperature were compared, as is illustrated in Figure 4-10 for -195°C and 50°C (more temperature cross sections can be seen in Appendix 4-2).

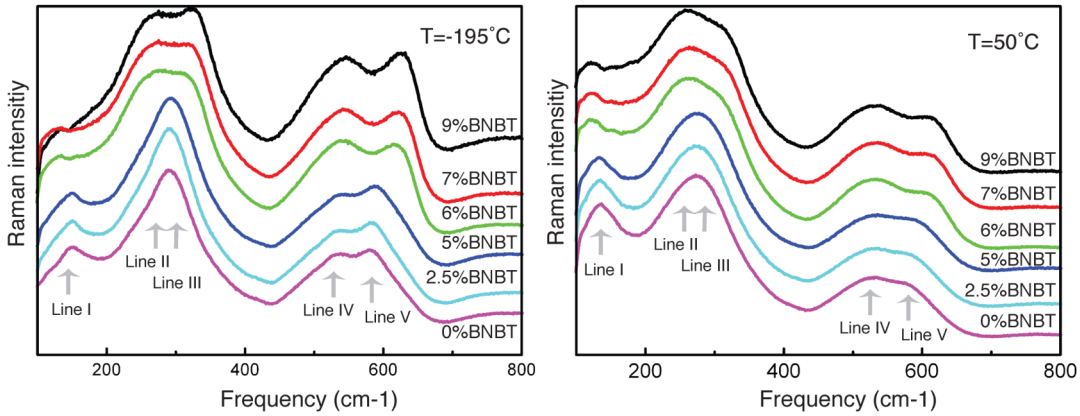

Figure 4-10 - Raman spectra of xBNBT collected at -195°C and 50°C. Lines I-V correspond to Figure 4-9

It can be easily seen in that a drastic change occurs between 5 and 6%BNBT: line I shifts to lower frequencies, lines II and III grow apart in frequencies and line V shifts to higher frequencies. These changes indicate a structural change in the unit cell and could be observed quantitatively from frequency, width and amplitude ratio, extracted from the fitted lines, as can be seen in Figure 4-11 (fitted data for other temperatures are given in Appendix 4-3). The change in the position of the peak (frequency change) is highlighted, whereas the changes in the width and amplitude ratios are characterized by an abrupt “jumps”.

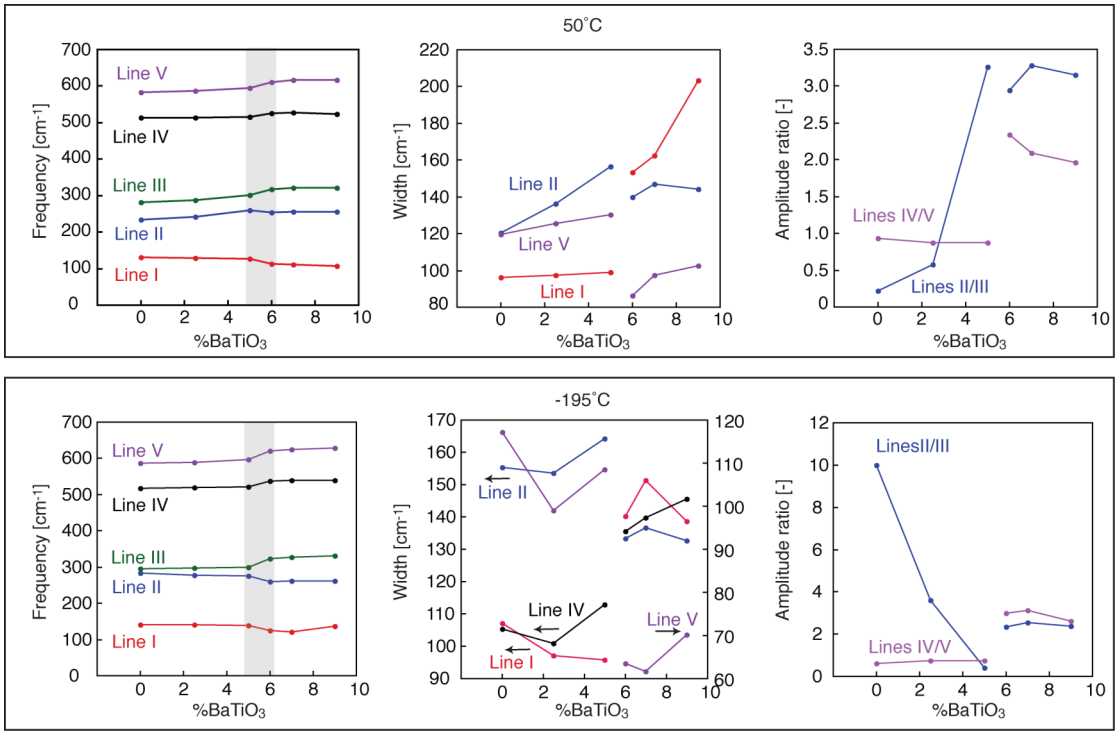

Figure 4-11 - Fitted Raman data presenting frequency, width and amplitude ratios of all compositions at 50°C and -195°C. Lines I-V correspond to Figure 4-9

All of the above indicate a phase transition between the low $BaTiO_3$ concentrations (below 5%BNBT) and the high $BaTiO_3$ concentrations (above 6%BNBT), corresponding to R and T phases found by XRD (see section 4.2). Since this phase transition range from -195°C and up to 50°C, it presents a perfectly vertical phase boundary, hence a morphotropic phase boundary (MPB).

4.7.2. Composition dependent cross sections

Close observation of the raw spectra (Figure 4-12a) of 5%BT reveals distinct changes of the spectra taken below 95°C and above 115°C. These changes could be clearly seen by sudden shifts of frequencies of fitted lines (Figure 4-12b), as well as by abrupt changes in width of these lines (Figure 4-12c), all of which indicate a phase transition above 95°C. These features coincide with the transition characteristics seen near the MPB, crossing from R to T phases. Higher temperature transitions could not be detected for this composition.

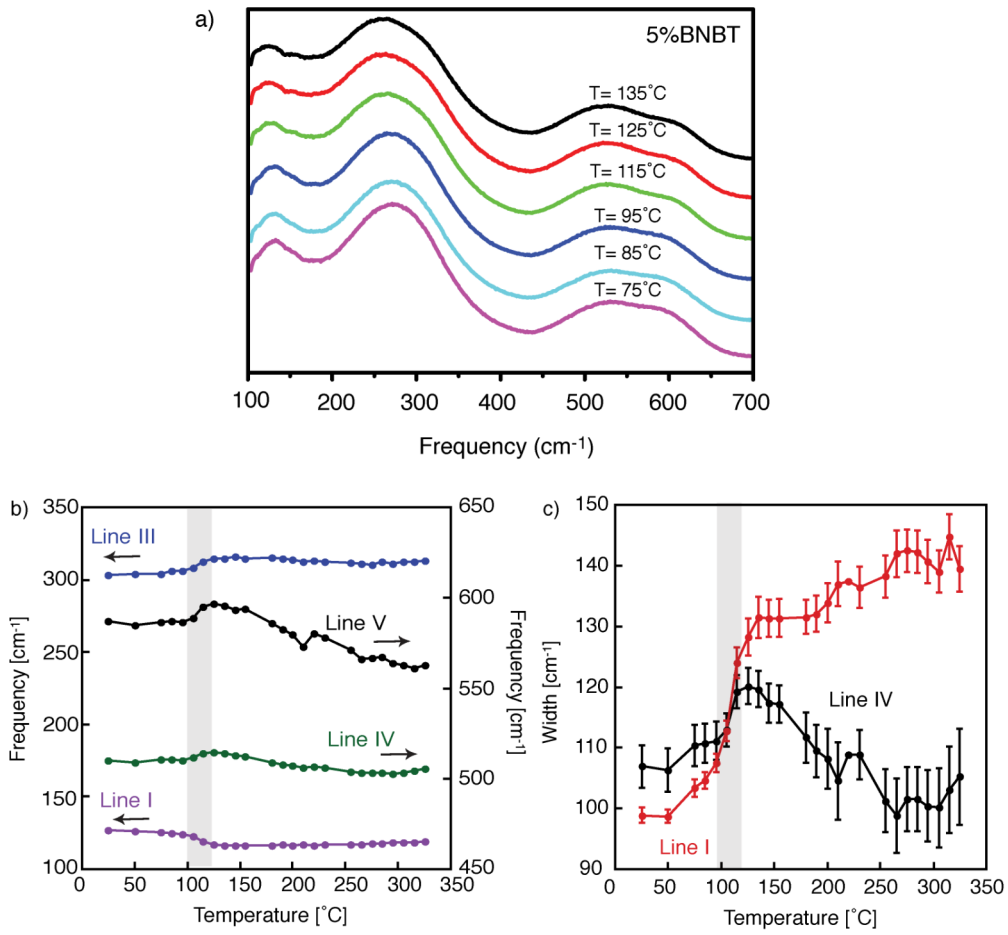

Figure 4-12 - (a) Raw Raman spectra of 5%BNBT near the T_d, (b) frequency and (c) width of fitted lines

However, similar investigation of Raman spectra and corresponding fitted data of low $BaTiO_3$ concentration, show different characteristics at the low temperature transition. As can be seen for 2.5%BNBT in Figure 4-13a, c and d (and for 0%BT in Appendix 4-4), although a change in the spectra can be observed, it is less abrupt than noted for 5%BNBT. Since both 5%BNBT and 2.5%BNBT were shown to have R phase at low temperatures, the different transitions features may imply a different high temperature phase.

In their paper, Hiruma at el[29] claim that very small lattice anisotropy seen by XRD, result in pseudocubic phase in compositions above 3%BNBT, in the temperature range between T_d and $T_{region\text{-}para}$. Different claims have been made as to the nature of the phase within T_d and $T_{region\text{-}para}$ for pure BNT. Ritveld neutron powder profile[134] indicated a T phase in this temperature range, whereas assigned peaks of Raman spectroscopy[135, 136] indicate an R phase. TEM investigations[137, 138] suggested a modulated phase separating an R phase and an orthorhombic phase.

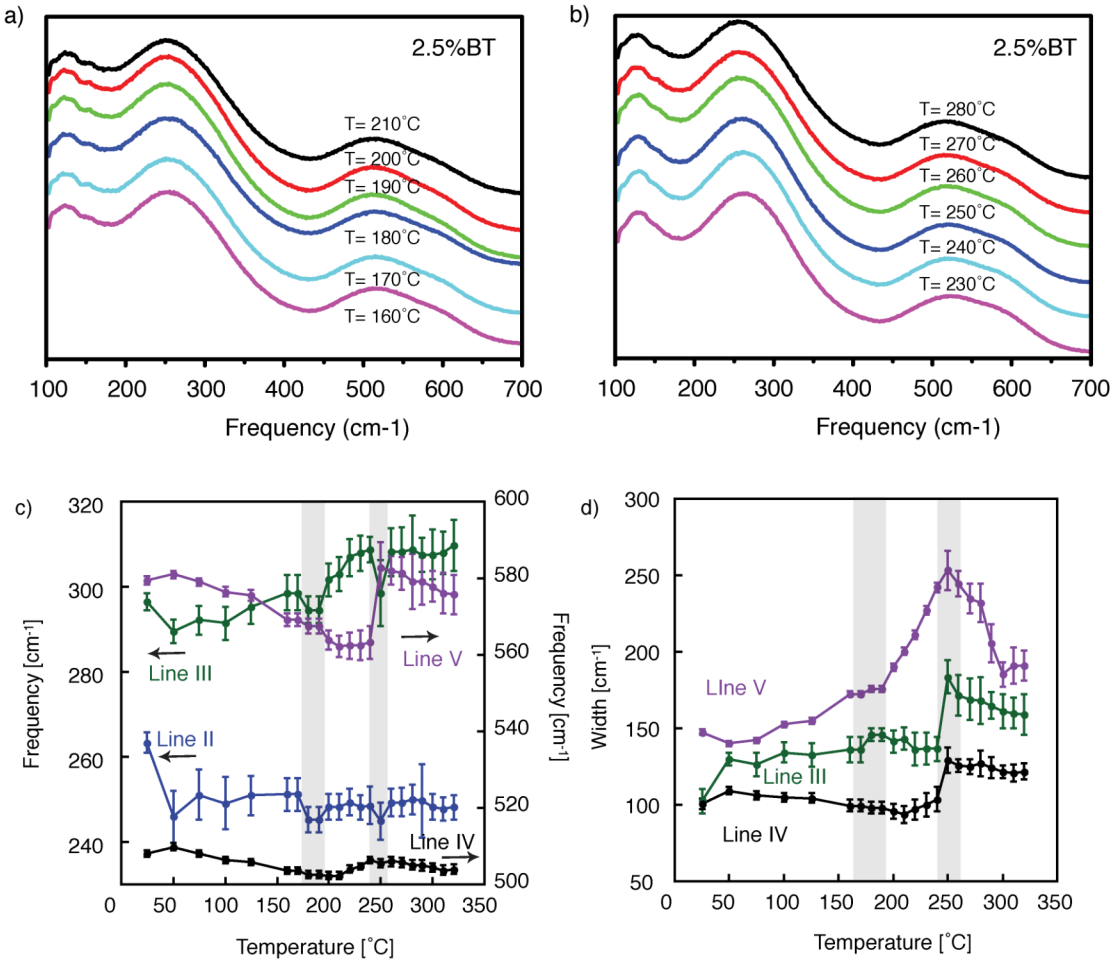

Figure 4-13 - Raw Raman spectra of 2.5%BNBT near (a) the Td and (b) the $T_{region\text{-}para}$, (c) frequency and (d) width of fitted lines

A second transition at the $T_{region\text{-}para}$ can be seen for 2.5%BNBT in Figure 4-13b, c and d, indicated by a change in some frequency peaks and in an abrupt change of the width of the fitted lines. Resembling features were observed in the spectra of compositions above 5%BNBT (as can be seen in Figure 4-14a, c and d for 7%BNBT and in the Appendix 4-5 for 6%BNBT and 9%BNBT). Therefore, it seems possible that the phases involved in these transitions have similar characteristics.

The transition at T_m was noted at 0%BNBT (Appendix 4-4), 6% and 9%BNBT (Appendix 4-5) and 7%BNBT (Figure 4-14) by an increase of the frequencies of the fitted data, and a change in the width of the peaks.

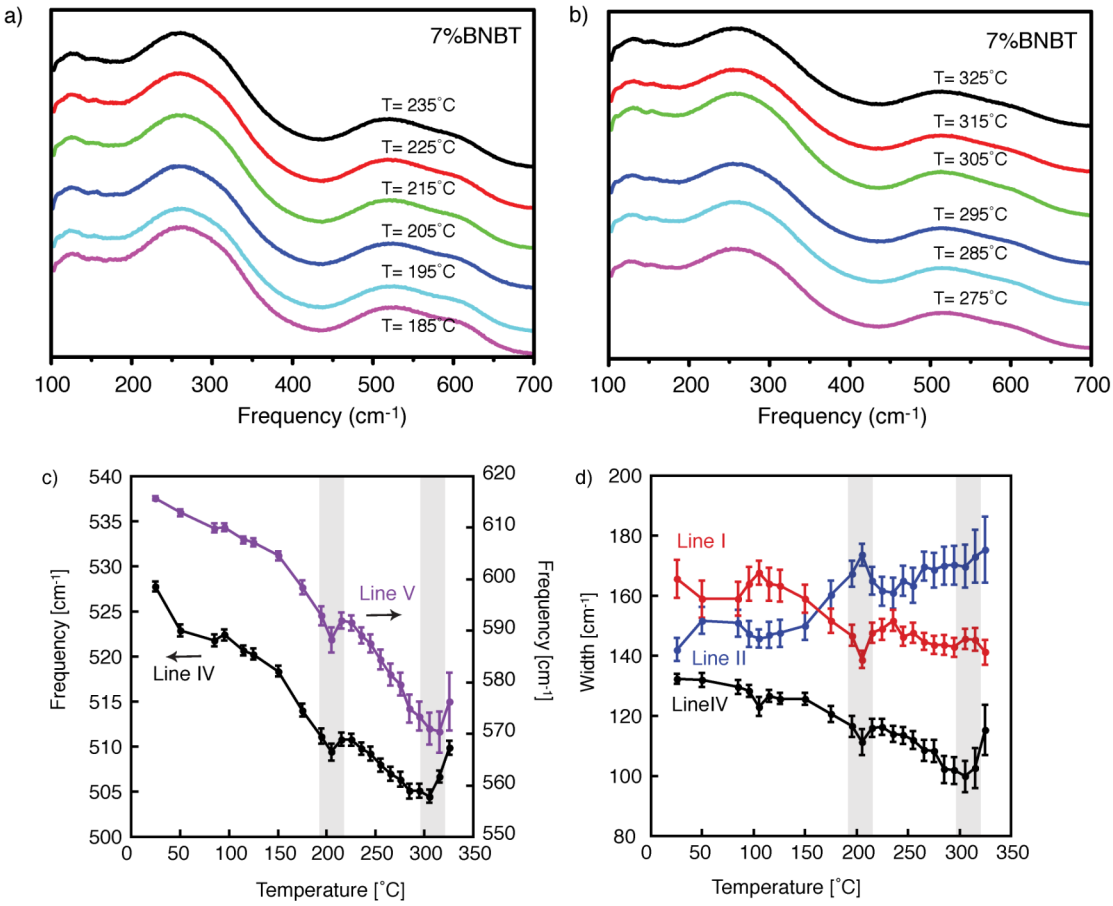

Figure 4-14 - Raw Raman spectra of 7%BNBT near (a) the Td and (b) the $T_{region\text{-}para}$, (c) frequency and (d) width of fitted lines

It should be noted that the transition at T_d could not be observed for compositions of 6 and 7%BNBT. As mentioned in the discussion of 5%BNBT sample, it seems reasonable that the phase above T_d in this composition is of T nature, with close features to the low temperature T phase, in compositions with >6%BNBT. Since the tetragonality of the phase near the MPB is low, indicated from the small tetragonal XRD signals (section 4.2), it is not surprising there are no significant changes in the Raman spectra when crossing the boundary between the two T phases: FE_T to T polar region mixed phase.

4.8. The phase diagram - summary

The transition temperatures and the nature of these transitions, discussed in sections 4.3-4.7, were put together to construct the phase diagram in Figure 4-15.

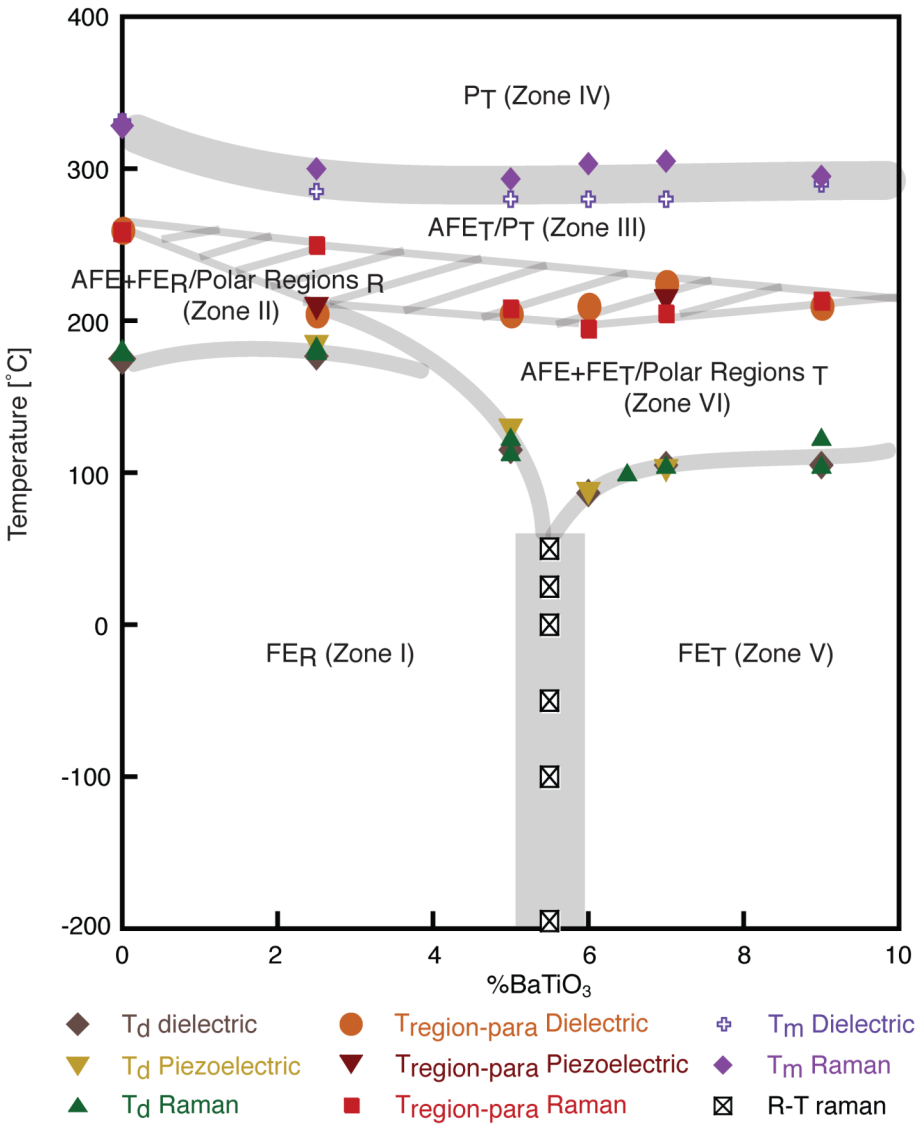

Figure 4-15 - Phase diagram of (1-x)BNT-xBT with 0<x<9% constructed from X-Ray diffraction, hysteresis loops, dielectric and piezoelectric measurements and Raman spectroscopy

XRD measurements (section 4.3) indicate rhombohedral and tetragonal phase, in zones I and V respectively, as was reported previously. Both phases show ferroelectric behavior, as was interpreted by hysteresis loops (section 4.4). Reinforcement to the existence of these two different regions was obtained by

frequency dependent dielectric measurements (section 4.5.2) and Raman spectroscopy (section 4.7.1). The last has also established the perfectly vertical MPB separating these two ferroelectric phases.

Due to pinched hysteresis loops (section 4.4), zones II and VI were postulated to be antiferroelectric phases. However, residual piezoelectric response (section 4.6) and a relaxor nature observed by temperature dependent dielectric measurements (section 4.5.1), suggest that these zones contain polar regions in a matrix which could be either antiferroelectric or paraelectric. Since hysteresis loops become flattened as temperature increases, it seems possible that the polar regions diminish until they no longer exist.

Comparison of the transition characteristics between zone I-zone V and zone I-zone VI, by Raman spectroscopy (sections 4.7.1 and 4.7.2), imply that the polar regions in zone VI are of tetragonal nature, whereas the polar regions in zone II are of rhombohedral nature.

Resonant response could not be observed in zone III, which suggests no piezoelectricity in this phase. Hence, this zone may be either anti-ferroelectric or paraelectric. It has been suggested in the literature that this phase is of tetragonal symmetry. Similar symmetry was claimed for the paraelectric zone IV.

The dashed lines separating zones II and VI from zone III indicate a gray area in which different measurement techniques gave slightly different transition temperature. While hysteresis loops, dielectric and piezoelectric measurements average the property across the whole sample, Raman spectroscopy studies only a hundred nanometer size diameter. Hence, small inhomogeneities in composition or in local temperature, could lead to slight variations in the transition temperatures. Resolution limits of the resonance response could have similar effect.

Appendix 4-1 – Temperature dependent dielectric data for all compositions

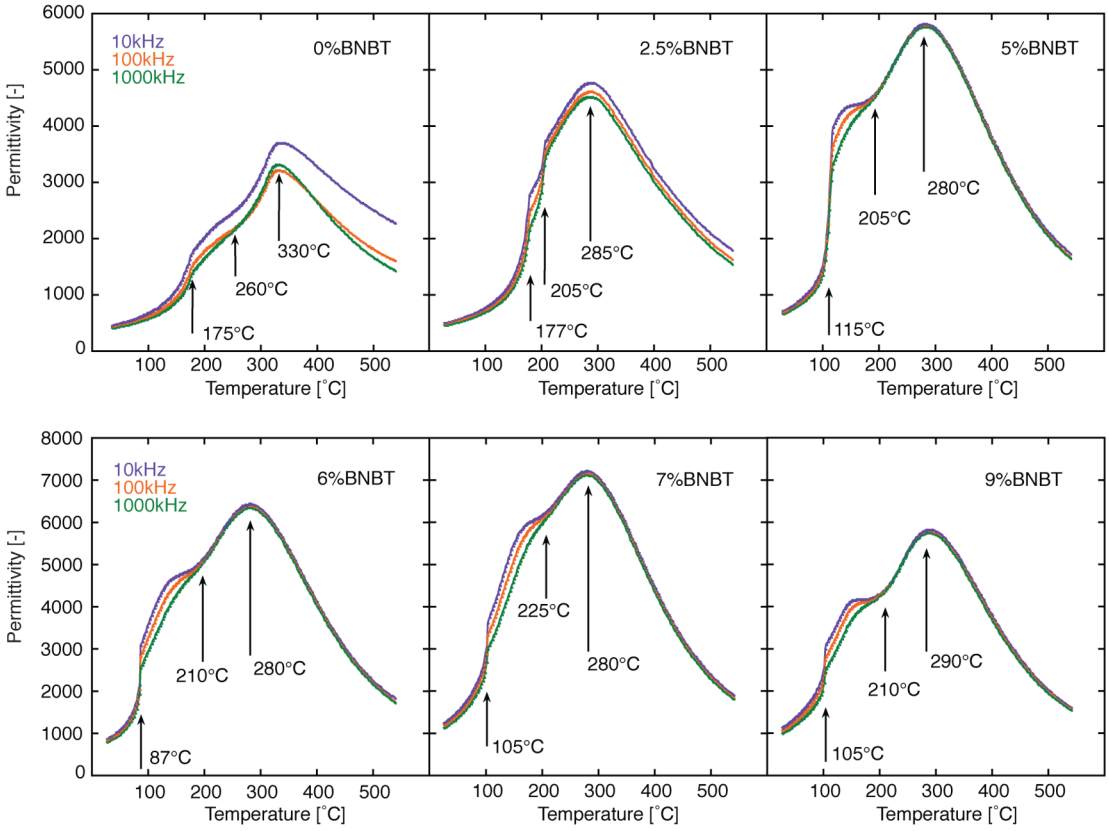

Appendix 4-2 - Raman spectra of all compositions at constant temperatures

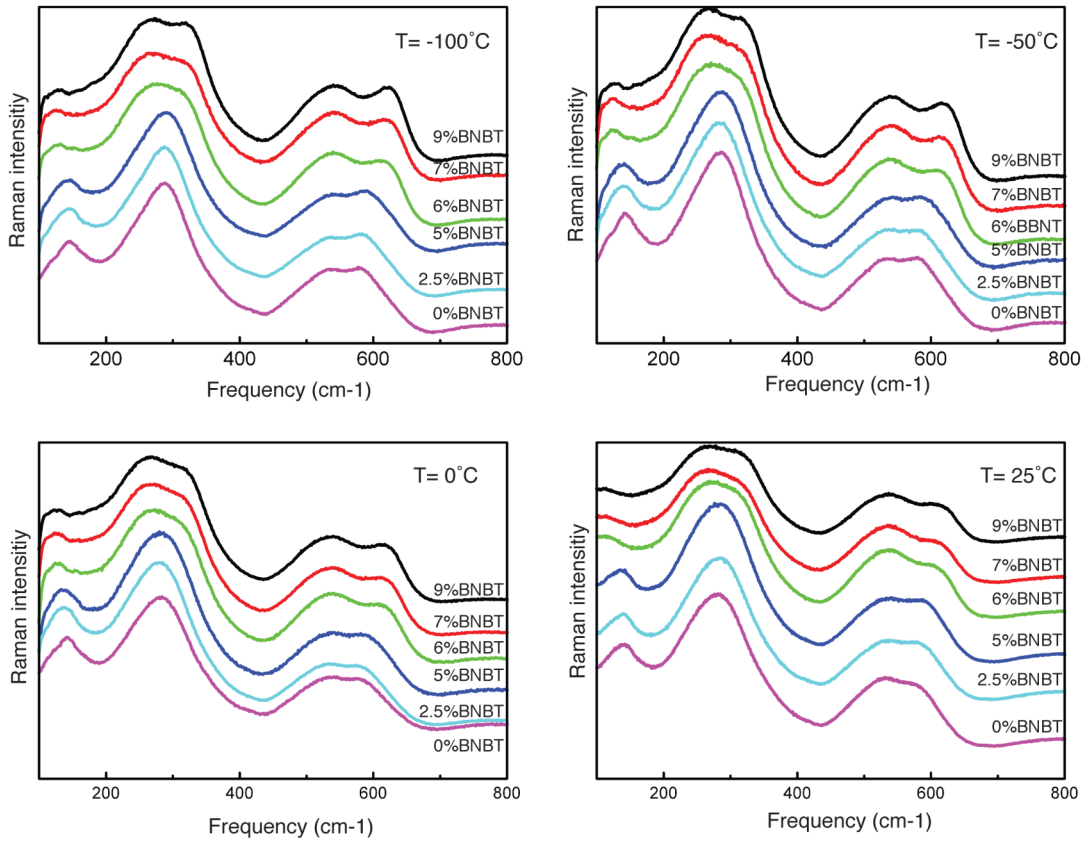

Appendix 4-3 - Fitted Raman data presenting frequency, width and amplitude ratios of all compositions at constant temperatures

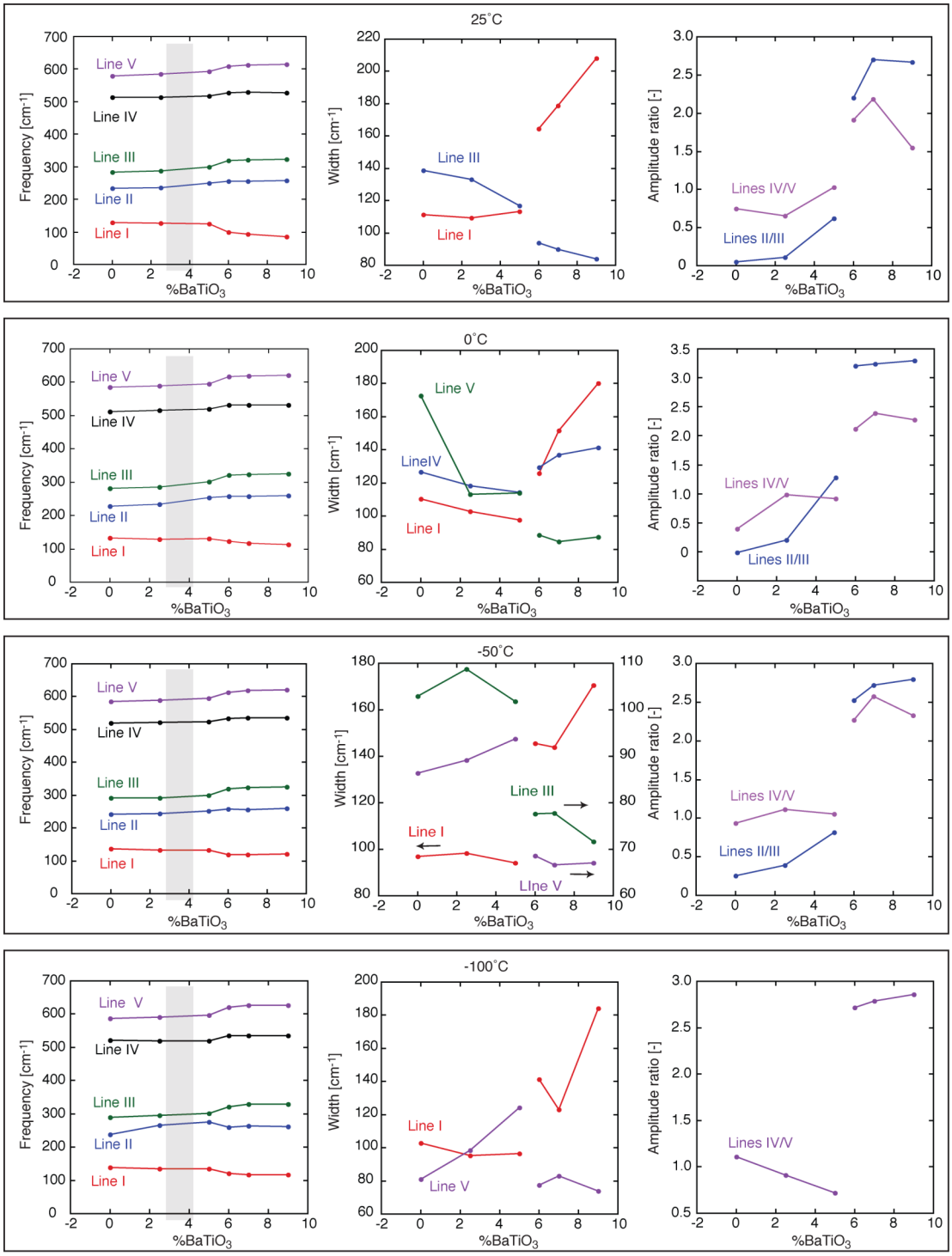

Appendix 4-4 - Raw and fitted data of 0%BT Raman spectra

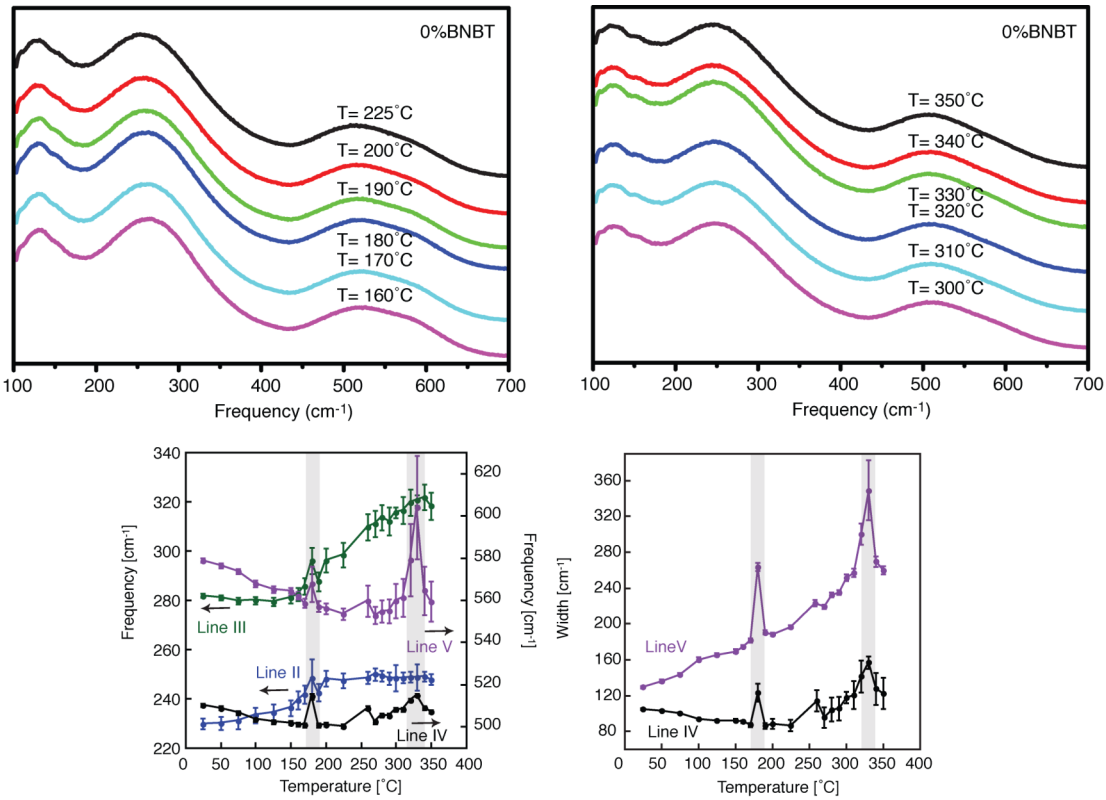

Appendix 4-5 - Raw and fitted data of 6%BT and 9%BT Raman spectra

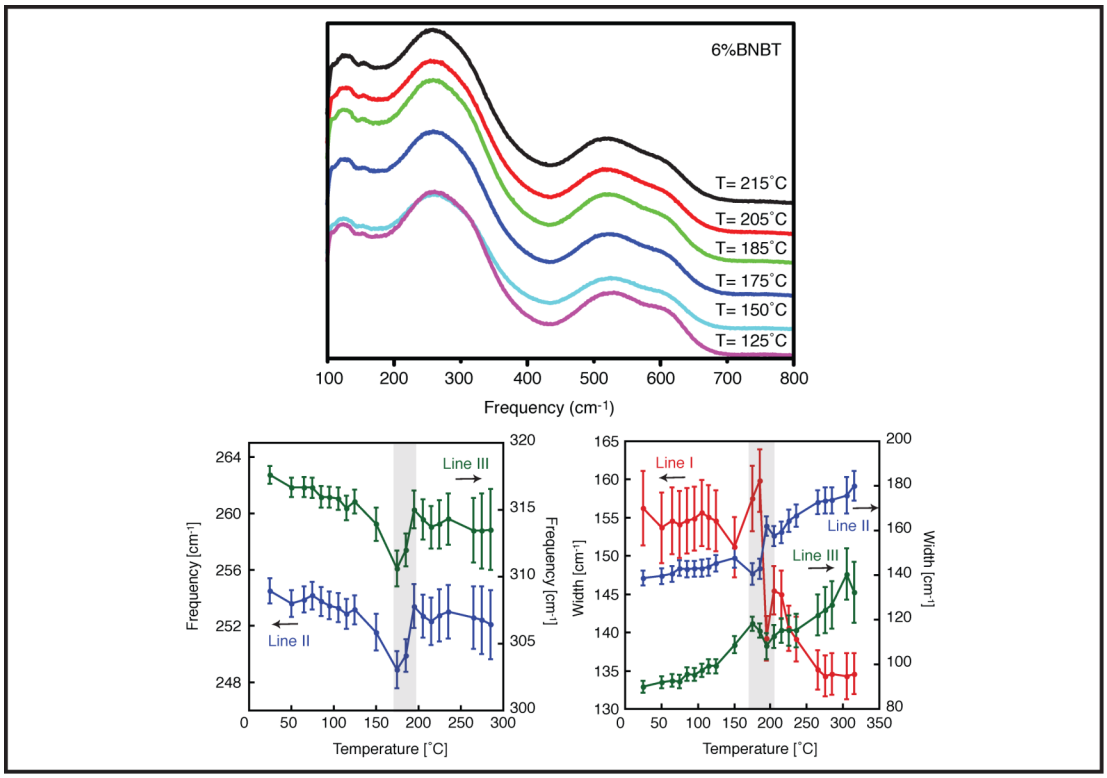

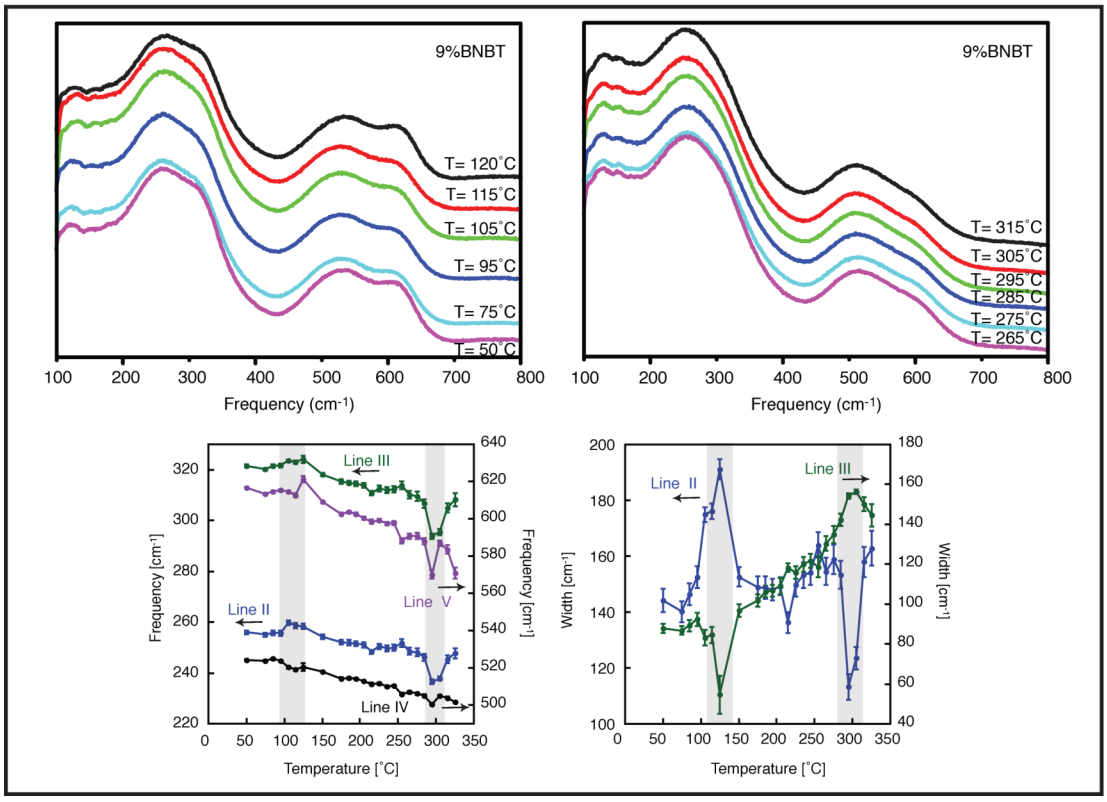

Chapter 5 - Processing and properties of KNLN

Conventional ceramic preparation, including sintering in air, was used to produce $(1-x)(K_{0.5}Na_{0.5})NbO_3$-$xLiNbO_3$ (xKNLN) ceramic samples with x=0.02-0.10. Planar and thickness coupling coefficients (k_p and k_t), piezoelectric d_{33} coefficient and permittivity were measured for 7%KNLN, showing lower properties compared to published ones. In addition, problems of reproducibility were observed. Comparison between two 7%KNLN samples was conducted using accumulative half hysteresis loops at different fields and temperatures. Measurements show similar behavior, though different maximum and remnant polarizations.

In order to improve properties, new 7%KNLN samples were prepared, with extra care on stoichiometry by using two new sintering approaches: controlling oxygen vacancies by sintering under oxygen atmosphere, and controlling alkali evaporation by powder buried, closed crucible sintering.

Comparison between two sintering approaches was conducted. Both procedures showed similar hysteresis behaviors and improved properties, providing up to 50% higher coupling coefficients than samples sintered in a conventional way.

5.1. Introduction

The need for reproducible lead free ceramics with high values, has led to numerous studies of the potassium sodium niobate system. Influence on the properties, of different parameters, including sintering heating rate[61], sintering temperature[62, 63] and poling conditions[64, 65], were discussed.

In this chapter, powder processing is described for $(1-x)(K_{0.5}Na_{0.5})NbO_3$-$xLiNbO_3$ (xKNLN) ceramics with x ranging from 0.02 to 0.10. The powders were sintered in air following published procedures. However, very low values of properties were found, together with non-reproducible maximum and remnant polarizations, measured for 7%KNLN samples by hysteresis loops.

In order to improve the properties, two sintering approaches, namely sintering under oxygen atmosphere, and powder buried, closed crucible sintering, were studied and compared for 7%KNLN.

5.2. Ceramic preparation

5.2.1. Powder and ceramic processing

The most common method for processing of ceramics of KNLN, is solid state synthesis from carbonates of potassium, sodium and lithium, and niobium oxide[60, 62, 64, 67-71, 139, 140].

$$K_2CO_3 + Na_2CO_3 + Li_2CO_3 + Nb_2O_5 \rightarrow (K,Na,Li)NbO_3 + CO_2\uparrow$$

High purity raw powders, K_2CO_3 99.997%, Na_2CO_3 99.997%, Li_2CO_3 99.999% and Nb_2O_5 99.9985%, were used to minimize impurities in the final product. Each powder was separately milled using attrition mill (650rpm) with ZrO_2 balls and isopropanol, in order to reduce and homogenize the particle size to optimized distributions[141] (Table 5-1). It was shown that K_2CO_3 particles form clusters when milling time was increased, therefore particle size could not be further reduced.

Raw powder	Milling time [hours]	Mean particle size $d_{v,0.5}$ [μm]
K_2CO_3	3	4.08
Na_2CO_3	2	2.81
Nb_2O_5	3	2.91

Table 5-1 - Attrition milling times of raw powders for homogeneous mean particle sizes

To avoid deficiencies in composition caused by absorbed water, the raw powders were dried at 200°C before they were weighed according to the desired composition.

A two-step milling was used ensuring homogeneous mix of the precursors. In the first step the A site precursor powders (K_2CO_3, Na_2CO_3 and Li_2CO_3) were mixed via ball milling (97rpm) with the aid of ZrO_2 balls for 24 hours in isopropanol. In the second step, the B site precursor powder (Nb_2O_5) was added to the slurry with additional isopropanol and ZrO_2 balls and the mixture was milled for another 24 hours.

Humidity in the precursor powders during powder processing has been shown by Hagh et al[142] to affect the piezoelectric properties of sintered $(K,Na,Li)(Nb,Ta,Sb)O_3$ ceramics. This is probably due to the effect of residual molecules of water which are absorbed by the hygroscopic K_2CO_3, and which at high temperatures decompose to free hydrogen. Therefore, extra care should be taken to avoid humidity.

During the powder processing, isopropanol with up to 0.2% H_2O was used as solvent for mixing and milling. Even though the isopropanol was evaporated from the powders before calcinations, residual water molecules were still likely to be absorbed. Therefore, in order to ensure dry precursor powders before the reaction starts, two-heating-step calcination was applied. In the first step the powders were kept at 200°C for 5 hours and only then, as a second step, the powders were calcined at 800°C for 4 hours (see schematic illustration in Figure 5-1). The powders were attrition milled for 3 hours with ZrO_2 balls in isopropanol before and after a second two-heating-step calcination was conducted.

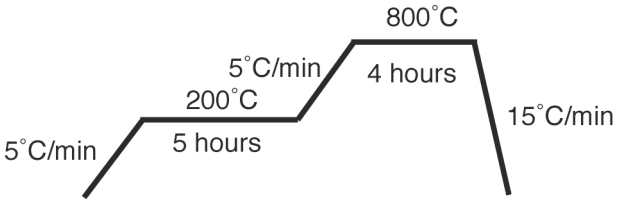

Figure 5-1 - Schematic profile of one calcination cycle

Figure 5-2 presents X-ray diffraction (XRD) spectra of 5%KNLN powder after the first calcination showing KNLN perovskite peaks in addition to peaks, indicated by arrows, correlated with the phases $NaKCO_3$ (ICDD 00-045-0871), $KNaCO_3 \cdot 6H_2O$ (ICDD 00-038-0705), $K_2Nb_8O_{21}$ (ICDD 00-031-1060) and $K_3LiNb_6O_{17}$ (ICDD 00-036-0533). These second phases disappear after the second calcination to give perovskite peaks solely (indexed in the figure).

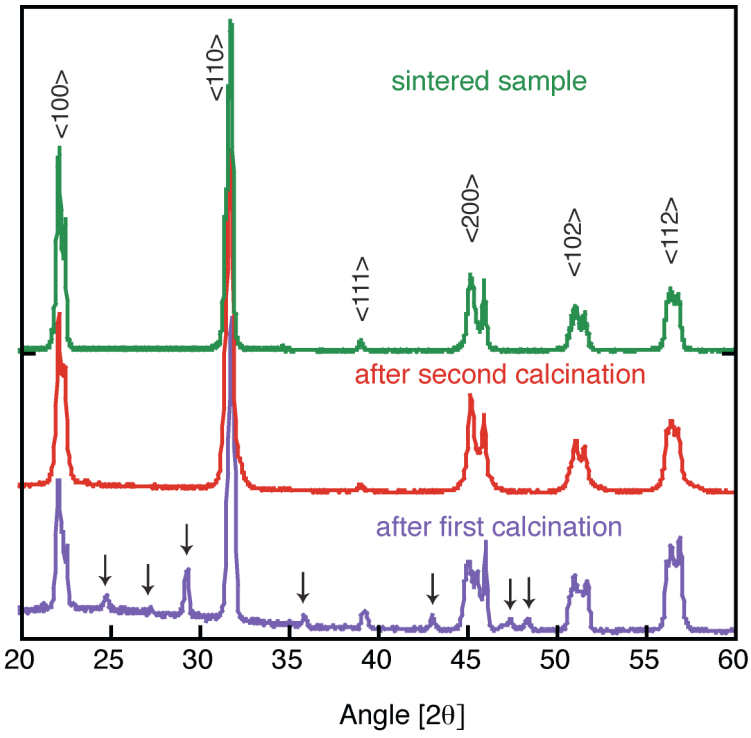

Figure 5-2 - X-ray diffraction spectra of KNLN 5% powder after first and second calcinations and after sintering. Perovskite phase is present (indexed) and arrows indicate second phases seen after the first calcination

The final powders were pressed to 7mm and 9mm diameter pellets with 2-5kN and sintered in air at temperatures ranging between 1055°C and 1095°C with a heating rate of 5°C/min[61] and a dwell time of 10 minutes (sintering profile illustrated in Figure 5-3). Sintering temperatures of the different compositions, summarized in Table 5-2, were optimized to meet highest densities with minimum grain growth.

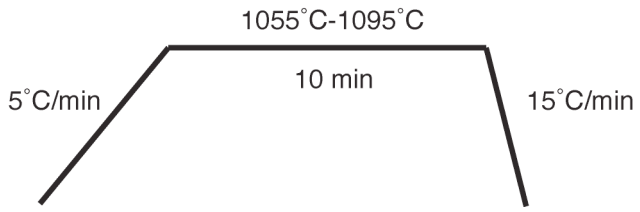

Figure 5-3 - Schematic profile for sintering KNLN ceramics

Densities of the samples were calculated according to their measured dimensions and weights. Theoretical densities were calculated using lattice parameters extracted from XRD, and known ratios of atomic masses. Errors of 0.1% in the lattice parameters would cause similar errors in the calculated densities, which would explain the irregular trend between compositions. Table 5-2 summarizes the averaged densities of 8-16 samples from each composition, showing small deviations between samples as well as between compositions.

x%KNLN	2	3	4	5	6	7	8	9	10
Sintering temperature [°C]	1095	1090	1085	1080	1075	1070	1065	1060	1055
Theoretical density [gr/cm3]	4.49	4.49	4.49	4.48	4.50	4.50	4.49	4.50	4.49
Averaged density [gr/cm3]	4.16	4.18	4.14	4.25	4.21	4.22	4.19	4.22	4.23
Averaged density [%]	92.75	93.12	92.19	94.79	93.58	93.81	93.42	93.80	94.19
STDEV [%]	1.02	3.54	1.12	1.04	2.07	1.41	1.44	1.18	1.07

Table 5-2 - Sintering temperatures and averaged densities of xKNLN ceramic samples with x=2-10%

In agreement with the results of Guo et al[60], XRD reveals gradual trace appearance of a secondary phase of tungsten bronze $K_3Li_2NbO_{15}$, for xKNLN with x>7%. Since the detection limit of XRD is about 3-5%wt (depending on the square root of the count time), it is estimated that for 10%KNLN, exhibiting the biggest second phase peaks (see Figure 5-4), this phase is present only in a few percent.

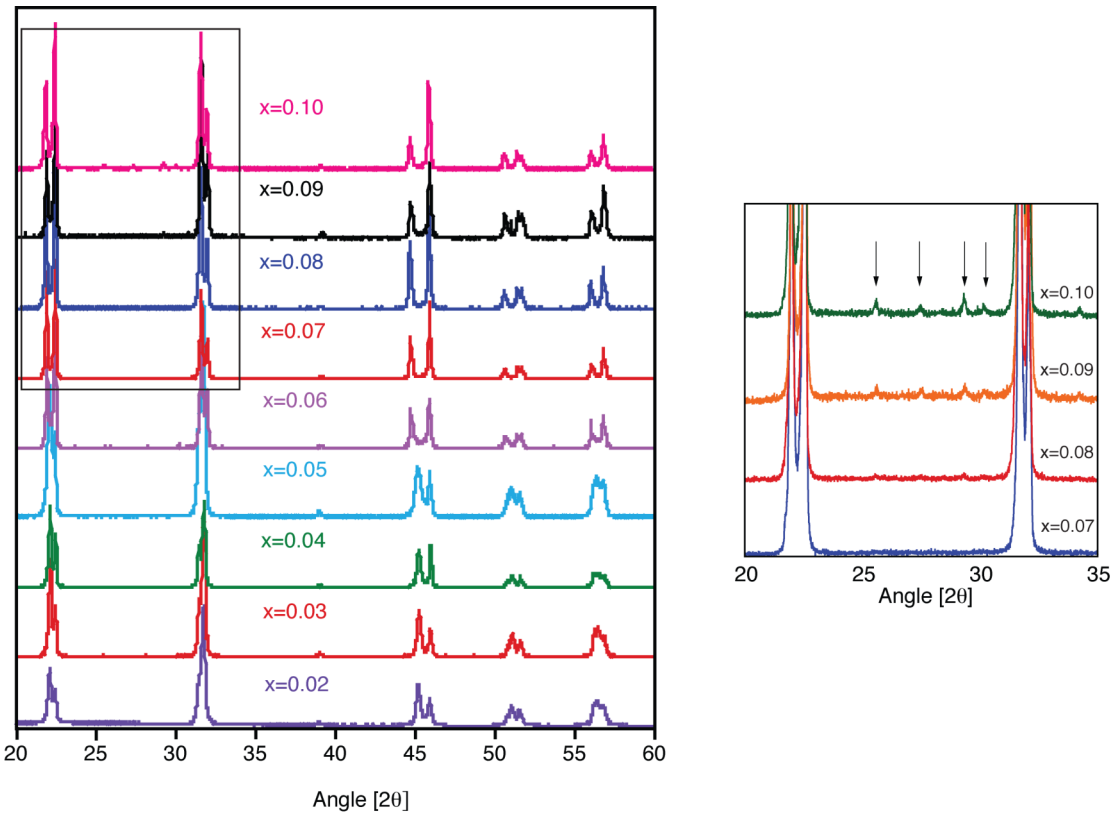

Figure 5-4 - X-Ray diffraction spectra of sintered KNLN with x=0.02-0.10. The square indicates the enlarged area, showing a gradual appearance of traces of a secondary phase. The secondary phase peaks are marked by arrows.

The compositions 4-8%KNLN where analyzed using Inductively Coupled Plasma Mass Spectrometry. Each composition was sampled on 4-15 random spots, of ø=30μm and ø=60μm for chemical homogeneity. The difference between measured and nominal concentrations was less then 1at% for Li. The samples were slightly deficient in K and Na, up to 2at%, but with K/Na ratio equal to the nominal (see Appendix 5-1 for a calculation example of 7%KNLN).

Fracture surfaces of all compositions were investigated using SEM. Homogenous square grains were observed and their average size was estimated to be about 5 μm, as demonstrated in Figure 5-5 for 3%KNLN.

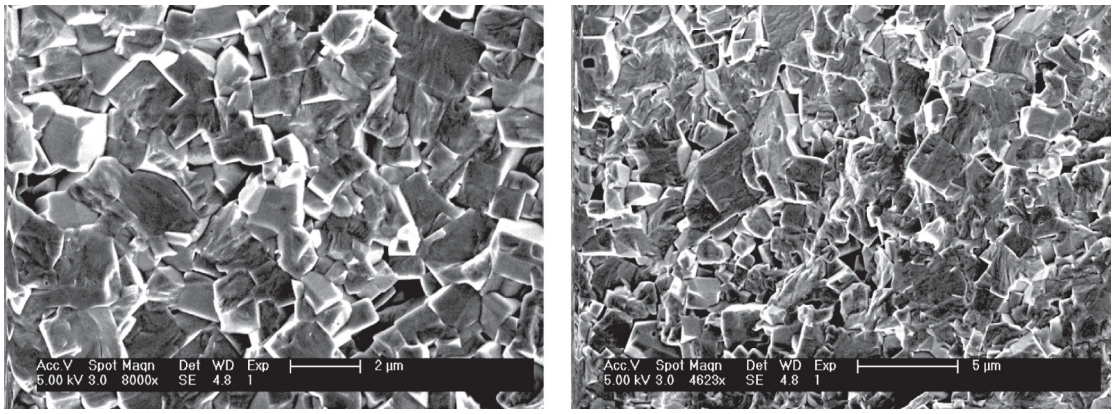

Figure 5-5 - SEM images of the fracture surface of 3%KNLN

5.2.2. Dielectric and piezoelectric properties

Accumulative half hysteresis loops, where only positive field was applied, were measured on one chosen composition, 7%KNLN, due to its interesting published properties. These measurements were conducted in order to investigate reproducibility of the samples, while accumulatively being poled, each step monitored and recorded. The sintered samples were polished with carbon paper up to 1000 grade (~18μm particles) and coated with chrome-gold electrodes by sputtering on the parallel surfaces.

Accumulative half hysteresis loops were measured on the same sample with increasing fields, from 10kV/cm to 50kV/cm, with steps of 10kV/cm. The field was always applied to the same direction relative to the same face, to ensure poling to one constant orientation. In addition no steps, such as heating, were made to depolarize the sample between each measurement.

Figure 5-6a and b illustrates accumulative half hysteresis loops measured on two samples at room temperature. Both samples show narrow loops, with small remnant polarization and significant back switching (indicated in the figure with arrows).

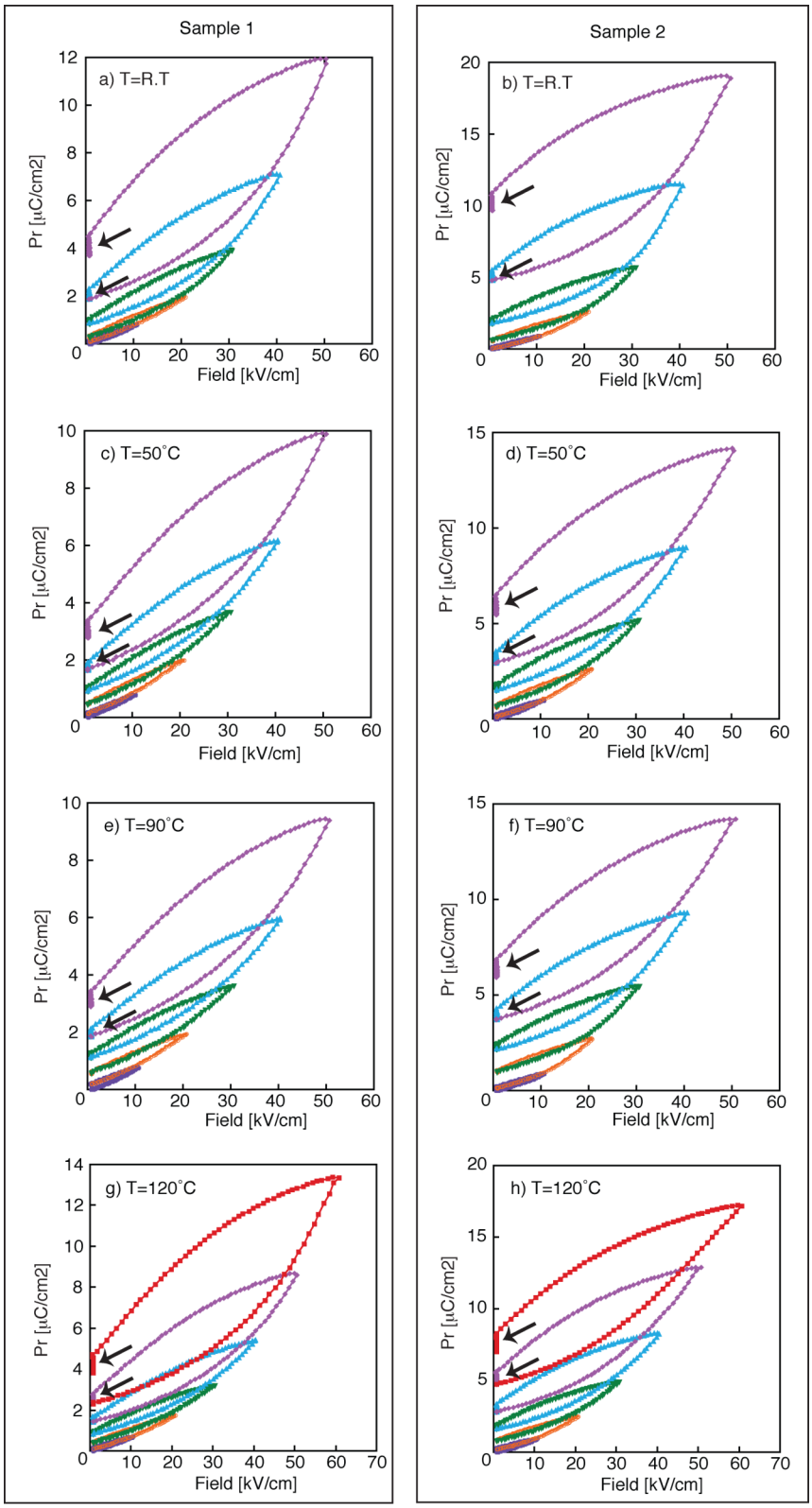

Figure 5-6 - Accumulative half hysteresis loops with increasing fields up to 60kV/cm, of two KNLN samples with x=0.07 at (a,b) room temperature, (c,d) 50°C, (e,f) 90°C and (g,h) 120°C. The arrows indicate relaxations of the remnant polarizations.

The samples were heated to 50°C (Figure 5-6c and d), 90°C (Figure 5-6e and f) and 120°C (Figure 5-6g and h), in order to study the temperature effect on similar accumulative half hysteresis loops. Uniform behavior is clearly seen in both samples. However, maximum and remnant polarization differ up to 50%.

Since only positive field was applied during the measurements, the samples were partially poled. The permittivity and coupling coefficients, k_p and k_t, were measured at each temperature after the "accumulative hysteresis poling" at 50kV/cm. Very low coupling coefficients were found (as can be seen in Figure 5-7) for both samples, even though an order of magnitude separate them.

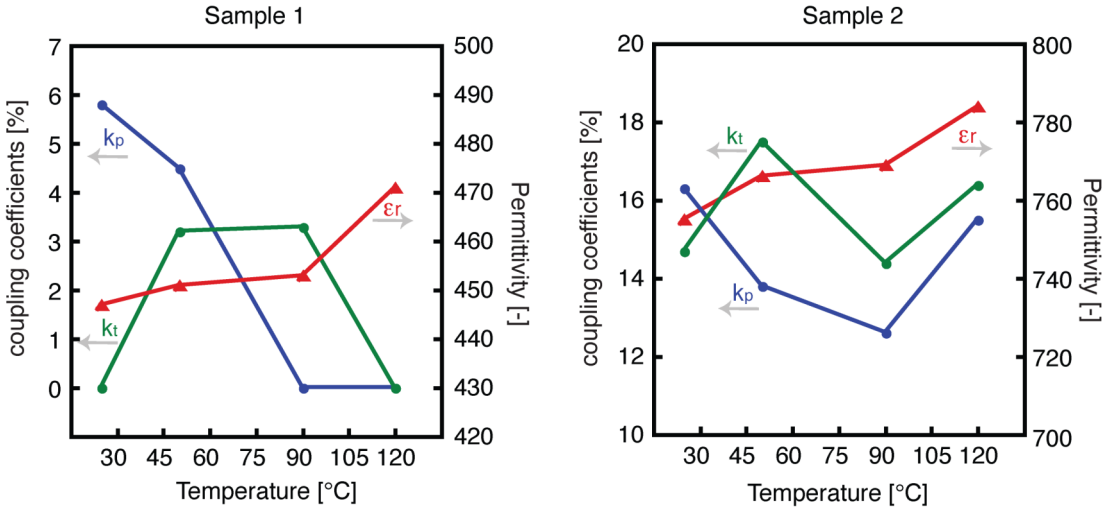

Figure 5-7 - Coupling coefficients and permittivity measured after accumulative half hysteresis loops at various temperatures for two KNLN samples with x=0.07

As expected, poling of a new sample at room temperature with 50kV/cm for accumulated times (up to 75 minutes), increased the coupling coefficients (Figure 5-8). Yet, even after poling the sample for 75 minutes these properties are sill poor, compared to published properties for same KNLN composition (Table 5-3). Since the coupling coefficients were so poor, no attempts of measuring the piezoelectric coefficients were made.

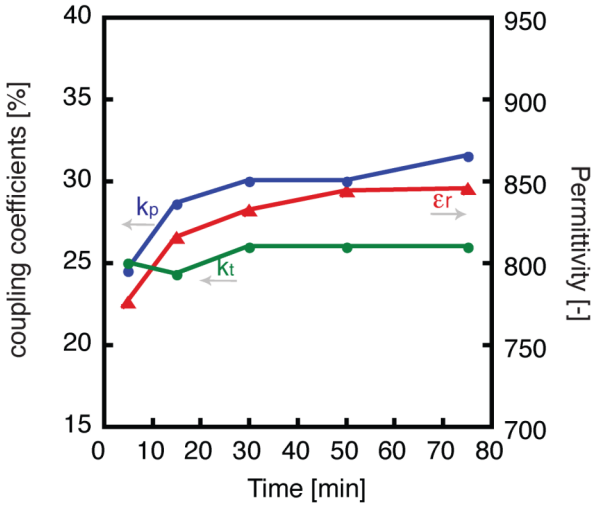

Figure 5-8 - Coupling coefficients and permittivity measured after accumulative poling at room temperature, under 50kV/cm at accumulative times

Source	k_p [%]	k_t [%]	d_{33} [pC/N]
Du et al[65]	46.0	-	274
Wang et al[143]	35.2	-	195
Du et al[63]	37.5	40.0	197
Tang et al[62]	35.4	-	172
Hollenstein et al[71]	45.0	51.0	240
Guo et al[60]	38.0	44.0	200
Literature average	39.5±4.8	45.0±5.6	213±37
"hysteresis poling"	15.5	16.4	
Conventional poling	31.5	26	

Table 5-3 - Coupling coefficients from the literature and as measured in this work

Two different explanations for the low values of properties have been suggested in the literature. The first explanation may be the small deficiency (up to 2at%) in K and Na mentioned in section 5.2.1. Alkali oxides volatilize easily during sintering at high temperatures, due to their high vapor pressures. This may cause deficiencies in stoichiometry and as a consequence, could lead to low values.

A possible way to avoid volatilization is to use double-crucible sintering technique, in which green pellets were buried in powder of the same chemical composition and covered by a reversed crucible that was further sealed by ZrO_2 powder[69, 70, 144]. Vapor pressure is created by volatilization of the surrounding powder and kept constant due to the sealed packing. As a result, minimal additional volatilization of alkali elements takes place from the green pellets.

The second explanation for the low measured properties is based on the work published by Shigemi and Wada[145, 146], in which the formation energies of neutral K, Na, Nb and O vacancies in $KNbO_3$ and $NaNbO_3$ were calculated. Their calculations showed that the formation energies of potassium and sodium vacancies increased as conditions changed from oxidizing to reducing, whereas the formation energies of oxygen vacancies decreased. In other words, the formation of oxygen vacancies diminish while alkali vacancies are formed in oxidizing conditions.

Oxygen vacancies in the structure act as pinning points, which restrict domain wall motions[142], and which in turn, limits domain switching. This results in insufficient poling and poor piezoelectric properties. Sintering in an oxygen rich atmosphere was reported to improve properties by Hagh at el[142] for $(K,Na,Li)(Nb,Ta,Sb)O_3$ ceramics and Birol et al[50] for $KNbO_3$ ceramics.

Hence, controlling the stoichiometry seems crucial in order to improve properties.

5.3. Sintering modifications

In order to improve the properties of the samples, and investigate and compare the two sintering approaches mentioned above, new ceramic samples of 7%KNLN were prepared.

Green pellets were prepared according to the procedure described in section 5.2.1, and were sintered in one of the following ways:

1. Samples were buried in powder of the same composition and placed in an alumina crucible. A top alumina disk was used to cover the alumina crucible, so that the vapor pressure would be kept. Samples sintered this way will be further referred to as “covered samples”.

2. Samples were placed on a Pt foil and placed in a tube furnace. Oxidizing atmosphere was obtained with a regular supply of oxygen. Samples sintered this way will be further referred to as "oxidized samples".

In both methods, samples were sintered with the same sintering profile (Figure 5-9).

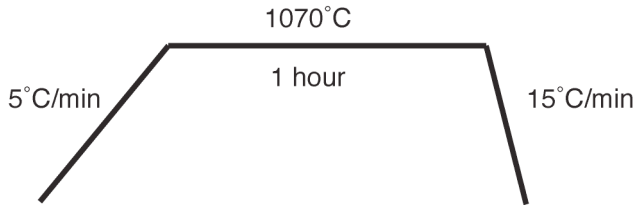

Figure 5-9 - Sintering profile of oxidized and covered samples

Densities of both covered and oxidized samples were calculated according to their dimensions and weights. Table 5-4 presents the averaged densities of 8-10 samples, showing only small deviations between the two sintering methods.

Sample	Theoretical density [gr/cm^3]	Averaged density [gr/cm^3]	Averaged density [%]
Oxidized	4.50	4.26±0.13	94.87±2.81
Covered	4.50	4.12±0.07	91.56±1.60

Table 5-4 - Densities of oxidized and covered sintered samples

The sintered samples were polished with carbon paper up to 1000 grade (~18μm particles) and coated with chrome-gold electrodes by sputtering on the parallel surfaces.

Accumulative half hysteresis loops were measured with fields from 10kV/cm to 50kV/cm at room temperature, giving close behaviors for samples of each sintering method (Figure 5-10a and b). Only small back switching can be seen in the remnant polarizations, as opposed to the large back switching observed in air sintering (Figure 5-6), indicating a smoother domain wall movement and more efficient switching. The

progression in properties, as measured after each half hysteresis, is similar in both samples (Figure 5-10c and d).

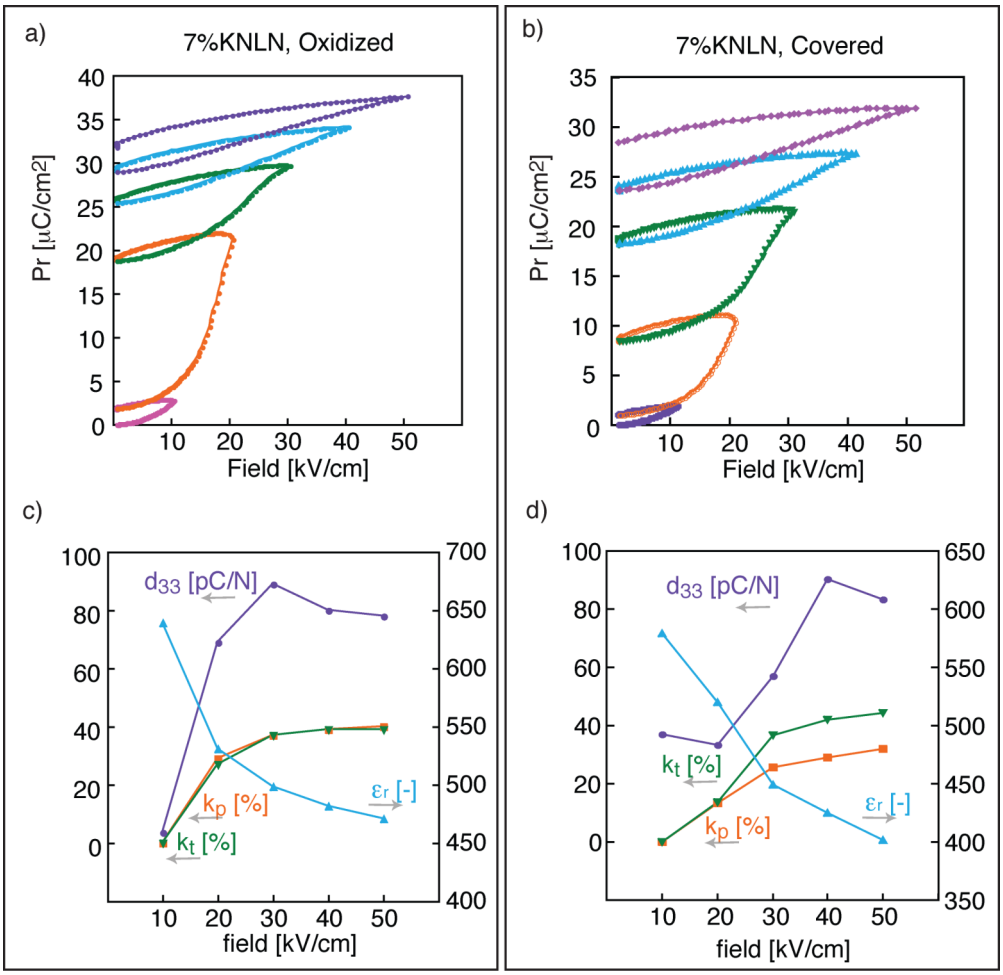

Figure 5-10 - Accumulative half hysteresis loops of (a) oxidized and (b) covered KNLN with x=0.07, and measured properties after each hysteresis (c and d)

Since the remnant polarization is much higher then in air sintered samples ($Pr \approx 10 \mu C/cm^2$ vs. $Pr \approx 33 \mu C/cm^2$), and nearly no back switching was observed, high values are expected. Table 5-5 summarizes the properties measured for oxidized and covered samples showing similar values. Permittivity and coupling coefficient (k_p) values are close to those reported by Niu et al[70]. However, the piezoelectric coefficient (d_{33}) is significantly smaller then reported elsewhere.

Sample	ε_r [-]	k_p [%]	k_t [%]	d_{33} [pC/N]
Oxidized	586±199	39±2	43±3	100±30
Covered	641±197	32±5	42±6	102±32
Reported for covered sample [70]	874	44	-	190
Oxidized – re-measured	908±252	38±3	44±5	71±23
Covered – re-measured	855±188	29±7	38±8	72±32

Table 5-5 - Properties measured on oxidized and covered samples, directly after "hysteresis poling" and about 4 months later

Re-measurements of the samples three to four months after the "hysteresis poling", show dramatic decrease for the piezoelectric coefficient and an increase in permittivity (Table 5-5). Both coupling coefficients exhibit no notable changes.

Aging was previously observed for conventionally sintered[50] KNN, (K,Na,Li)NbO_3 ceramics[141] and (K,Na,Li)(Nb,Ta)O_3 ceramics[147]. The aging behavior can be associated with a decrease of the remnant polarization caused by back-switching of domain walls, and domain wall clamping, domain wall vibration, and stress relaxation caused by 90° domain nucleation, all of which tend to decrease the internal stresses and reduce properties. In addition, diffusion of defects to the domain walls, or ordering of defects inside the grains, may lead to reduction of the properties.

5.4. Summary and conclusions

Ceramic samples of 7%KNLN were prepared according to conventional powder processing and air sintering, however very low values of properties were attained. Since remnant polarization was found to be very low, and back switching was observed, it was suggested that pinning of the domain walls by defects, compositional deficiencies or vacancies, would limit domain switching resulting in poor poling and therefore, cause low values.

In order to improve the properties, reduction of compositional deficiencies seems necessary. Sintering under oxygen flow has been suggested to limit oxygen vacancies and double-crucible-powder-packed sintering was shown to diminish evaporation of alkali elements. Therefore, both sintering methods were studied, giving

similar coupling and piezoelectric coefficients, being nearly 50% higher then obtained when samples were sintered in air, in the case of coupling coefficients.

Seemingly, sintering under oxidizing atmosphere and sintering under alkali rich vapor are two contradicting approaches. According to Shigemi and Wada[145, 146] the increase of formation energies of neutral potassium and sodium vacancies are inversely proportional to the increase of formation energy of oxygen vacancies.

Therefore, when sintering in oxygen rich atmosphere, oxygen vacancies were depressed, whereas potassium and sodium evaporations were encouraged. And in alkali rich vapor sintering, potassium and sodium evaporations were depressed, whereas oxygen vacancies were encouraged.

It has been shown[142] that by increasing the oxygen flow rates during sintering, properties were improved. Yet, very high oxygen flow rates caused a slight decrease in properties. No explanation was offered in the paper for this result. It is possible, that when the oxygen flow rate is such, giving the highest properties, the balance between potassium, sodium and oxygen vacancies is optimal. As soon as the oxygen flow rate is exceeded, this balance is disturbed and properties decline.

Considering the results obtained above, it is believed that similar balances between potassium, sodium and oxygen vacancies have been created in both sintering methods. By using lower or higher oxygen flow rate, this balance would be deviated and the properties would differ from the ones obtained by the alkali rich vapor method.

Appendix 5-1 - LA-ICPMS results for 7%KNLN

Niobium content was measured via SEM-EDX on ten random points on the surface of the sample and was averaged and used as an internal standard.

Point	LA diameter [µm]	Li [ppm]	Na [ppm]	K [ppm]	Nb [ppm]
1	30	3696	62789	110682	545670
2	30	3235	65482	112201	545670
3	30	2937	63761	109669	545670
4	30	3586	62522	109976	545670
5	30	2805	64770	107286	545670
6	30	3064	63820	110325	545670
7	30	2993	62225	110433	545670
8	30	2896	62054	109544	545670
9	30	3188	62915	109137	545670
10	30	2910	63041	111163	545670
11	30	2895	60237	108257	545670
12	30	2845	62937	107153	545670
13	60	3465	58285	109362	545670
14	60	3283	59925	109544	545670
15	60	2963	59472	107170	545670
16	60	3273	59621	110798	545670
Average	-	3127	62116	109544	545670
STDV	-	275	2049	1471	-

Using the atomic weights of the atoms, the concentration of the ions could be calculated to give:

$$K = 47.7\%$$

$$Na = 46\%$$

$$Li = 7.67\%$$

Adding the three A site cations concentrations, one would reach 101.37%, which could be cause by the deviation of 8.79% in different measured points of Li. Taking into consideration this deviation the concentration of Li would be $7.67\% * 0.879 = 6.74\%$, bringing the A site concentration sum to 100%.

Chapter 6 - Phase diagram of potassium sodium lithium niobate

A composition - temperature phase diagram of the system $(1-x)(K_{0.5}Na_{0.5})NbO_3$-$xLiNbO_3$ (xKNLN) is presented for $0 \leq x \leq 0.1$. Using dielectric and piezoelectric resonance measurements, and Raman spectroscopy, ceramic samples containing 2-10% $LiNbO_3$ were studied over a temperature range from -266°C to 550°C showing a complex sequence of phase transitions, which were identified using X-Ray diffraction. Analysis of the different Raman, piezoelectric and dielectric data shows distinct transitions from cubic to tetragonal to orthorhombic (with monoclinic features) to monoclinic (with orthorhombic features) phases for x=0.02-0.05. For x>0.07 only one transition between ferroelectric phases exists where tetragonal phase transforms to monoclinic phase. In the region between x=0.05 and x=0.08 the phase transition sequence is complex. Below -170°C monoclinic phase creates a vertical boundary with the monoclinic-orthorhombic phase near 5% Li. A triple point between the tetragonal, orthorhombic-monoclinic and monoclinic phase is identified around 0°C near 6-7%KNLN.

6.1. Introduction

Since the excellent electro-mechanical properties of PZT have been related to a morphotropic phase boundary (MPB) between rhombohedral (R), tetragonal (T) and monoclinic (M) phases[148], strong emphasis has been given on investigating lead free systems containing MPBs. One such system showing enhanced piezoelectric and dielectric properties is (1-x)(K,Na)NbO_3-x$LiNbO_3$ (xKNLN). It has been demonstrated that in this system those properties show a maximum[59, 60, 71, 149] at around x=0.06-0.07 $LiNbO_3$ at room temperature coinciding with a structural transformation from an orthorhombic (O) to a T phase[150]. This was believed to be the result of an MPB[59].

In KNLN and related systems, the transition between T and O phases shifts toward lower temperatures when the concentration of LiNbO3 is increased[151]. Such a temperature dependent boundary (polymorphic phase transition – PPT) has also been reported in relaxor-ferroelectric solid solutions, such as[15] $Pb(Mg_{1/3}Nb_{2/3})O_3$-$PbTiO_3$, $Pb(Zn_{1/3}Nb_{2/3})O_3$-$PbTiO_3$ and $Pb(Ni_{1/3}Nb_{2/3})$-$Pb(Zr,Ti)O_3$ [115]. In KNLN, maxima in the dielectric and piezoelectric responses are observed around room temperature coinciding with the thermally induced O-T phase transition temperature[151]. Thus, a question can be posed whether the enhanced room temperature properties in KNLN and related solid solutions are dominated by instabilities associated with the proximity of the phase transition temperature or, as most often claimed, are a consequence of a compositionally driven phase transition (an MPB). A thorough delineation of the phase transitions in KNLN is thus essential for a deeper insight into the nature of this problem.

In this chapter a tentative temperature-composition phase diagram of KNLN solid solution for $0 \leq x \leq 0.1$ is presented, based on X-Ray diffraction, Raman spectroscopy, dielectric permittivity and piezoelectric resonance measurements, of ceramic samples ($x \geq 0.02$).

6.2. Sample preparation

Ceramics of xKNLN with x=0.02, 0.03, 0.04, 0.05, 0.06, 0.07, 0.08, 0.09, 0.1 were prepared by solid state synthesis as described in chapter 5 (sintering in air). The sintered samples, with densities between 91-96% of the theoretical density, were polished to the final size keeping the aspect ratio of the samples (thickness/diameter) smaller then 0.1, suitable for dielectric and piezoelectric measurements. Gold-chromium electrodes were sputtered on both parallel surfaces for these electrical measurements.

6.3. X-Ray and neutron diffraction

X-Ray diffraction θ-2θ powder diffraction patterns of KNLN samples were taken on heating from -173°C to 550°C with temperature steps of 10° in order to determine the structural phase transitions. Due to time limitations, instead of recording a whole diffraction pattern for each temperature, only three selected 2θ regions (39.5-42.0°, 58.0-60.5° and 74.0-75.4°) were scanned. By recording a *(h00)*, *(hh0)* and *(hhh)* cubic-like diffraction peaks, by detecting splitting it is possible to have access to the unit cell symmetry and to determine the lattice parameters. For example, in a cubic-rhombohedral (C-R) phase transition, the single *(hhh)* Bragg reflection splits to two peaks in the R phase, whereas the single *(h00)* peak remains single. In order to have the best compromise between time consumption, accuracy (usually at higher 2θ angle) and high enough intensity/background ratio (usually at lower 2θ angle), the C-like peaks (200), (220) and (222) were selected. The (300) peak is also reachable but in the C phase its position is confounded with that of (221) peak.

Figure 6-1a illustrates spectra taken for 2%KNLN sample at various temperaturs, up to 22°C. Even though the spectra were taken within 200°C range, only one phase is detected. It is surprising that the (200) peak region never shows any single peak as one may expect in an R phase, phase believed to be the stable low temperature phase in KNN. However the low temperature phase is clearly not R in KNN with a low amount of Li. Rather, the Miller indices were matched to an O phase (see chapter 3.6) with (002) and (200) peaks at the 39.5-42.0° interval, (040), (004)

and (222) peaks at the 58.0-60.5° interval and (042) and (402) peaks at the 74.0-75.4° interval.

Extensive early studies[2, 43, 152, 153] established that $K_yNa_{1-y}NbO_3$ adopts the series of phases cubic-tetragonal-orthorhombic (C-T-O) above 0°C that are common to many perovskite ferroelectrics, including $KNbO_3$ (KN). Analogy to KN at low temperatures may mistakenly point to R phase but recent study[44] on $K_yNa_{1-y}NbO_3$ ceramics with y=0.4-0.6 claims R phase could be found only in potassium rich compositions. An M phase was identified in all compositions, co-existing at times with the R phase. Similar results were reported for KNN ceramics with y=0.5 and particle size bigger then 200nm[45]. It was also reported, using both x-ray and neutron diffraction, the existence of a *Pm* M phase at room temperature between y=0.24 and y=0.36, existing within a large concentration of K/Na[46]. Interestingly, it was also shown that a M-T first-order phase transition takes place without going through any O phase.

Unit cell parameters of the O phase are commonly given in the axes system, where $x_1:[110]_c, x_2:[-110]_c, x_3:[001]_c$. Since O phase is a special case of the M phase with the unit cell angle β=90°, the lattice parameters presented at Figure 6-1b were calculated for an M phase revealing a=b≠c, β ≈86°. This conversion enabled easier representation of the lattice parameters.

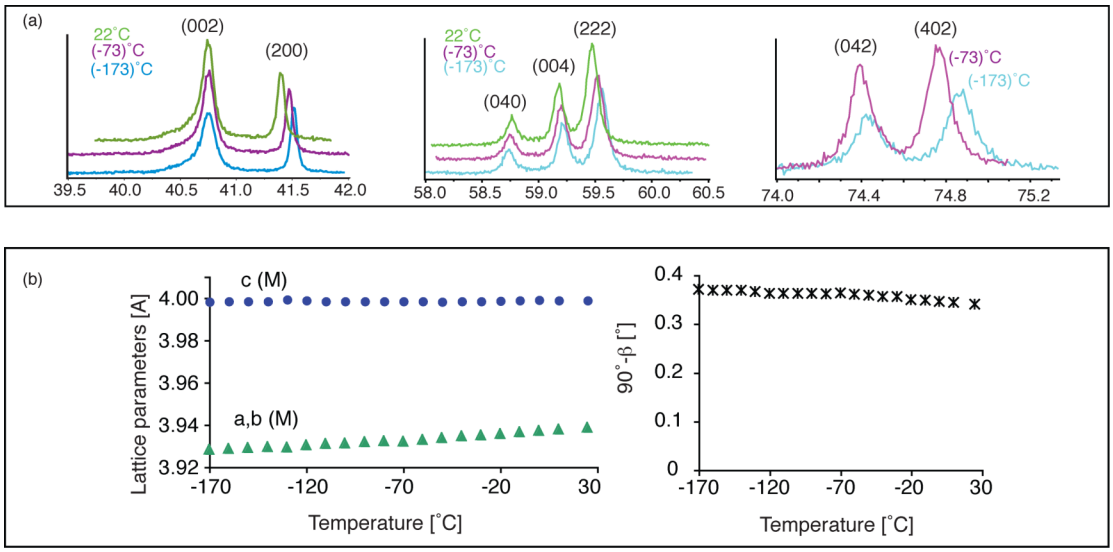

Figure 6-1 -XRD data at different temperatures for 2%KNLN presenting (a) spectra at three characteristic intervals and (b) calculated lattice parameters and lattice angle

The low temperature phase could be described by an O phase but a subtle change at 2θ~40.7° occurs as a function of temperature. As can be noted in Figure 6-1a, the left Bragg peak (at 2θ~40.7°) becomes broader with a clear asymmetry, as the temperature decreases, whereas the right peak (at 2θ~41.5°) remains symmetric and narrow in the whole temperature range.

For a better understanding of the low temperature phases, complete neutron diffraction pattern was recorded at -200°C, using the Orphée reactor at Laboratoire Léon Brillouin (Saclay, France). Since neutron diffraction is sensitive to light atoms, it should be possible to detect oxygen octahedra tilting. However, no evidence to superstructure peaks were noted, hence the subtle change between the low and high temperature phases could not be attributed to oxygen octahedral tilting.

In order to reveal the structure, the neutron diffraction pattern was refined by Rietveld analysis. Two different symmetries were tested, O and M, showing a better refinement with an M *Pm* phase: a=3.9911(2)Å, b=3.9349(2)Å, c=4.0014(2)Å, β=90.380(1). However, as can be deduced from the angle, the M distortion is very small.

As Li concentration increases, the diffraction patterns at low temperature slightly change. Figure 6-1a demonstrates diffractograms of 4%KNLN (XRD spectra and unit cell parameters of other samples are presented in Appendix 6-1 and Appendix 6-2). Note that the first left peak at 2θ~39.9 is a parasitic peak associated to the silver (paste to glue the sample) and/or the copper (sample holder) and should not be considered in the analysis.

Low temperature diffractions displays similar features as discussed for 2%KNLN. Indeed, the Bragg peak at 2θ~40.7° is even broader than the corresponding 2%KNLN peak, indicating that the M distortion is bigger. A clear first order phase transition occurs at 97°C as both the O-like and T phases coexist. The T to C phase transition taking place close to 440°C is also of first order.

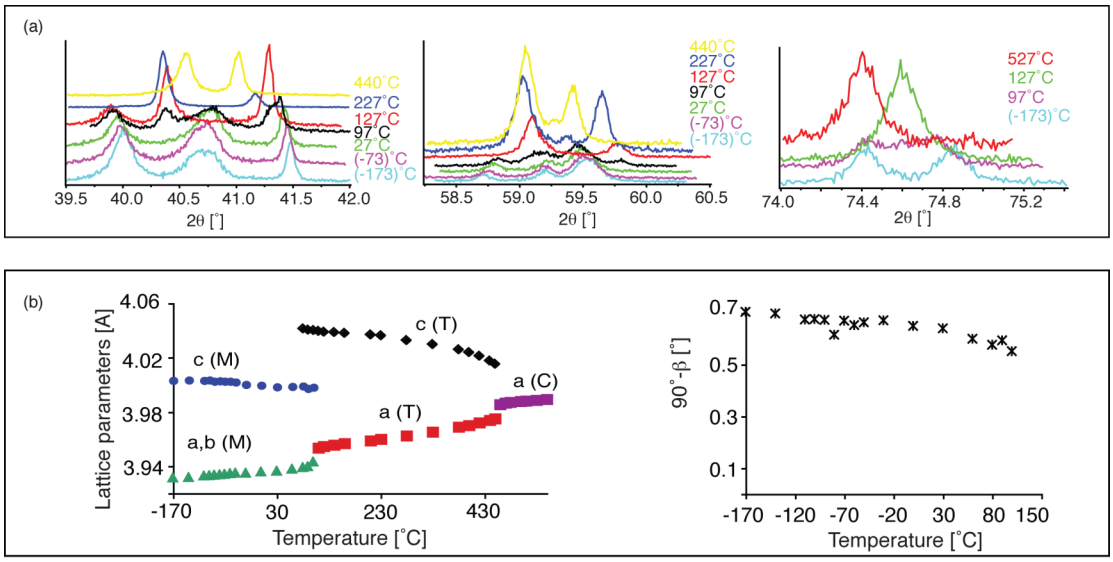

Figure 6-2 -XRD data at different temperatures for 4%KNLN presenting (a) spectra at three characteristic intervals and (b) calculated lattice parameters and lattice angle

The existence of only one phase below room temperature for KNLN samples contradicts the analogy to KNN phase transitions, where one would expect a second phase transition around (-90)°C. This second transition could be detected in KNLN by Raman spectroscopy, dielectric and piezoelectric measurements, as will be presented later in this chapter. The lattice angle becomes closer to 90° as temperature increases (seen in Figure 6-1,Figure 6-2 and Appendix 6-2), and hence becomes "more" O. Therefore, a probable explanation could be that the two phases, O and M, are present together, having a more O behavior at higher temperatures (O/M) and more M behavior at lower temperatures (M/O).

By increasing Li concentration, the splitting of the left peak in the (200) region into two peaks becomes clear at 5%Li (Appendix 6-1 and Appendix 6-2). The *Pm* phase at low temperature is now clear as its distortion is now high enough to be observed. The change from a broad peak to a split peak is evident between x=0.04 and x=0.05, as can be observed in Figure 6-3, summarizing the lattice parameters and unit cell volume of different concentrations at one constant temperature, T=(-170)°C. This change indicates a phase transition from a M/O phase to a pure M phase at higher Li concentrations.

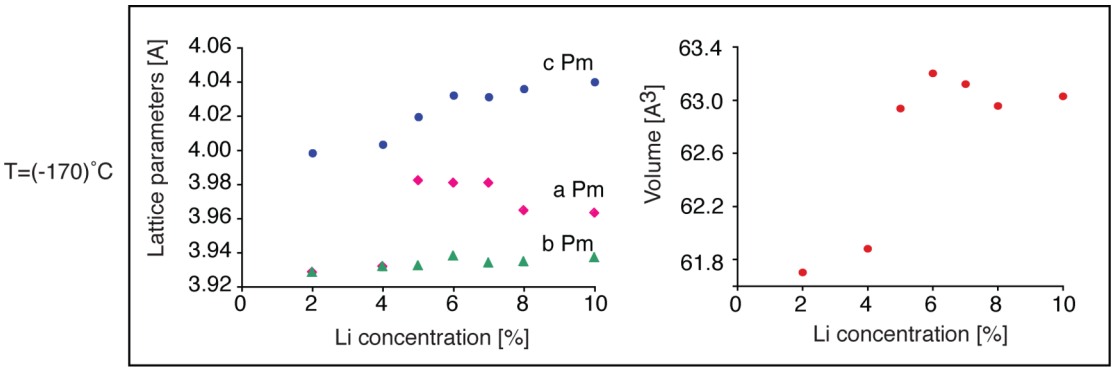

Figure 6-3 -lattice parameters and unit cell volume as a function of Li concentration at (-170)°C

6.4. Raman spectroscopy

In the analysis of spectra taken on all KNLN samples upon heating from –266°C to 550°C, no attempts were made to identify the normal modes responsible for the features ascribed to different phases, but rather qualitative differences were monitored.

In many cases the spectra across a phase boundary were clearly and qualitatively different at a level that could be noted as the data were collected. However, across some transitions the changes were more subtle, and for those it was necessary to characterize the changes with more sensitivity. For that purpose the spectra were first normalized to their integrated intensities to eliminate effects associated with the inevitable ~10% variation introduced by re-focusing, and those normalized spectra were fitted with an appropriate number of Lorentzian lines. Signatures of phase changes were sought in the temperature and composition dependence of the line frequencies, widths and strengths.

6.4.1. Raman spectroscopy – qualitative inspection

Very distinct spectral changes across the T to C phase transition boundary are apparent, as discussed for 2%KNLN and shown in Figure 6-4a. Just below the transition, the T phase has strong broad lines at 250 and 600 cm^{-1} and a weaker line at 850 cm^{-1}. The two strong lines broaden and weaken above the Curie temperature (T_C) at 440°C, and the weak line disappears completely. These changes were found to be universal in the KNLN system, including in Li-free single crystals[48] and $KNbO_3$

ceramics[154], making this transition especially easy to trace by Raman spectroscopy. The C perovskite phase, with all ions at centers of inversion, supports no Raman active modes at all. Subsequently, the presence of any Raman signal above T_C establishes that the phase has significant local departures from a C perovskite structure[155].

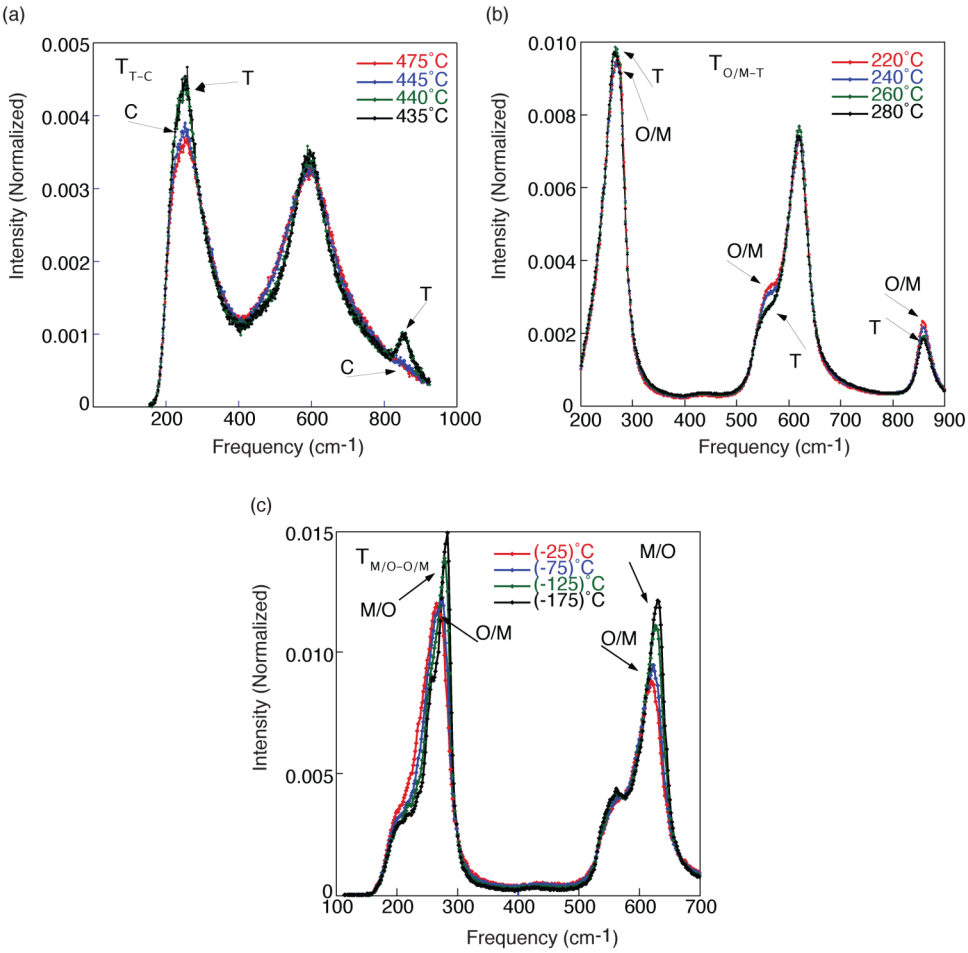

Figure 6-4 -Raman spectra of 2%KNLN going through a sequence of phase transitions (a) T-C, (b) O/M-T and (c) M/O-O/M

The next transition below the Curie temperature of 2%KNLN is depicted in Figure 6-4b. It should be noted that the Raman signature of the T phase differs between Figure 6-4a and b, as should be expected in view of the factor of two difference in the temperatures at which they were taken. At 240°C the T phase Raman spectrum shows lines that have narrowed substantially from 440°C, now showing multiple phonon contributions to the two main features found at 250 and 600 cm^{-1} in the 440°C spectrum. In addition to the narrowing, all of the phonons harden, i.e.,

increase in frequencies, as the temperature is lowered, as is expected for thermal contraction. Following the evolution of the Raman spectra with temperature across the entire T phase, established the absence of any discontinuous changes that would signal a further phase transition.

In the O/M phase there are distinct shoulders in the Raman spectra on the low-frequency sides of the main Raman modes, shoulders that are present also in the T phase although rather weaker. Furthermore the O/M phase sees a loss in Raman intensity in the 400-500 cm^{-1} region. As can be seen in Figure 6-4b and c, that the M/O-O/M transition has similar characteristics to the O/M-T transition. The same lines exist but they show a discontinuous change in relative intensity across the M/O-O/M phase transition. Thus extracting these transition temperatures requires a more careful fitting of the Raman spectra.

Samples with x<0.05 show the same features as 2%KNLN. In compositions with x above 0.07-0.10 only one phase transition between ferroelectric phases (M-T) is observed (for spectra of all samples see Appendix 6-3).

6.4.2. Fittings of Raman spectroscopy data

The Raman spectra were fitted using a sum of Lorenzian lines, as illustrated in Figure 6-5 for 3%KNLN, as an example.

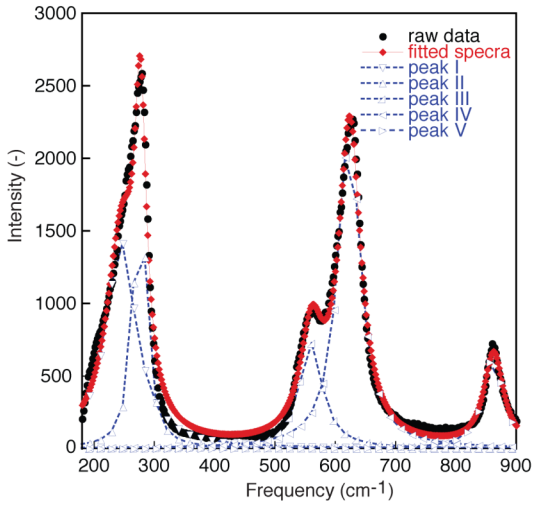

Figure 6-5 -Fitted Raman spectra of 3%KNLN, where the circles are the raw experimental data, the triangles are Lorentzian fits of individual peaks and the diamond shapes are the total spectrum calculated from fitted data. The lines are guides for the eye.

The fitted line corresponds well to the raw data with R^2>99%. Information on width, intensity and frequency position of the peaks was extracted from the fitted curves and plotted as a function of temperature. In Figure 6-6 the data presented for 3%KNLN indicates phase transitions from M/O to O/M (Figure 6-6a), O/M to T (Figure 6-6b) and T to C (Figure 6-6c).

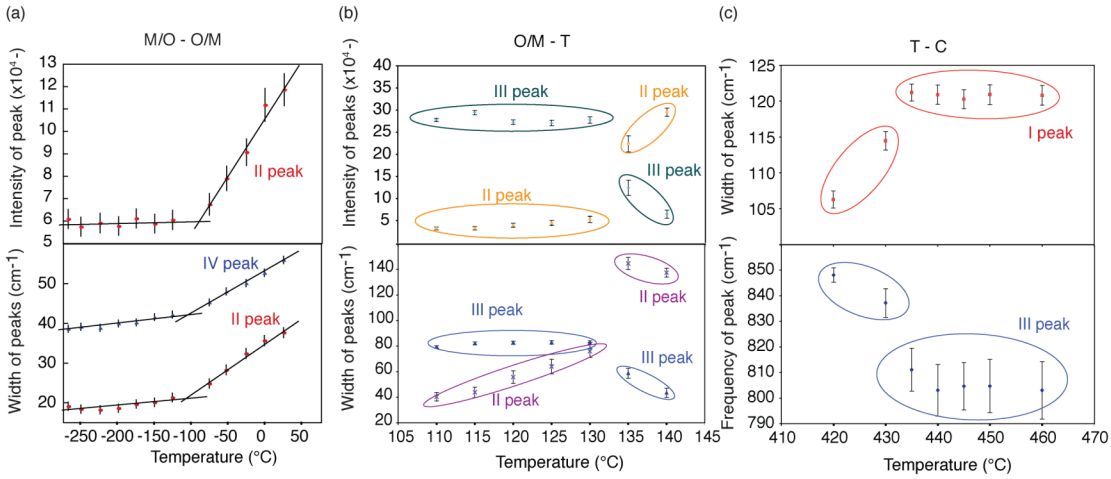

Figure 6-6 -Width, intensity and position of fitted Raman peaks (presented in Figure 6-5) as a function of temperature for 3%KNLN indicating phase transitions: (a) M/O-O/M (b) O/M-T and (c) T-C. Vertical lines denote error bars

The low temperature transition (M/O-O/M) in the case of 2-5%KNLN is characterized by a change in the slope of the temperature dependence of the phonon characteristics (Figure 6-6a and Appendix 6-4 for 4 and 5%KNLN). The phase transition temperature was determined as the temperature at which the two lines from the different slopes intersect.

The gradual change of the phonon properties and the absence of perceptible thermal hysteresis between M/O and O/M phases is consistent with the absence of a clear transition in the XRD spectra of KNLN samples. Considering the discontinuous character of this transition in KN and KNN crystals[41, 48], and the XRD results published lately[44] the space group of Li-modified compositions seems not to be the same as for KN and KNN; this can happen if, for example, addition of Li induces tilt of oxygen octahedra.[153, 156-159]

The two high temperature transitions (O/M-T and T-C, in Figure 6-6b and c respectively), present a clear abrupt change in the fitted parameters, consistent with the features of a first order phase transition. Similar abrupt change is noted for 7%KNLN (Figure 6-7) and higher lithium concentration (Appendix 6-4) for the low transition temperature near -30°C, indicating a first order transition between M and T phases.

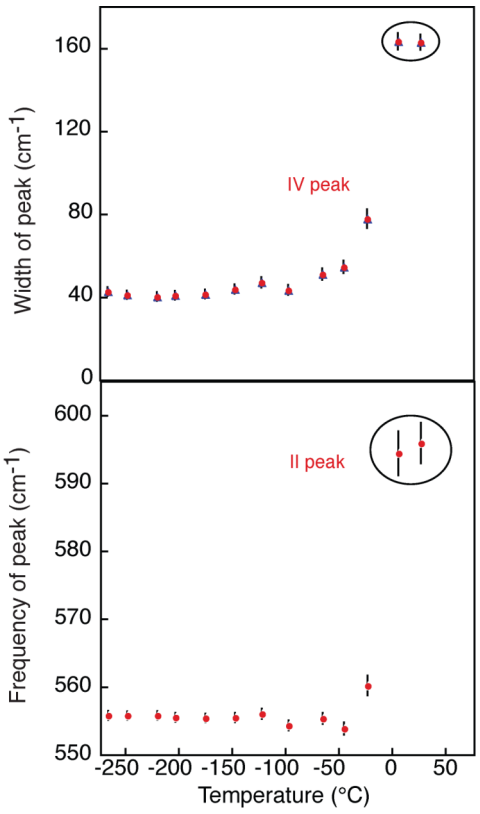

Figure 6-7 -Width and position of fitted Raman peaks as a function of temperature for 7%KNLN. Vertical lines denote error bars.

6.4.3. Isothermal or composition-dependent lines

Normalized Raman spectra from all concentrations at constant temperature were analyzed. Examples of spectra are shown in Figure 6-8 for -266°C, 27°C, 200°C and 400°C. Figure 6-8a represents spectra in temperatures below -170°C. It reveals an abrupt change of pattern between 5 and 6%KNLN, with a line at 280 cm^{-1} identifying the M/O phase at lower Li concentrations, developing satellites in the region between 200-280 cm^{-1} and indicating the appearance of a pure M phase. This phase transition between the M/O and M phase is vertical (temperature independent). Above -170°C

the temperature of this phase transition gradually shifts until at 0°C it passes between 6 and 7%KNLN (Figure 6-8b). Above room temperature there is no sign for a phase transition of this type (Figure 6-8c and d).

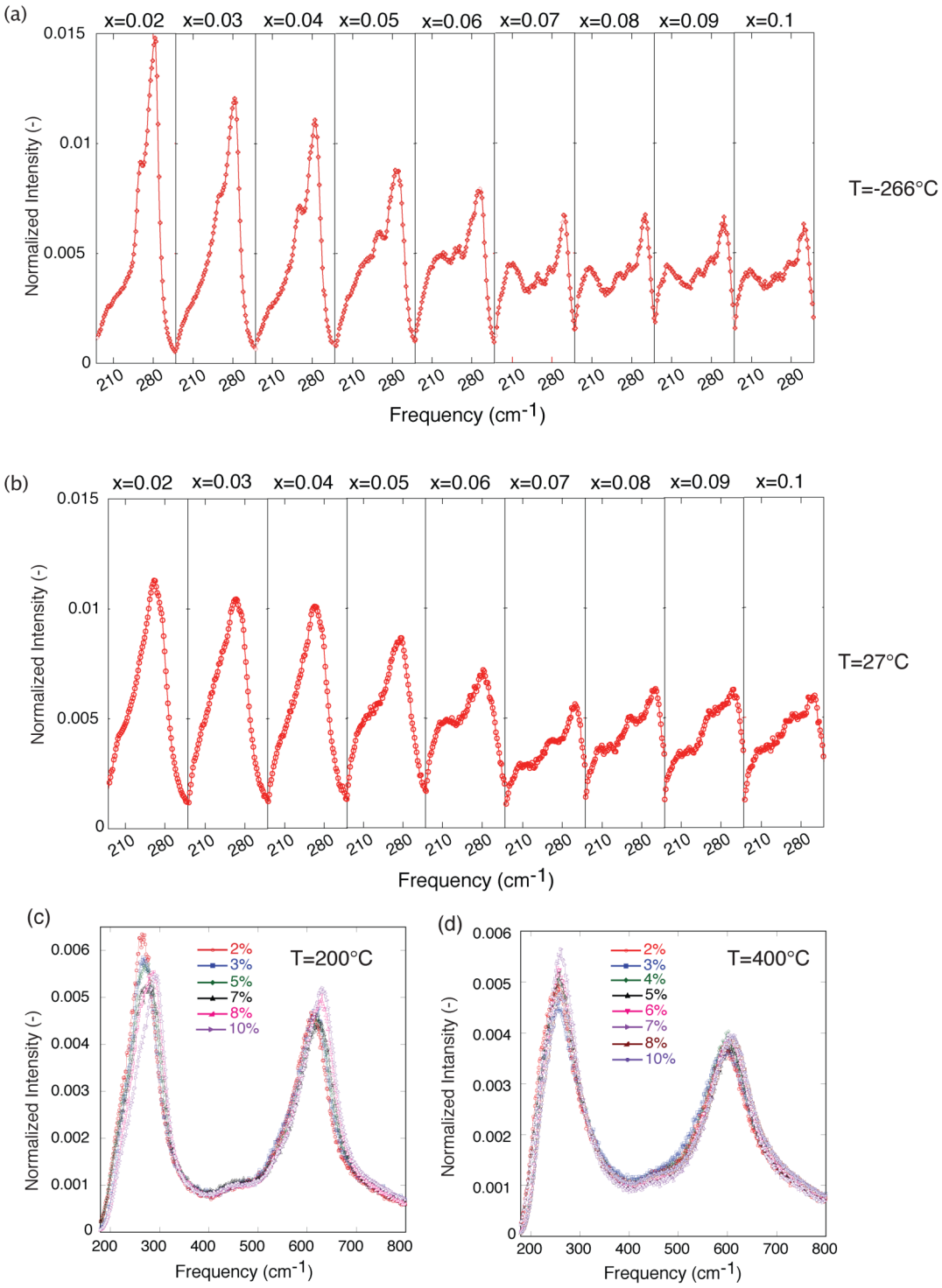

Figure 6-8 -Normalized Raman spectra of different compositions showing a phase transition around (a) 5%KNLN at -266°C, (b) 7%KNLN at 27°C, and no transitions at (c) 200°C and (d) 400°C

6.5. Dielectric measurements

The relative permittivity of the unpoled samples at constant stress, ε_r, and loss tangent, δ, were determined from capacitance measurements (see chapter 3.3). Measurements were made at a frequency of 100 kHz, upon heating the samples from 30°C to 500°C at 2°C/min. Since dielectric anomalies associated with ferroelectric-ferroelectric phase transitions appearing at lower temperatures are broad, the temperatures of those transitions were sometimes difficult to determine. The accuracy may be improved by measuring permittivity and loss of poled samples, or by taking temperature derivatives of permittivity and loss data[115]. Therefore the samples were poled at 50°C and under 50kV/cm for different times ranging from 5 to 30 minutes optimized for the different compositions[141]. After aging for at least 24 hours, the relative permittivity was measured again upon heating from -240°C to 200°C using the same parameters. The accuracy in the determination of the phase transition temperatures is estimated to be about 4°C.

Figure 6-9a shows the dielectric peaks for all samples in the temperature range from -150°C to 550°C. The temperature dependence of the relative permittivity shows two clear peaks that were associated with phase transitions, and are presented in the enlarged graphs (Figure 6-9b and c). The peak present at the higher temperature (Figure 6-9b) corresponds to the T-C phase transition. Its temperature increases gradually from about 420°C at 2%KNLN to 520°C at 10%KNLN. The temperature of the second peak (Figure 6-9c), seen at 180°C for 3%KNLN, shifts to lower temperatures with increasing x; it becomes wider and less well defined as Li concentration increases.

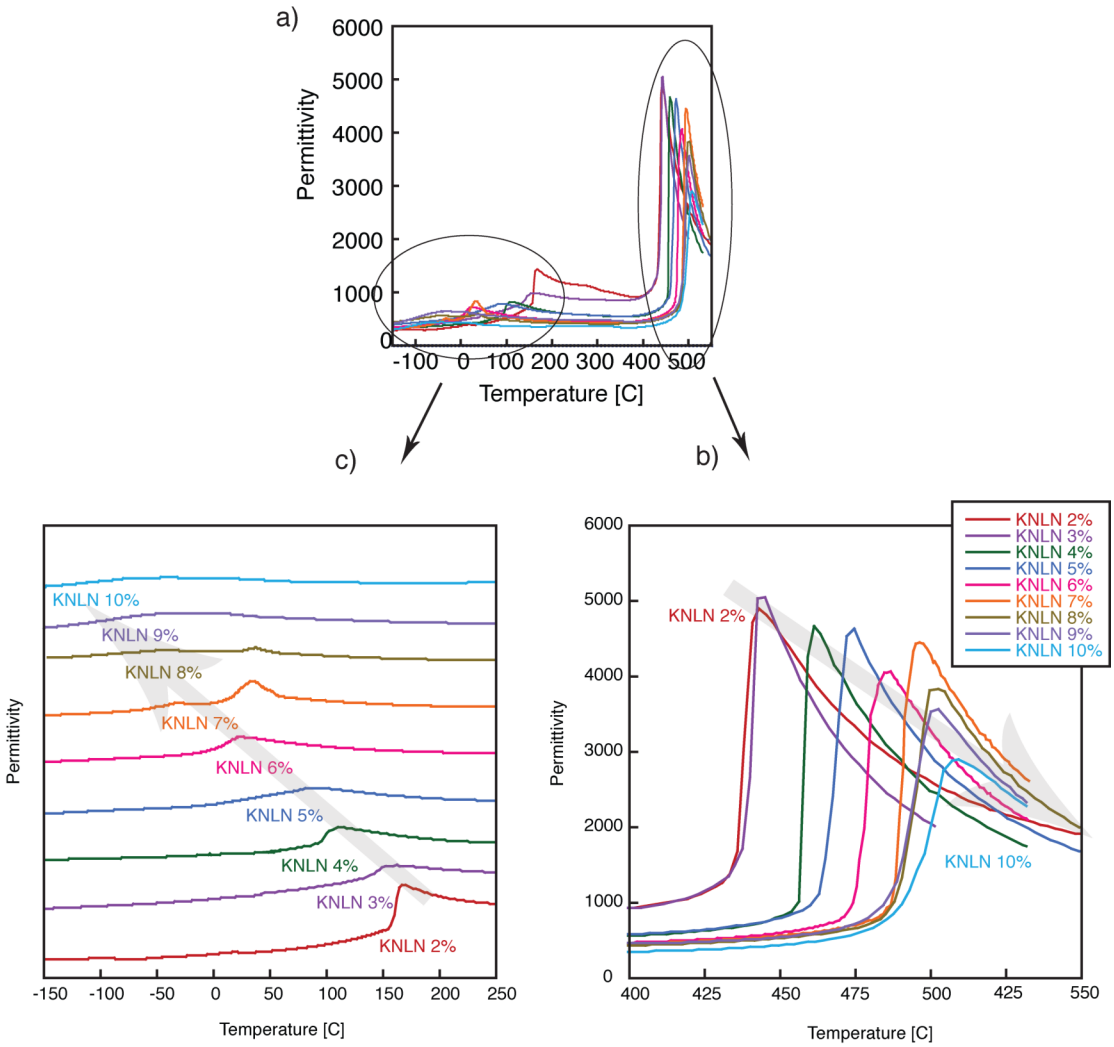

Figure 6-9 -Temperature dependence of the relative permittivity measured at 100 kHz of 2-10%KNLN from (a) -150-550°C and the enlarged regions where (b) T-C and (c) O/M-T phase transition occurs.

A third peak is observed at low temperatures in some compositions with $x \leq 0.07$. This peak is less pronounced than the two peaks appearing at higher temperatures, but can be seen in the temperature derivative of the permittivity (illustrated for 3%KNLN in Figure 6-10). Raman and/or piezoelectric data discussed in this chapter confirm that this third dielectric peak is indeed related to a phase transition.

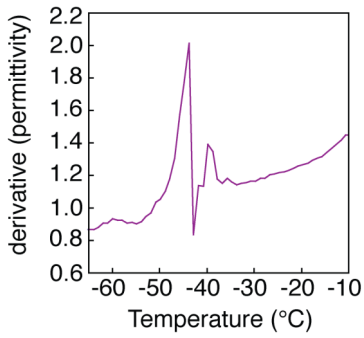

Figure 6-10 -Low temperature phase transition observed by the derivative of the permittivity for 3%KNLN

6.6. Piezoelectric measurements

Poled samples were used to determine phase transition temperatures by observing anomalies in the elastic properties via the piezoelectric resonance technique[2]. Elastic anomalies are sometimes more distinct and less ambiguous than dielectric anomalies, which can be caused by charge relaxation processes as well as by structural phase transitions. Furthermore elastic properties in ferroelectrics may be sensitive to structural modifications that do not leave a clear signature in the dielectric behavior. Such is the case for the transition between the low- and high-temperature R phases in Zr rich PZT[160] and for ferroelectric-paraelectric phase transition[161] in $Gd_2(MoO_4)_3$.

For the radial mode, the resonant frequency under a short circuit condition is related to elastic properties as has been presented in chapter 3.4.1 (Equation 3.3). For the present purposes it was not necessary to calculate explicitly the elastic coefficients since the temperature dependence of the resonant frequencies is sufficient to determine the phase transition temperatures. Resonant (minimum of impedance) and anti-resonant (maximum of impedance) frequencies of the fundamental radial vibrations were determined upon heating in the temperature range from about -170°C to 150°C. The samples were stabilized at each temperature for at least 5 minutes. The accuracy in the determination of the phase transition temperatures is estimated to be about 10°C, equal to temperature intervals between measurements.

Resonant and anti-resonant frequencies were measured for 2,3,5,6 and 10%KNLN as a function of temperature, and are plotted in Figure 6-11. These plots enable identification of the phase transitions via two main characteristics. The

transitions in 2%KNLN (Figure 6-11a) are indicated by a nearly discontinuous jump of characteristic frequencies of about 0.5MHz at ~150°C. A more gradual increase of about 0.3 MHz at ~(-60)°C is noted both in 2 and 3%KNLN (Figure 6-11b). The high transition in 3%KNLN is denoted by a large change of the slopes of the resonant frequency vs. temperature curve, at ~150°C. Similar changes of the slopes indicate transitions at 5%KNLN (Figure 6-11c), and 10%KNLN (Figure 6-11e) at 50°C and (-80)°C respectively, and two transitions in 6%KNLN (Figure 6-11d) at ~20°C and ~(-60)°C. The low temperature transition in the cases of 2 and 3%KNLN occurs over a temperature range of about 30°C. In addition to phase transitions, a softening of the structure is indicated in Figure 6-11d by a slow decrease in the resonant frequencies above 80°C.

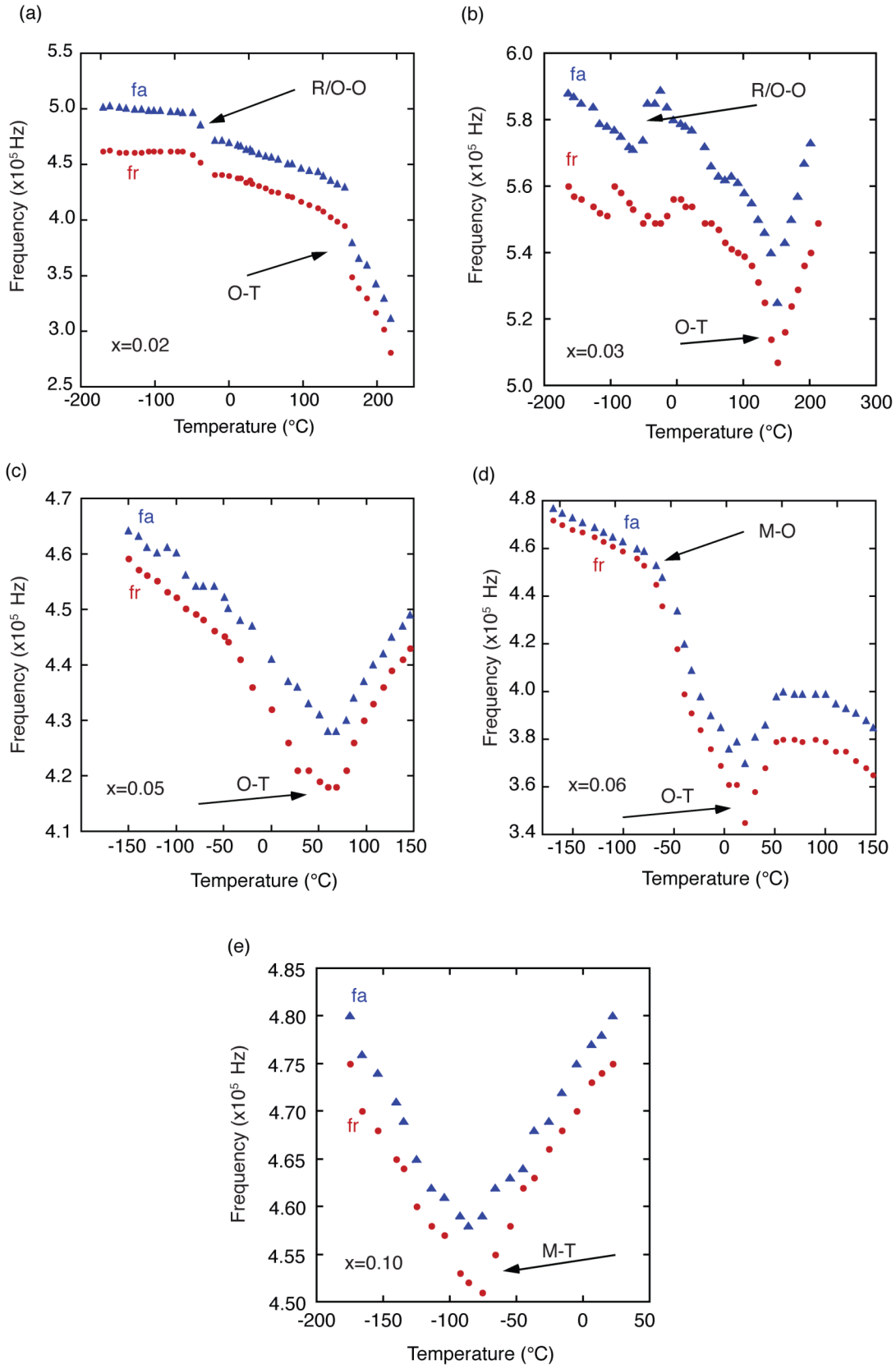

Figure 6-11 -Temperature dependence of the radial mode resonant and anti resonant frequencies for (a) 2%KNLN and (b) 3%KNLN, (c) 5%KNLN, (d) 6%KNLN and (e) 10%KNLN. The arrows indicate positions of phase transitions.

6.7. The phase diagram

Transition temperatures detected by Raman spectroscopy, dielectric and piezoelectric measurements, described in this chapter (sections 6.4-6.6), show excellent agreement. Figure 6-12 presents the derived KNLN phase diagram with crystal systems resolved using X-Ray diffraction (section 6.3).

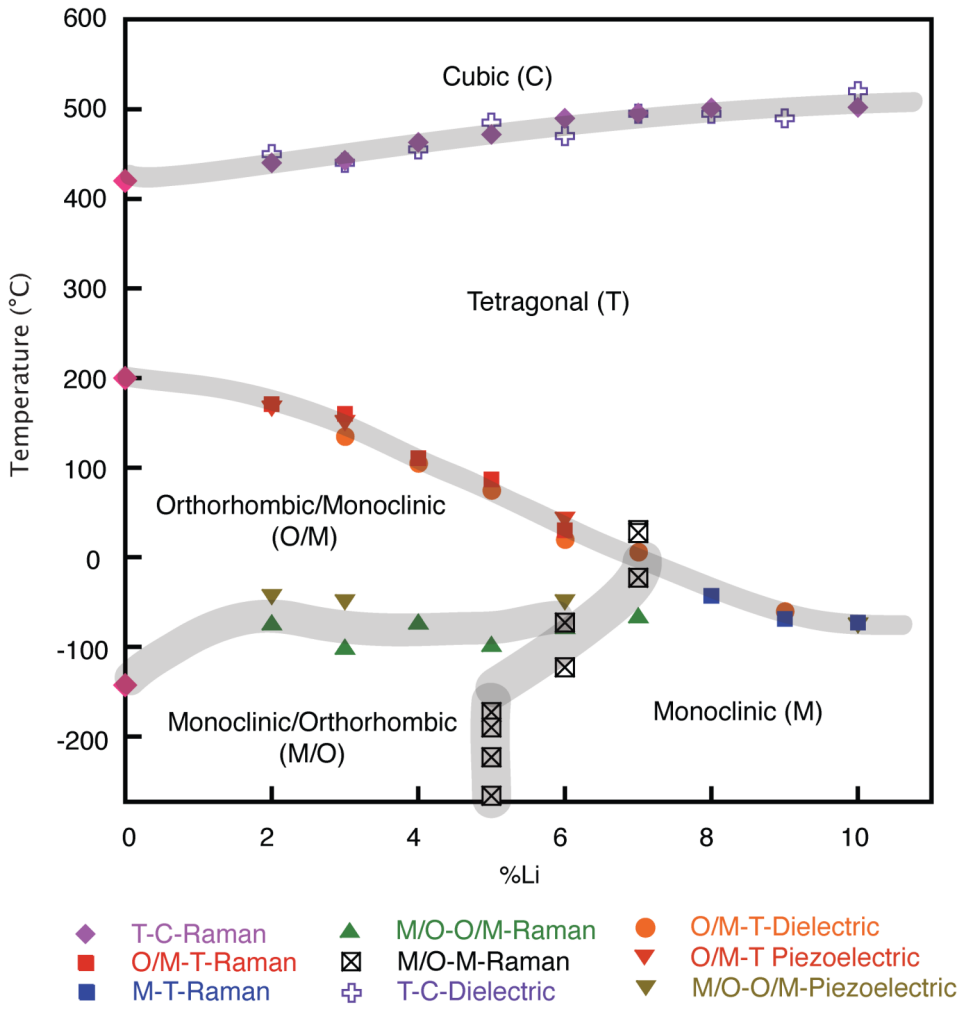

Figure 6-12 -Temperature-composition phase diagram of $(1-x)(K_{50}Na_{50})NbO_3$-$xLiNbO_3$ solid solution for $0 \leq x \leq 0.1$, based on dielectric permittivity, piezoelectric resonance and Raman spectroscopy measurements.

As can be seen in Figure 6-12a vertical MPB appears at approximately 5%KNLN, at temperatures below -170°C, separating M/O phase and a pure M phase. At higher temperatures and up to 0°C this boundary bends toward 7%KNLN. Although both phases are mostly monoclinic, their polarization orientation is different

(due to the O nature of the low Li concentration phase), therefore, the nature of this MPB could be similar to relaxor-ferroelectric crystals in PZT[13], where the huge enhancement of the piezoelectric properties along nonpolar directions is related to the polarization rotation mechanism[162]. It should be mentioned that the polarization orientation of M in the low temperature phases in KNLN were not specified as opposed to PZT materials having M with [100] or [110] polarization orientations.

The vertical MPB in KNLN appears at temperatures that are too low to be of wide-range practical interest and where the magnitude of the materials coefficients would be in any case low. However, its presence is important from the fundamental point of view: it would signal the possibility that this lead-free system supports such MPBs, which may be brought to a more useful temperature range by modifying crystal composition.

The phase diagram exhibits a region at ~7-8%KNLN and ~223K to 273K where three phases (M, O/M and T) meet. Such a region, in which two or more phases have a nearly degenerate energy is associated with a flat free energy profile, possibly leading to enhanced piezoelectric and dielectric properties[16, 19, 163]. Like the vertical MPB, such a region could hopefully be brought to a more useful temperature range by crystal chemistry engineering.

6.8. Summary

A tentative phase diagram of the system KNLN has been composed based on dielectric and piezoelectric measurements, and Raman spectroscopy, with the phases resolved by X-Ray diffraction. Our results suggest the presence of a vertical MPB at low temperatures at approximately 5%KNLN. This boundary separates a monoclinic-orthorhombic phase, different from the one observed in $(K_{0.5}Na_{0.5})NbO_3$ (a monoclinic-rhombohedral phase), and a pure monoclinic phase. The results also identify a triple point where tetragonal, monoclinic and the monoclinic-orthorhombic phases meet. Both the vertical MPB and the triple point are regions where enhanced piezoelectric and dielectric properties can be expected due to a flattening of the free energy profile. Future work should be carried out to investigate if the temperatures of these regions could be increased by chemical engineering into practically used temperature ranges.

Appendix 6-1 - XRD spectra of KNLN samples with x=0.05-0.08, 0.10

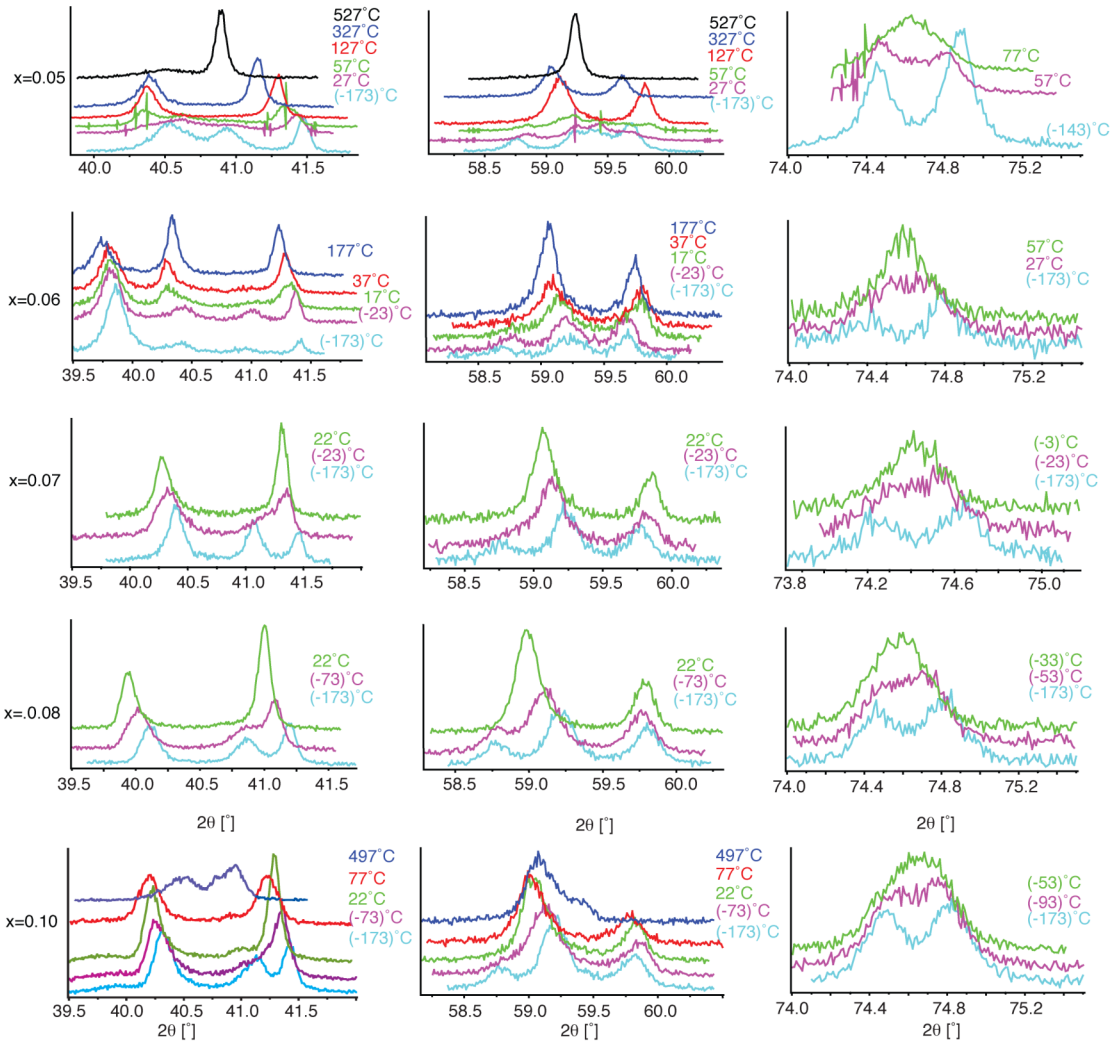

Appendix 6-2 - Lattice parameters and lattice angles for KNLN with x=0.05-0.08, 0.10

X=0.05

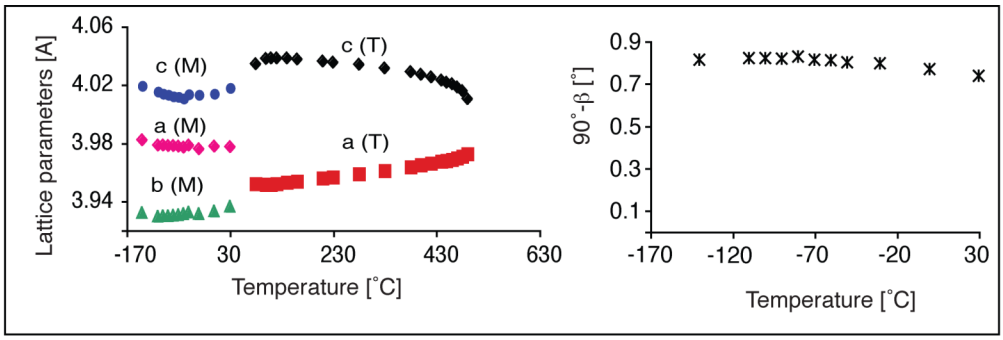

X=0.06

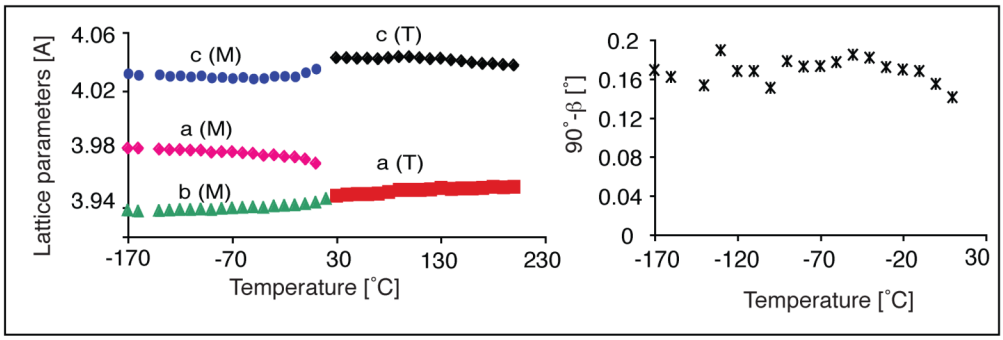

X=0.07

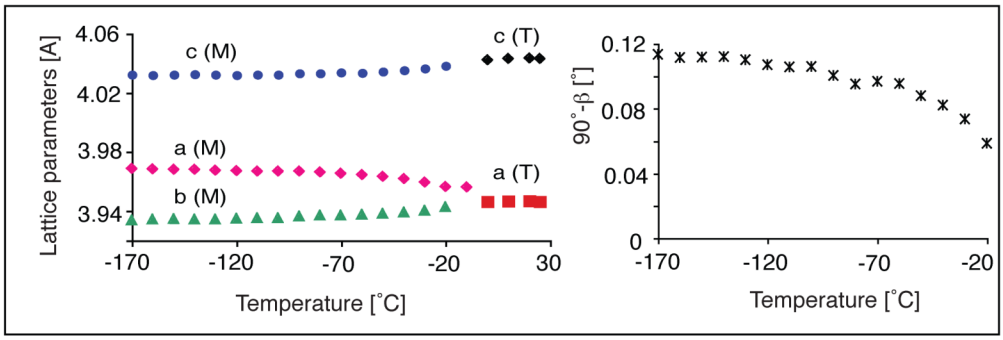

X=0.08

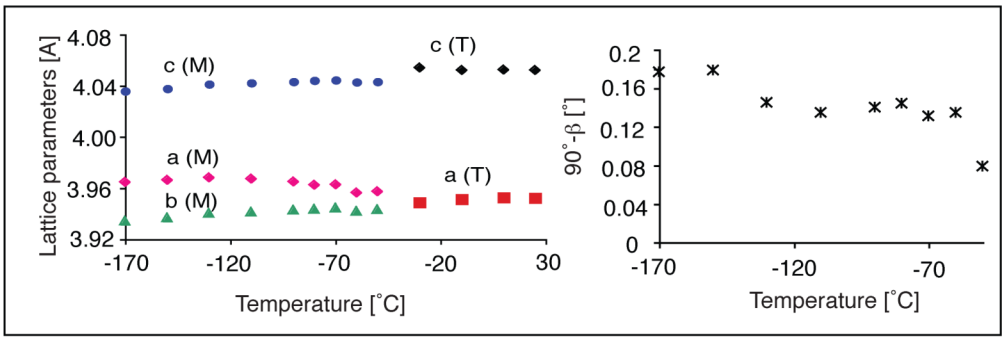

X=0.10

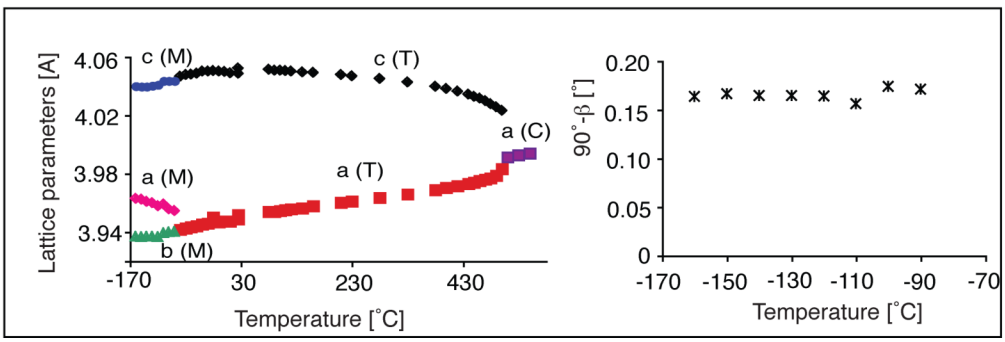

Appendix 6-3 - Raman spectra of KNLN samples with x=0.03-0.10

x=0.03

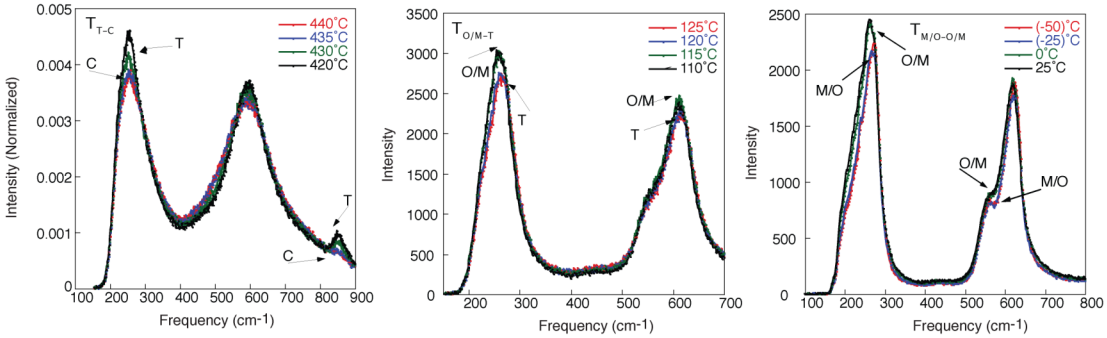

x=0.04

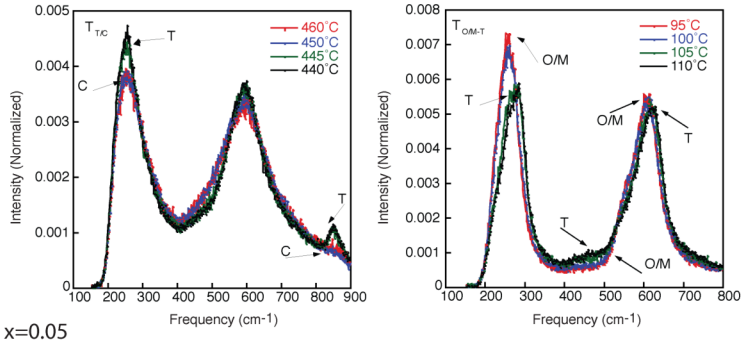

x=0.05

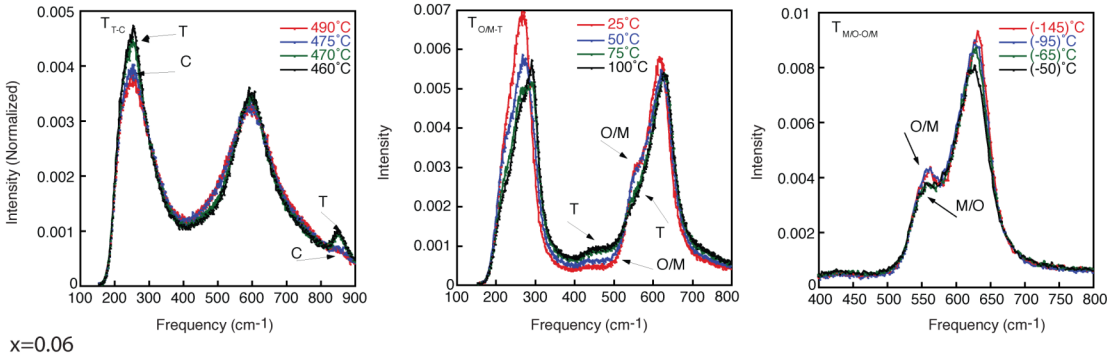

x=0.06

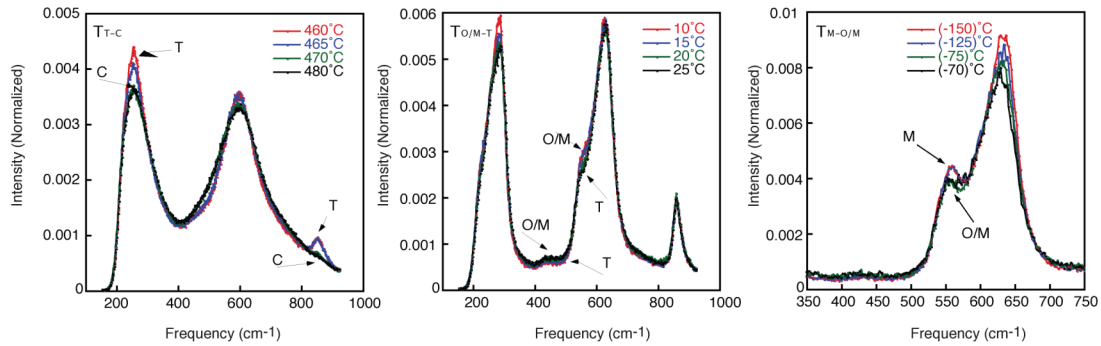

x=0.07

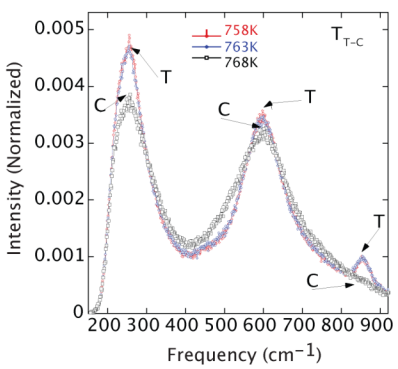

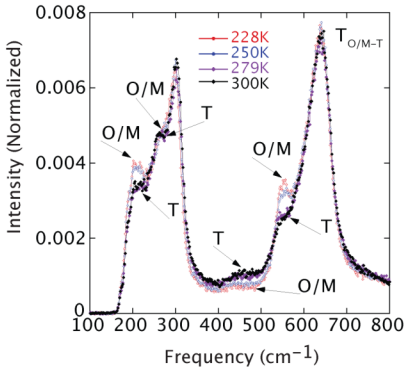

x=0.08

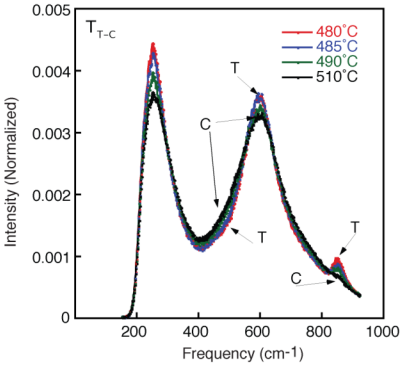

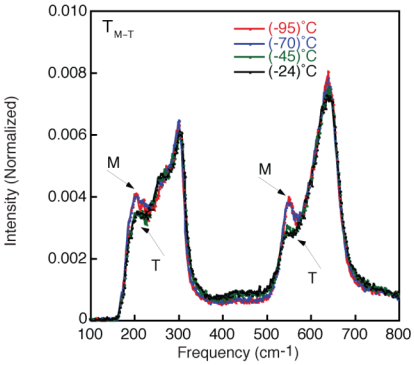

x=0.09

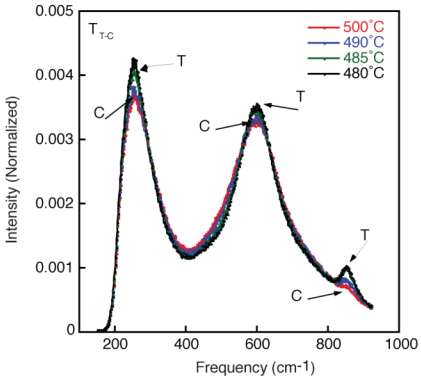

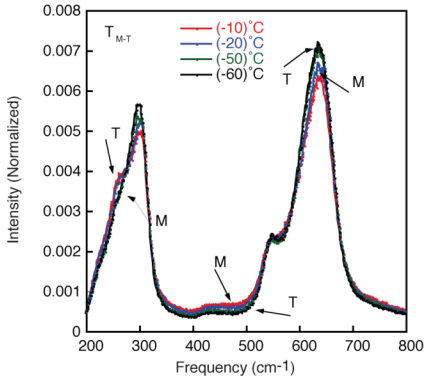

x=0.10

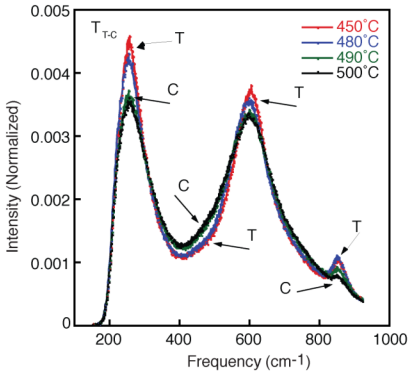

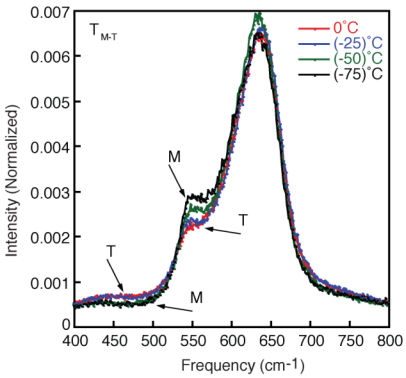

Appendix 6-4 - Fitted Raman spectra for KNLN samples with x=0.04, 0.05, 0.08 and 0.09

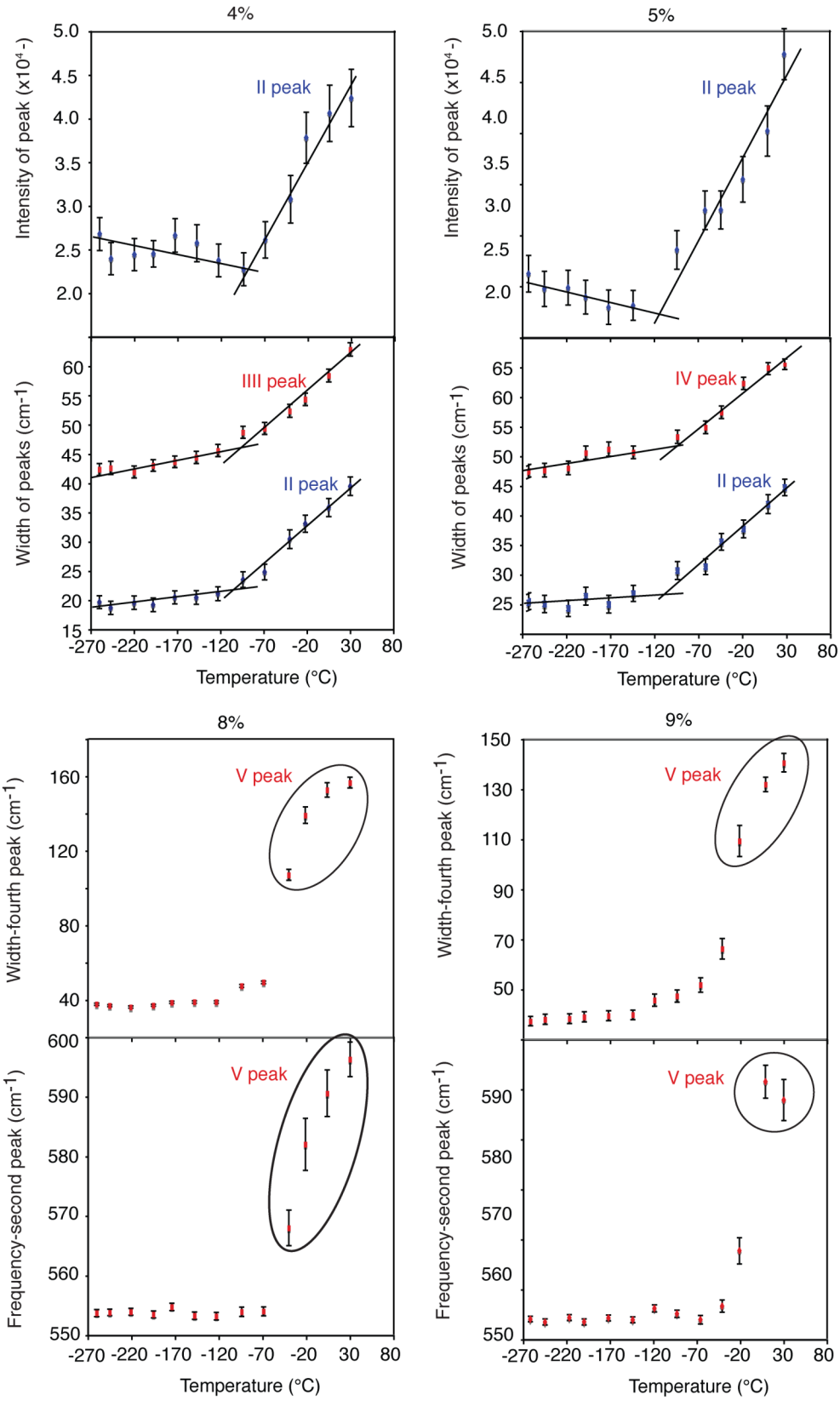

Chapter 7 – KN and KNLN single crystals for high frequency applications

Following predicted and measured large thickness coupling coefficients in monodomain $KNbO_3$ rotated away from the Z axis by θ=40.5° about the orthorhombic Y axis, and due to the high preparation coasts involved, a slightly different cutting angle (θ=45°, $[001]_C$-cut) was investigated. Calculations predict high values should be expected for monodomain and domain-engineered single crystals cut at this angle.

In this chapter, large thickness coupling coefficients of $k_t \leq 70\%$ were measured in both monodomain and domain-engineered crystals $[001]_C$-cut. k_t was found to be extremely stable over a large temperature range, remaining high ($\geq$65%) even upon heating and cooling through the orthorhombic-tetragonal phase transition. This is likely related to another finding that spontaneously high k_t values ($\leq$68%) are observed in as-grown unpoled, $[001]_C$-cut, polydomain $KNbO_3$ crystals. k_t stayed also stable upon thinning to thicknesses below 60μm, as required for high-frequency applications.

However, $KNbO_3$ crystals (monodomain and domain-engineered) show low permittivities, which present a challenge for impedance matching in low-frequency devices. Hence, $[001]_C$-cut, domain-engineered, Li-doped $K_{0.42}Na_{0.58}NbO_3$, with nearly twice as high permittivity as in $KNbO_3$, were measured showing large k_t values of $\leq$70%.

7.1. Introduction

Potassium niobate $KNbO_3$ (KN) based single crystals are promising for a range of ultrasonic applications[164]. A maximum thickness coupling coefficient k_t of 69%, the highest among known piezoelectrics, has been predicted[165], and experimentally verified[166] for monodomain KN when rotated away from the Z axis by θ=40.5° about the orthorhombic Y axis (Figure 7-1). Combined with its low density (ρ=4.62 g/cm^3), high acoustic velocity (7800–8100ms^{-1}), and low clamped permittivity (ε^S=28–42)[166], the high k_t of 40.5°-cut KN makes it particularly interesting for high frequency transducers. KN shows the same sequence of phase transitions as barium titanate, however, it is orthorhombic at room temperature and up to around 220°C and have a higher Curie point of 435°C[2].

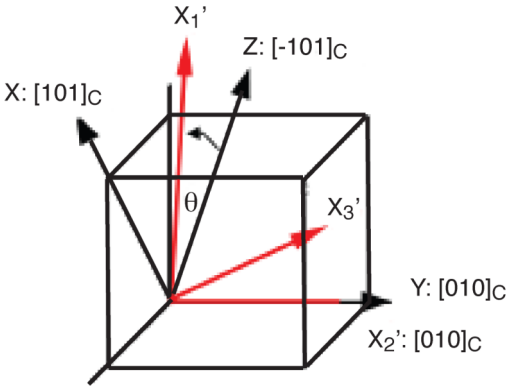

Figure 7-1 – Schematic showing the orthorhombic axes (C stands for cubic axes) and transformed axes (X'_1, X'_2, X'_3) rotated away from the Z axes by θ about the orthorhombic Y axis

The effort and cost involved in preparing off-axis cut, monodomain single crystals of KN are significant. However, k_t values very close to 69% are also predicted in $[001]_C$-oriented 45°-cut KN crystals[166] (Figure 7-1). These samples could be poled from the as-grown state, to give a polydomain "domain-engineered" sample[162] and presumably show similar properties as a monodomain, 45°-cut crystal, and thus lead to considerable cost reduction.

Hence, all measurements presented in this chapter were conducted on $[001]_C$-oriented 45°-cut single crystals (abbreviated 45_{cut} for convenience).

In this chapter, the temperature stability of the coupling coefficients of 45_{cut} monodomain and domain-engineered single crystals of KN were studied upon heating

and cooling through the orthorhombic-tetragonal phase transition. Polishing effect was monitored on thinning to thicknesses below 60μm. Last, the coupling coefficient of as grown unpoled 45_{cut} polydomain KN, and 45_{cut} domain engineered KNLN were recorded.

7.2. Sample preparation

High quality, defect-free crystals of KN were grown by carefully controlled top-seeded solution growth (TSSG) technique at FEE GmbH, Idar-Oberstein, Germany. After poling to a monodomain state at high temperature, three 45_{cut} monodomain plates were cut and a very thin plate was prepared by careful polishing, with nominal dimensions as given in Table 7-1. Additionally, six smaller polydomain plates, were cut from a 45_{cut} as-grown, unpoled crystal of KN.

Sample	No. of samples	Dimensions [mm^3]
Monodomain KN	3	8.1x8.0x0.58
Thin monodomain KN	1	4.7x3.6x0.057
As grown polydomain KN	6	5.8x5.3x0.5
As grown polydomain KNLN -1	1	5.8x9.0x0.36
As grown polydomain KNLN -2	1	7.9x6.3x0.46

Table 7-1 - Samples dimensions

Li-modified KNN crystals [$Li_x(Na_{0.5}K_{0.5})_{1-x}NbO_3$] (xKNLN) were also grown by a TSSG technique at FEE GmbH. The crystals generally had a milkier appearance than as-grown KN, indicative of a higher domain wall density. Two 45_{cut} plates were cut from two different boules (Table 7-1). The Li content in xKNLN was later estimated by comparison of the orthorhombic-tetragonal transition temperature ($T_{FE-FE}\approx177°C$) determined by dielectric measurement, with those for KNLN ceramics (see chapter 6), to be around 2% (2%KNLN).

All samples were sputtered with gold electrodes and poling was conducted at temperatures as close as possible to T_{FE-FE}, with fields typically below 200V/mm[167, 168]. Note that poling of monodomain and polydomain (domain engineered) KN remains a nontrivial task due to its large conductivity at high temperatures[166, 169]. The pyroelectric coefficient at 22±0.5°C was measured using a dynamic method[170].

7.3. Piezoelectric properties of ceramics and single crystals

A typical thickness-extensional response for one of the 45_{cut} monodomain KN plates is shown in Figure 7-2a. For all three samples, k_t was calculated (see chapter 3.4.1) to be between 69 and 70%, no smaller than that for 40.5°-cut samples[166]. In each case, the maximum phase angle θ_{max} was close to 90°, indicative of a truly monodomain state. Other properties are given in Table 7-2.

Sample	ε^{σ} [1kHZ]	tan δ [1 kHz]	p (22°C) [$\mu C/m^2k$]	θ_{max} [°]	k_t [%]
Monodomain KN	92-98	≥0.006	63-65	90	69-70

Table 7-2 - Measured unclamped ε^{σ} and tan δ at 1 kHz, p at 22°C, k_t, and θ_{max} for 45_{cut} monodomain KN

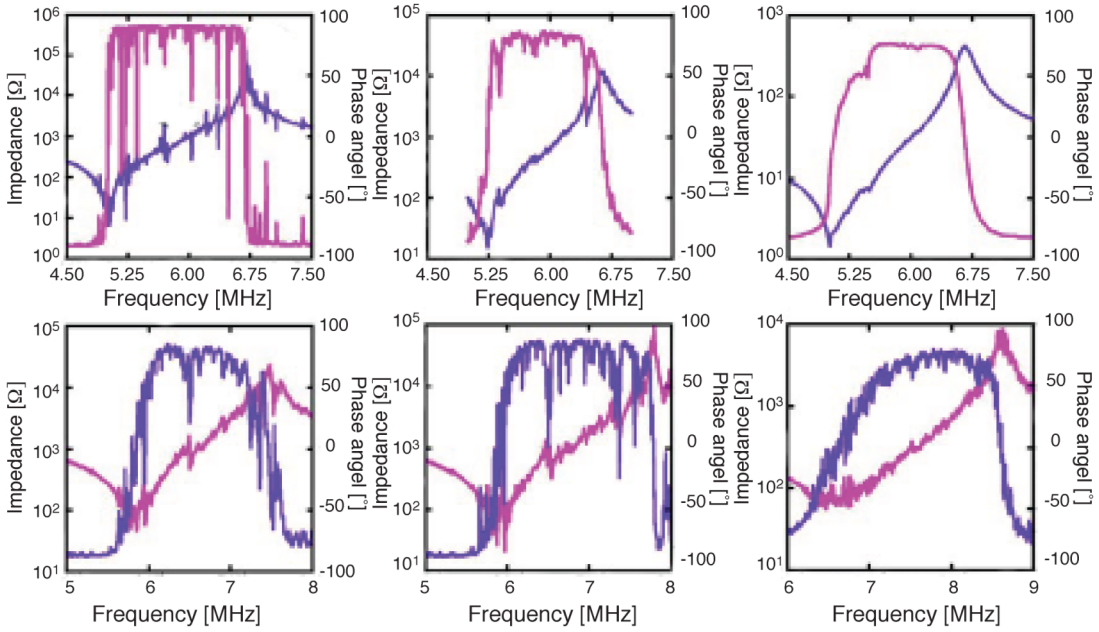

Figure 7-2 - Room temperature impedance spectra for (a) 45_{cut} monodomain KN, (b) the same sample after heating and cooling through phase transition, (c) 45_{cut} monodomain KN thinned to around 60μm, (d) as-grown 45_{cut} polydomain KN, (e) the same sample after domain engineering, and (f) 45_{cut} domain-engineered 2%KNLN sample.

The k_t of one 45_{cut} monodomain plate was measured as a function of temperature every 5–10°C (after stabilizing at each temperature for 10 minutes) between 20 and 180 °C, over two heating and cooling cycles. As shown in Figure 7-3, k_t is extremely stable, varying by only about 5% across the temperature range. Importantly, there is no evidence of depoling. The other two monodomain samples were heated and cooled through T_{FE-FE} at a rate of 2 °C/min, one in open-circuit conditions and one with its electrodes shorted, after which room temperature properties were then re-measured. In both cases, the permittivity was left unchanged. In the open-circuited sample (impedance spectra given in Figure 7-2b), k_t and θ_{max} dropped to 65% and 88°, respectively. Similarly, in the electrically shorted sample, k_t and θ_{max} dropped to 65% and 86°, respectively. Although there is evidence of depoling through the phase transition, it is slight; k_t is still very high (65%) in the thermally treated samples. Notably, this is in stark contrast to the behavior of KNLN ceramics, which depole significantly upon heating and cooling through the orthorhombic-tetragonal phase transition (d_{31} and k_p both decreasing by up to 30%)[171].

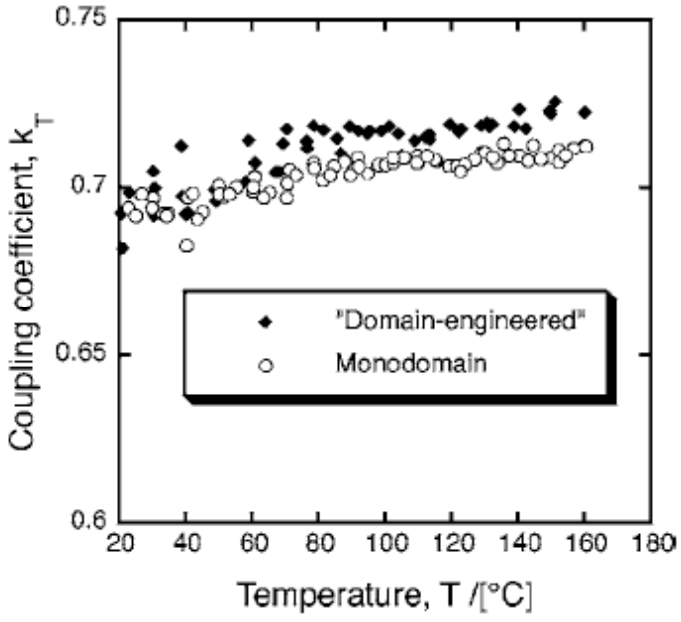

Figure 7-3 - Temperature stability of k_t for 45_{cut} "domain engineered" polydomain KN, poled along the $[001]_C$ direction, and 45_{cut} monodomain KN. The graph shows measurements for two subsequent heating and cooling cycles; no significant depoling is observed.

The impedance spectra for the thinned monodomain KN plate is shown in Figure 7-2c. k_t, θ_{max}, and resonant frequency were found to be 69%, 75°, and 50.1MHz, respectively. The dielectric constant of the sample was calculated to be 108, thus slightly different for the thicker, monodomain samples (92–98). However, this value might be about 5%–10% overestimate due to the difficulty in ensuring complete electrode coverage in such a thin sample. Hence, monodomain KN can be thinned down to a few tens of microns without significant depoling, an important result for the use of these crystals in high-frequency transducers.

Room temperature properties of the 45_{cut} unpoled polydomain crystals of KN are shown in parentheses in Table 7-3. Notably, five out of six of the as-grown unpoled crystals had a strong, spontaneous, and macroscopic polarity, indicated by dielectric constants ($93 \leq \varepsilon^{\sigma} \leq 101$) and pyroelectric coefficients ($53 \leq p \leq 59 \mu C/m^2K$), very similar to those of the monodomain, 45_{cut} crystals. However, the presence of a polydomain structure is indicated by higher losses ($0.04 \leq \tan\delta \leq 0.06$) and lower phase angles ($79° \leq \theta_{max} \leq 86°$). Most importantly, coupling coefficients in the five samples were uniformly high ($64\% \leq k_t \leq 68\%$). Impedance spectrum for one of the five samples is shown in Figure 7-2d.

Sample	ε^{σ} [1kHZ]	$\tan\delta$ [1 kHz]	p (22°C) [$\mu C/m^2k$]	θ_{max} [°]	k_t [%]
Polydomain KN	(131) 127	(0.14) 0.16	(4) 60	(…) 80	(…) 61
Polydomain KN	(97) 96	(0.06) 0.03	(54) 60	(79) 87	(64) 70
Polydomain KN	(97) 97	(0.05) 0.03	(53) 56	(85) 89	(67) 70
Polydomain KN	(93) 93	(0.05) 0.007	(57) 60	(84) 88	(66) 68
Polydomain KN	(96) 94	(0.04) 0.004	(59) 67	(84) 88	(68) 70
Polydomain KN	(101) 98	(0.05) 0.002	(59) 62	(86) 88	(68) 68

Table 7-3 - Measured unclamped ε^{σ} and $\tan\delta$ at 1 kHz, p at 22°C, k_t, and θ_{max} for various as-grown 45_{cut} KN single crystals. Values inside and outside parentheses correspond to measurements before and after poling, respectively.

The reason for the strong, spontaneous polarity of the as-grown KN samples is unclear. In as-grown boules of KN at room temperature, a well-defined ferroelastic 90° and 60° domain wall structure is often apparent[172]. These domain walls are most likely to nucleate due to microdefects within the crystal (for 90° domain walls) and

dislocations at the intersection junction of 90° domain walls (for 60° domain walls)[173]. A carefully controlled thermal gradient across the phase transitions could limit the number of 60° domain walls in the sample due to their higher nucleation energies[168, 174]. However, there is no limitation on the number of 180° domain walls, which will generally form to reduce the depolarizing field. It is possible that the depolarizing field is neutralized due to leakage conduction in KN at high temperatures, removing the tendency to form 180° domain walls and thus leading to a strong, spontaneous polarity. Moreover, this would also explain why the monodomain plates of KN do not significantly depole when heated through T_{FE-FE}.

As shown in Table 7-3, only one of the unpoled tested samples showed a weak spontaneous polarization. For this sample permittivity and losses were high (131 and 0.14, respectively), and the pyroelectric coefficient p was very low ($4\mu C/m^2K$), suggesting the presence of a dense domain structure. The reason why one of the samples, cut from the same as-grown crystal as the other five samples, did not have the same high spontaneous polarity is not clear, however, it is likely due to the greater presence of ferroelastic, 60°, 90° and the unique S-wall domain walls[175].

As shown in Table 7-3, the properties of all 45_{cut} polydomain KN samples could be improved when poled. For all six samples permittivity and losses were reduced and the pyroelectric coefficients, coupling coefficients and maximum angles were increased by poling. High k_t values (61-70%) could be domain engineered in the 45_{cut} polydomain samples (Figure 7-2e). Hence, not only do as-grown crystals show a high k_t, but k_t values as high as those for monodomain samples can be domain engineered in 45_{cut} KN. This is potentially considerably less expensive than preparing monodomain, 45°- or 40.5°-cut single crystals. Finally, k_t is again stable upon heating and cooling to 180°C, as shown in Figure 7-3.

As shown in Table 7-4, the as-grown 45_{cut} samples of 2%KNLN also had a spontaneous, macroscopic polarity, indicated by nonzero pyroelectric coefficients, related to high conductivity at high temperatures. Importantly, high coupling coefficients k_t values (64% and 70%) could be domain engineered in the as-cut samples (Figure 7-2f). Notably, the permittivities in these samples ($\varepsilon^{\sigma} \approx 160$) were nearly twice as high as that of the pure KN samples ($\varepsilon^{\sigma} \approx 95$), which could be helpful for impedance matching in low-frequency devices. These results coincide with reported data on 5%KNLN[176] (it should be noted that no chemical analysis was

conducted on the reported crystals, and measured transition temperature indicate the lithium concentration to be about 2%).

Sample	ε^{σ} [1kHZ]	tan δ [1 kHz]	p (22°C) [$\mu C/m^2k$]	θ_{max} [°]	k_t [%]
Polydomain KNLN	(158) 146	(0.11) 0.13	(22) 67	(41) 71	(53) 64
Polydomain KNLN	(205) 164	(0.33) 0.025	(41) 52	(77) 82	(59) 70

Table 7-4 - Measured unclamped ε^{σ} and tan δ at 1 kHz, p at 22°C, k_t, and θ_{max} for two as-grown 45_{cut} KNLN single crystals. Values inside and outside parentheses correspond to measurements before and after poling, respectively.

7.4. Summary

$[001]_C$-cut and poled domain-engineered samples of KN and 2%KNLN show large thickness coupling coefficients $k_t \leq 70\%$, as do 45°-cut, monodomain KN samples. Moreover, at least in KN samples, the coupling coefficient is stable over a large temperature range. Upon heating and cooling through the orthorhombic-tetragonal transition temperature only minor depoling was observed in 45°-cut monodomain KN. It is likely related to the fact that in as-grown KN, there is a tendency for a spontaneous, macroscopic polarization and high coupling factors. These may follow from large conductivity at high temperatures, which acts to reduce the depolarizing field. Such thermal stability could be useful for medical ultrasound applications, which require sterilization by heat treatment. Finally, 45°-cut, monodomain KN can also be thinned to a few tens of microns, as required for high-frequency applications, without significant depoling.

Chapter 8 - *In-vitro* biocompatibility study of KNLN and PZT

This chapter presents preliminary *in-vitro* biocompatibility study of potassium sodium lithium niobate and lead zirconate titanate ceramics. Human foreskin fibroblast cells were directly cultured on unpoled $K_{0.465}Na_{0.46.5}Li_{0.07}NbO_3$ ceramic samples, and their degrees of attachment and viability over a 10 day period were compared to those of cells cultured on unpoled tetragonal $Pb(Zr_{0.48}Ti_{0.52})O_3$. Cells effectively adhered to the surfaces of both materials and reached confluence within four days in culture, similar to their adherent behavior when cultured on tissue culture (TC) plates. When comparing cell viability after culturing on the two ceramic samples, cells cultured on $Pb(Zr_{0.48}Ti_{0.52})O_3$ samples retained the lowest viability over time, even though microscopic investigation clearly showed similar attachment of cells to the surface. Furthermore, viability values were slightly lower on the two ceramic surfaces when compared to non-coated tissue culture plates. No difference was noted between the viability of cells on positively and negatively charged surfaces of poled rhombohedral $Pb(Zr_{0.52}Ti_{0.48})O_3$ samples.

8.1. Introduction

Bioceramics used for bone repair are shown to be bioactive (possibly by stimulating gene expression[177]) and to improve mechanical properties of bones[178, 179]. Piezoelectric bioceramics are expected to possess additional biofunctionality by producing charges during application of mechanical forces and therefore could be of great interest for implants and other biological applications[97]. A successful implant allows direct cellular contact (or even enhances it) and should not disturb cells growth and proliferation. Thus, when investigating biocompatibility of implants materials, a study of direct cells attachment should be involved[180].

Presently, little is known of the biocompatibility of piezoceramics, and more specifically of $Pb(Zr,Ti)O_3$ (PZT), the most widely used piezoelectric material. As the presence of Pb suggests possible toxicity, $(K,Na,Li)(Nb,Ta)O_3$ and $(K,Na,Li)NbO_3$ piezoelectric ceramics have recently been proposed as an alternative to PZT[59, 60]. These alternative ceramics possess good piezoelectric properties[70, 181] in the range from 20 to 50 °C, and thus are of interest for biological applications, where temperature is fairly stable at ~37°C. In these applications, earlier arguments in chapter 6, of composition and thermal instability (polymorphic phase transition) are of no concern.

In this chapter, preliminary tests on the viability of Human Foreskin Fibroblasts cells seeded on tetragonal and rhombohedral PZT, and 7%KNLN were conducted. Both materials show reasonable viability all through the experimental duration (one week). In addition, the viability of cells on charged surfaces of rhombohedral PZT was compared, however no differences were noted between positive, negative and neutral substrates.

8.2. Ceramic preparation

$K_{0.465}Na_{0.46.5}Li_{0.07}NbO_3$ (7%KNLN) powder was prepared as described in chapter 5. The powder was then pressed to 7mm diameter pellets and sintered under oxygen flow at 1070°C with a dwell time of 1h.

8.2.1. Processing of Lead Zirconate Titanate

Tetragonal $Pb(Zr_{0.48}Ti_{0.52})O_3$ (PZTt) and rhombohedral $Pb(Zr_{0.52}Ti_{0.48})O_3$ (PZTr) PZT ceramic compositions were prepared by solid-state synthesis from PbO 99.9%, ZrO_2 99.96% and TiO_2 99.8% (process optimized –personal communication). The raw powders were weighed to the desired composition and mixed in isopropanol for 6h in a planetary mill, with the aid of ZrO_2 balls. After separating the balls and drying, the powders were calcined at 850°C for 2h. The powders were milled for 6h and dried before they were pressed into 7mm diameter pellets. The pellets were then sintered in a double crucible at 1200°C, with a dwell time of 2h.

8.2.2. Characterization and properties of ceramics

The samples were polished with carbon paper to 1000 grade (~18μm particles). The densities were calculated using measured dimensions and weight of the samples. Theoretical densities were calculated using lattice parameters extracted from XRD, and known ratios of atomic masses. Table 8-1 presents averaged densities of 7-14 samples for each group of materials, showing high densities with only small deviations.

Sample	Calculated density [gr/cm3]	Theoretical Density [gr/cm3]	Density [%]
KNLN7	4.14±0.03	4.5	92.0±0.6
PZTt	7.51±0.08	7.6	98.8±1.0
PZTr	7.60±0.08	8.0	95.0±0.8
PZTr - poled	7.52±0.15	8.0	94.1±1.8

Table 8-1 - Densities of sintered ceramic samples of KNLN7, PZTt. PZTr and poled PZTr

X-Ray diffraction spectra of all samples (7%KNLN and PZT) show normal Perovskite structure (Figure 8-1). No evidence of a second phase could be observed.

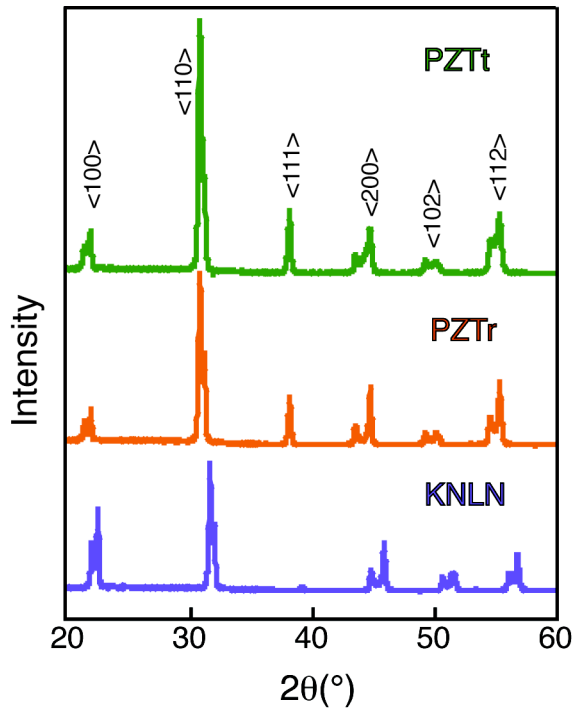

Figure 8-1 - X-Ray spectra of sintered 7%KNLN, PZTr and PZTt ceramics

Surfaces roughness is a key parameter when comparing adhesion of biological tissue to different surfaces[182-185]. Therefore, SEM was used for surface analysis in order to verify similar smoothness of 7%KNLN and PZTt. As can be seen in Figure 8-2, the shape of the porosity and the topography of the two materials are very much alike.

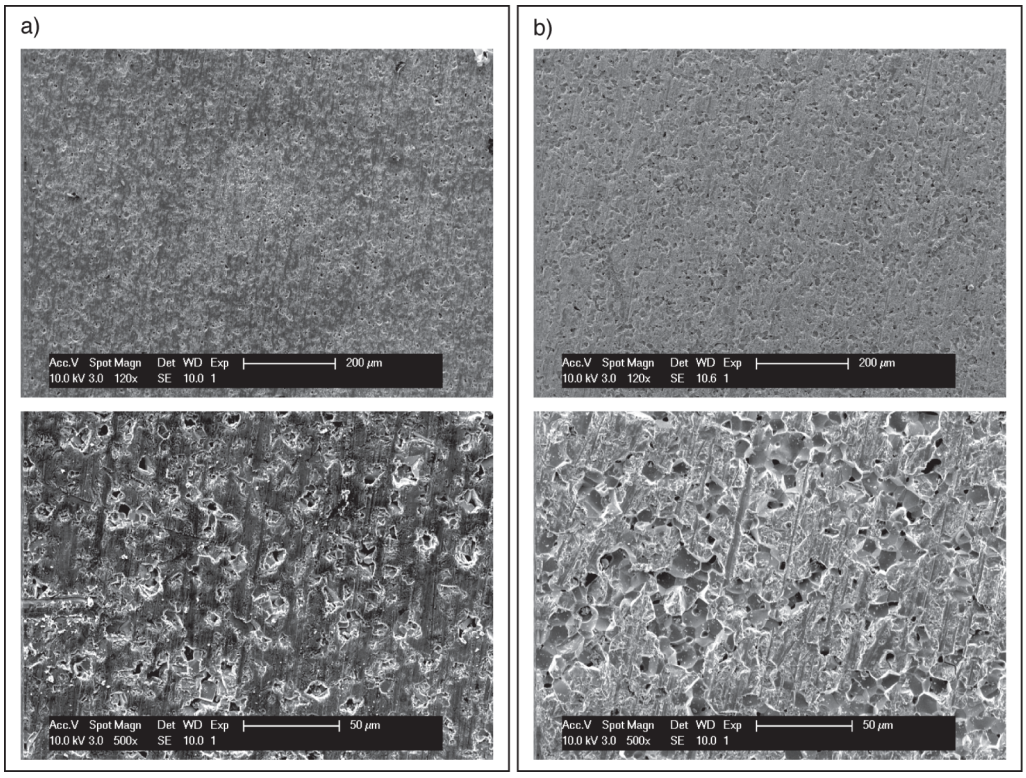

Figure 8-2 - SEM of (a) 7%KNLN and (b) PZTt

PZTr samples were coated with gold electrodes by EMS575X sputtering machine on the parallel surfaces and poled with 30 kV/cm at 100°C for 30 minutes. The dielectric and piezoelectric properties were measured showing good agreement with the literature[186]: ε=1300±50, d_{33}=147±14pC/N], k_p=38±2% and k_t=27±9%.

The direction of the polarization was marked on the samples. The electrodes were then polished away with carbon paper of 1000 grade. Polishing of single crystals was shown to induce small domains at the surface due to stresses created in the mechanical process. The polarity of the samples was verified by a second measurement, for which a sample was re-electroded, showing only small variations in the properties, within accuracy of the measurement.

8.2.3. Surface preparation and cell seeding

The KNLN and PZT samples were sterilized overnight in a 70% ethanol solution and then washed twice with phosphate buffered saline solution, for 20 minutes each time. The samples were then mounted in 96-well tissue culture (TC) plates. Ceramic samples covered the entire well bottom, allowing for cells to only adhere to the upper

surface of the ceramic. Next, Human Foreskin Fibroblasts cells (HFF) were trypsinized, counted using a hemacytometer and centrifuged. Cell pellets were re-suspended in medium (10% Fetal Bovine Serum (FBS, Hyclone), 1% Non Essential Amino Acid (GIBCO), 0.2% beta Mercapto Ethanol, 88.8% DMEM (GIBCO)) to a concentration of 1000 cells/1μl medium. 30,000 cells were then seeded on top of each sample and left for 30 min to adhere. Well volume was then brought to 200μl by addition of 170μl medium. Finally, plates were incubated (37°C, 5%CO_2, high humidity) for the desired culture period (4, 7 or 10 days). Cells were incubated for at least 2hr before performing the first viability measurement.

8.3. Viability of cells on Potassium Sodium Lithium Niobate and Lead Zirconate Titanate

8.3.1. Optical microscopy and SEM of cell attachment

For optical microscopy observations Hamatoxyline and Eosin staining (see section 4.10.1) of the cells was conducted. A confluent monolayer of cells on the surface of 7%KNLN was observed in two different time-points of culture: 6 days (Figure 8-3b) and 10 days (Figure 8-3c). In both time-points the cells reached confluence.

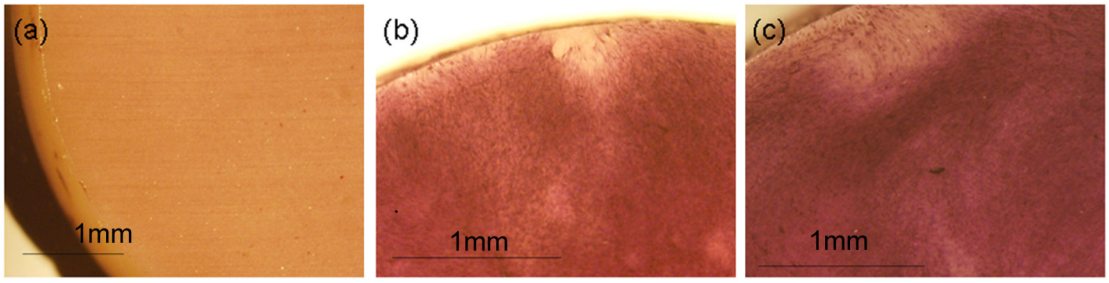

Figure 8-3 - 7%KNLN (a) without cells and with confluent monolayer of human foreskin fibroblasts cells at two different time-points of culture: 6 days (b) and 10 days (c).

More details on the attachment of the cells to the ceramics surfaces were observed with SEM (see chapter 3.7). Images of cell's attachment to 7%KLNL and PZTt samples (Figure 8-4a and b, respectively) show full confluence already after 4 days and one week in culture on both materials. The cells cover and tightly adhere the

entire surface. High magnification reveal cytoplasmic projections of the cells, known as Filopodia, which form focal adhesions that link the cells to the beneath surface, probably via open porosity. No specific difference in cell morphology culture on the PZT compared to the KNLN materials can be pointed.

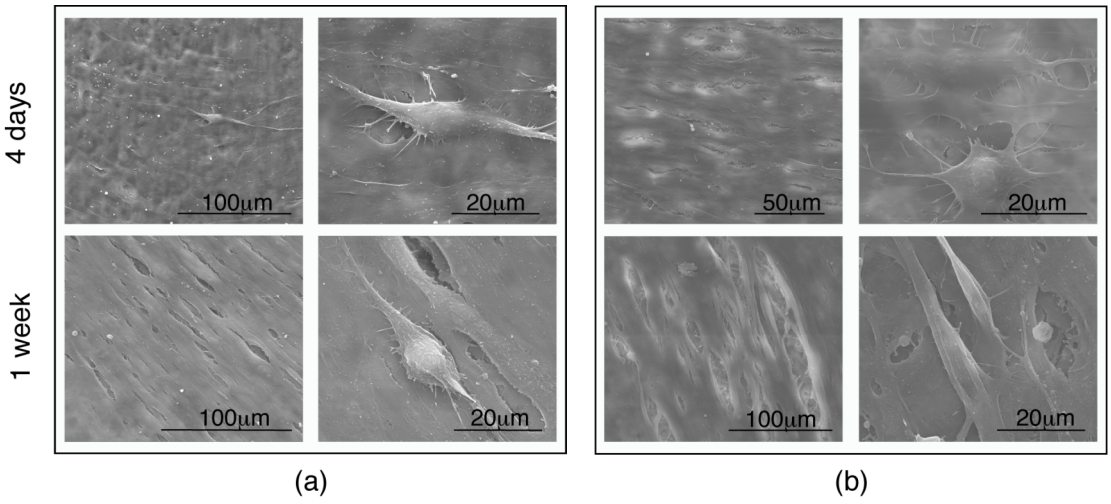

Figure 8-4 - SEM images of cell attachment on 7%KNLN (a) and PZTt (b) after 4 days and 1 week of culture

8.3.2. Fluorescence of live cells

Fluorescence cell viability assay (see chapter 3.10.3) was chosen for microscopically visualization of live cells cultured on the 7%KNNL and PZTt surfaces. After 10 days in culture, the medium of the cells was replaced by a solution of Calcein AM (2μM) and returned to the incubator for 20min. The cells were then washed twice with phosphate buffered saline solution and were taken for visualization under the fluorescence microscope.

Figure 8-5a and b, demonstrate the fluorescence obtained from viable cells cultured on 7%KNLN and PZTt samples after 10 days, showing homogeneously covered surfaces with viable cells exhibiting typical elongated cell phenotype associate with fibroblast cells morphology.

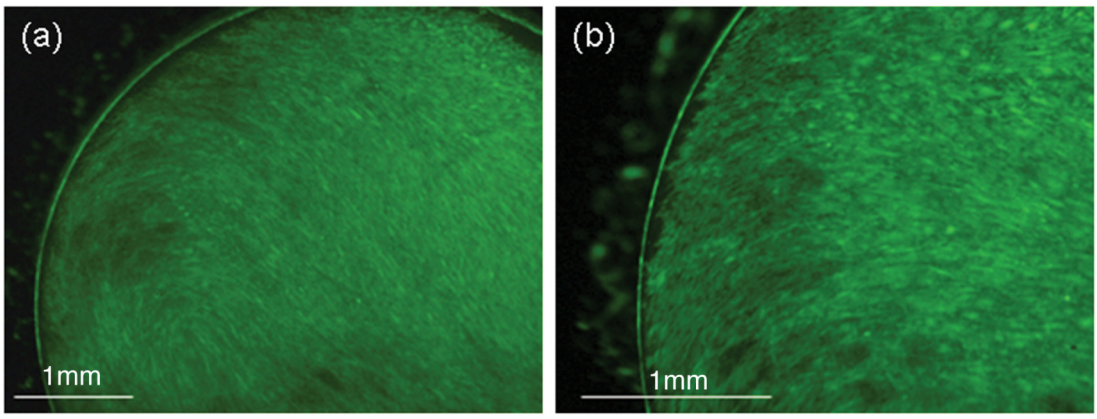

Figure 8-5 - Fluorescence obtained from viable cells homogeneously covering (a) 7%KNLN and (b) PZTt surfaces after 10 culturing days.

8.3.3. Viability of cells on unpoled ceramics

Alamar-Blue assay was used to quntitatively analyse the metabolic activity of the cells, which is proportional to viable cells number (see chapter 3.10.2). Alamar-Blue reduction was measured daily during 1 week of culture. Cells' medium was replaced by 200µl of Alamar-Blue-containing medium (10% AB in medium). Then, samples were returned to the incubator for 6hr (optimized time reported by the manufacturer). After 6hr of incubation, 200µl of Alamar-Blue-containing medium were transferred into a new 96-well plate and their fluorescence was read by spectrophotometer. Finally, the cells were provided with fresh medium and returned to the incubator.

Using the Alamar Blue assay, the intensity of fluorescence was detected and averaged for 4 samples of each group of materials (7%KNLN, PZTt and tissue culture TC plates surving as referance). The normalized intensities of the fluorescence are presented in Figure 8-6 for one week of culture.

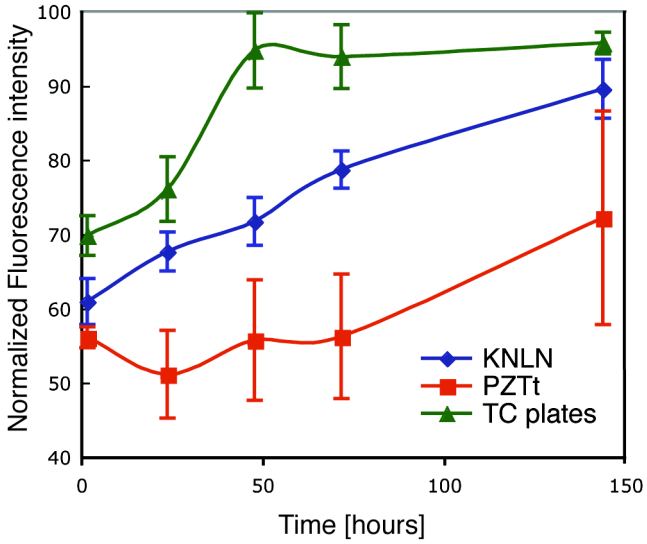

Figure 8-6 - The fluorescence intensity observed using quantitative Alamar-Blue assay, presenting the metabolic activity of cells (proportional to viable cell number) confluent to 7%KNLN, PZTt and TC plates as a function of time

In all types of materials, a typical cell growth curve was obtained: First, cells experienced a recovery phase after being removed from their previous environment. This phase was recorded for TC and PZTt in the first 25hr, and couldn't be observed for KNNL. Cells eventually settled and attached to the substrate surface, followed by an exponential growth phase until confluence. Full confluence was recorded for the TC after 50hr and around 90% confluence for KNNL after 140hr. At this point, contact inhibition from other cells caused them to enter a plateau stage. In the time duration of the experiment, a plateau stage was only detected for cells cultured on TC plates between 50hr and 140hr. In contrast, cells cultured on PZTt only reached 70% confluence within the last time point tested. Throughout the various stages of analysis, cells grown on TC plates demonstrated increased viability, when compared to both KNLN and PZT ($p \leq 0.1$ for both materials at all time points). Cells cultured on PZTt demonstrated the lowest degree of viability over time.

These results agree with previously published paper describing *in-vitro* biocompatibility tests of PZT samples[22]. In this study, mouse fibroblast cells were cultured on tissue culture dishes in the presence of PZT materials. They showed that PZT has little effect on cell's proliferation rate compared to control group, but the number of dead cells increased with time. A similar result was obtained in another study on pulmonary fibroblasts of Chinese hamsters[187].

8.3.4. Viability of cells on poled Lead Zirconate Titanate

Studies correlate electrical charges and currents to bone healing, showing an increase in osteogenesis of the bone around negatively charged surfaces[81, 86-88], and in the presence of currents[83, 84] (see chapter 2.2). Therefore comparison between viability of cells seeded on different charged surfaces of PZTr is of interest.

14 poled PZTr samples were mounted in a 96well plate so that the top surface of 7 samples was positively charged and the other 7 with the negatively charged surface facing up. Using Alamar Blue assay, the fluorescence intensity was detected and normalized. Figure 8-7 presents the data collected during one week for the poled samples as well as for unpoled PZTr samples and TC plates (surving as referance samples).

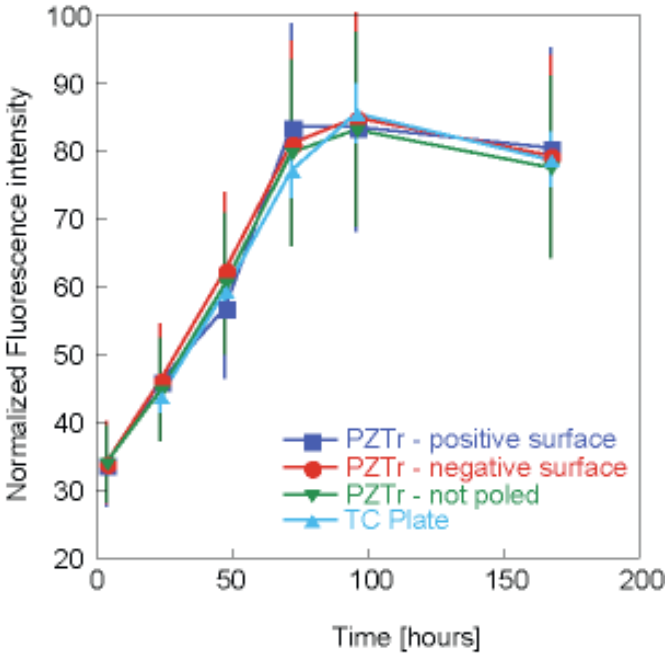

Figure 8-7 - The fluorescence intensity observed using quantitative Alamar-Blue assay, presenting the metabolic activity of cells (proportional to viable cell number) confluent to positive, negative and neutral surfaced of PZTr and TC plates as a function of time

Comparison between viability of cells seeded on different charged surfaces of PZTr showed that the viability on positively and negatively charged PZTr substrates yielded similar ($p>0.05$, average of seven samples for each group) viability levels, as did the nonpolar PZT surface material. This result is not in agreement with *in-vivo*

studies reported in recent papers showing that bone formation is enhanced by negatively charged hydroxyapatite surfaces[86, 87]. However, *in-vivo* and *in-vitro* environments extremely differ and probably cannot be appropriately compared. It is also possible that the polarization charges on ceramic surfaces were completely screened by the charges present in the culture media and were thus not accessible to the cells.

A difference in the viability behavior of PZTt (Figure 8-6) and PZTr (Figure 8-7) should be noted. Whereas PZTt showed lower fluorescence intensity then the measured for tissue culture plates, PZTr (in all polarization states) shows similar intensities. This divergence might be due to the different compositions, however could be as well due to the different cell passage (the number of times the cells were divided before used) in the two experiments. It is possible that since experiments on PZTr were conducted using a smaller cell passage, cells were less sensitive to the surface and therefore showed higher viability.

8.4. Summary

Biocompatibility of potassium sodium lithium niobate and lead zirconate titanate pieozoceramics has been studied *in-vitro* because of their great interest as implant materials and for other biological application.

Beyond the necessity of biocompatibility evaluation of both materials, implant based materials should allow cells attachment and even promote tissue regeneration. Many groups have been working on implant surface modification which best promote tissue regeneration, like in the case of Ti implants which are chemically coated with oxidative layer or with biofunctional proteins to improve bioactivity of the implant[180]. Hence, direct attachment of cells to the surface of the materials and their effect on cell viability is crucial and were examined.

Human foreskin fibroblasts cells were cultured directly on non-poled 7%KNLN samples, and their attachment and viability during 10 days were examined. The results were compared to those obtained from cells cultured on non-poled tetragonal PZT.

The results show that the attached cells were able not only to remain viable for prolonged time but also to proliferate and growth on the PZT and KNLN ceramics prepared without any surface modifications. The cultured cells exhibited typical growth behavior on both materials, compared to the tissue culture plates. However, the number of viable cells was highest on the tissue culture plates, and was lower on the KNLN and PZT samples. On the PZT samples, cells exhibited the lowest viability in all time points, although microscopic investigation clearly showed similar attachment of cells to the surface of both 7%KNLN and tetragonal PZT ceramics. No difference was noted between the viability of cells on positively and negatively charged surfaces of poled rhombohedral PZT samples.

Chapter 9 - Hydroxyapatite – KNLN system

Piezoelectricity can be found in various biological systems, including the bone. Studies were able to isolate the piezoelectric component, collagen fibers, in a hydroxyapatite matrix. This discovery allows better understanding of the behavior of the bone and thus, better engineering of implant materials for faster healing.

After the biocompatibility of KNLN was demonstrated in chapter 8, the use of hydroxyapatite-piezoelectric composite was considered to electro-mechanically activate bone growth and tissue growth around bone. Another possibility is to implant KNLN into bone as a pressure sensor and energy harvester.

Due to a strong chemical reaction, it seems unreasonable that KNLN could be used when big interfaces with hydroxyapatite are needed (embedded sensor in hydroxyapatite implant, for example). However, since small piezoelectric signals were found by AFM in the composite, it could possibly be of biological use.

9.1. Introduction

Bones are constructed of composite based on hydroxyapatite mineral and piezoelectric collagen. This piezoelectricity of the bone has been suggested to stimulate bone growth due to the charges and currents involved (see chapter 2.2).

Implants made of hydroxyapatite are currently being used[188-190]. And even though they were shown to be polarizable (see chapter 2.2.2), they still miss the piezoelectric quality, which enables the implant to create changing chargers as pressure is applied on the implant and thus encourage bone growth.

Composites of hydroxyapatite and barium titanate ($BaTiO_3$) have been studied[98-100]. These studies show that only for very high concentration of $BaTiO_3$ signs of piezoelectricity can be detected, due to a reaction between the two components.

In this chapter, potassium sodium lithium niobate, $(K_{0.465}Na_{0.465}Li_{0.07})NbO_3$ 7%KNLN, was used as hydroxyapatite-piezoelectric composites, in one of the two possibilities:

1. The hydroxyapatite-piezoelectric composite requires prior to all, chemical stability between the different components. Therefore, the interface between sintered ceramics (hydroxyapatite-7%KNLN pellets) was investigated after thermal treatment at elevated temperatures.
2. In the bone, collagen fibers are imbedded in the hydroxyapatite, as separate regions. Thus, integration of small piezoelectric "zones" into the hydroxyapatite matrix was investigated (powder-particle composite).

9.2. Preparation of Hydroxyapatite

Dehydroxylation of hydroxyapatite occurs at all elevated temperatures in a small amount but significantly more above 800°C and as sintering temperatures increase[191-193]. Hydroxyapatite is mainly converted to β-tricalcium phosphate (TCP) having Whitlockite structure[92, 95]:

$$Ca_{10}(PO_4)_6(OH)_2 \rightarrow Ca_3(PO_4)_2 + Ca_2P_2O_9 + H_2O$$

Due to the constant dehydroxylation, the ratio Ca/P in the material varies. The stoichiometric hydroxyapatite $3\left[Ca_3(PO_4)_2\right]\cdot Ca(OH)_2$ has a Ca/P ratio of 1.67 whereas in the bone this ratio is 1.5 due to calcium deficiencies. This flexibility of stoichiometry allows bone hydroxyapatite to act as a buffer to the composition of blood[194], and therefore calcium deficient hydroxyapatite are of great biological interest.

In this work, reagent grade hydroxyapatite (sigma-Aldrich, synthetic) was used. X-ray diffraction (XRD) of the powder at room temperature shows no presence of β-TCP. Furthermore, powder kept in a humid atmosphere for 24 hours show exactly the same spectra, as can be seen in Figure 9-1. Both powders correspond precisely to ICDD data of hydroxyapatite (01-074-0566).

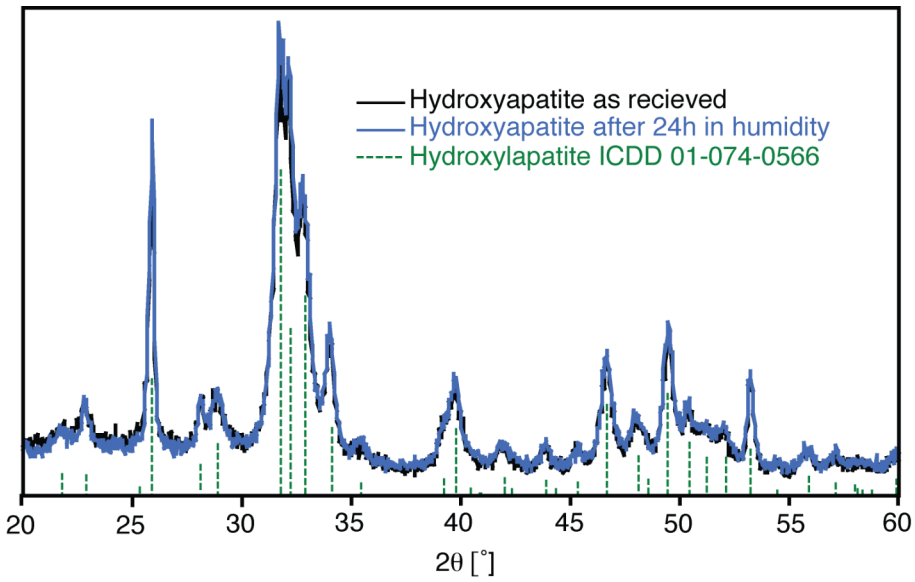

Figure 9-1 - XRD spectra of hydroxyapatite powder as received and after 24h in humid atmosphere compered to ICDD data sheet (01-074-0566)

The powder (as received) was pressed in a uniaxial press to 9mm diameter pellets with thickness of about 5mm. Considering the dhydroxylation process and grain growth (occurring[95] at sintering temperatures above 1000°C), sintering temperatures were fixed at 1000°C. Sintering was conducted in a Lenton tube furnace with dwell time of 1 hour.

It has been previously shown that the sintering atmosphere can minimize volatilization and deficiencies of elements[50, 69, 70, 142, 144]. However, similar XRD

spectra were observed on samples which were sintered in air, argon and oxygen atmospheres (Figure 9-2). With good agreement to the literature[92, 94], β-TCP phase (Whitlockite ICDD 00-009-0169) is detected in addition to the hydroxyapatite peaks (ICDD 01-074-0566), creating a two-phase system.

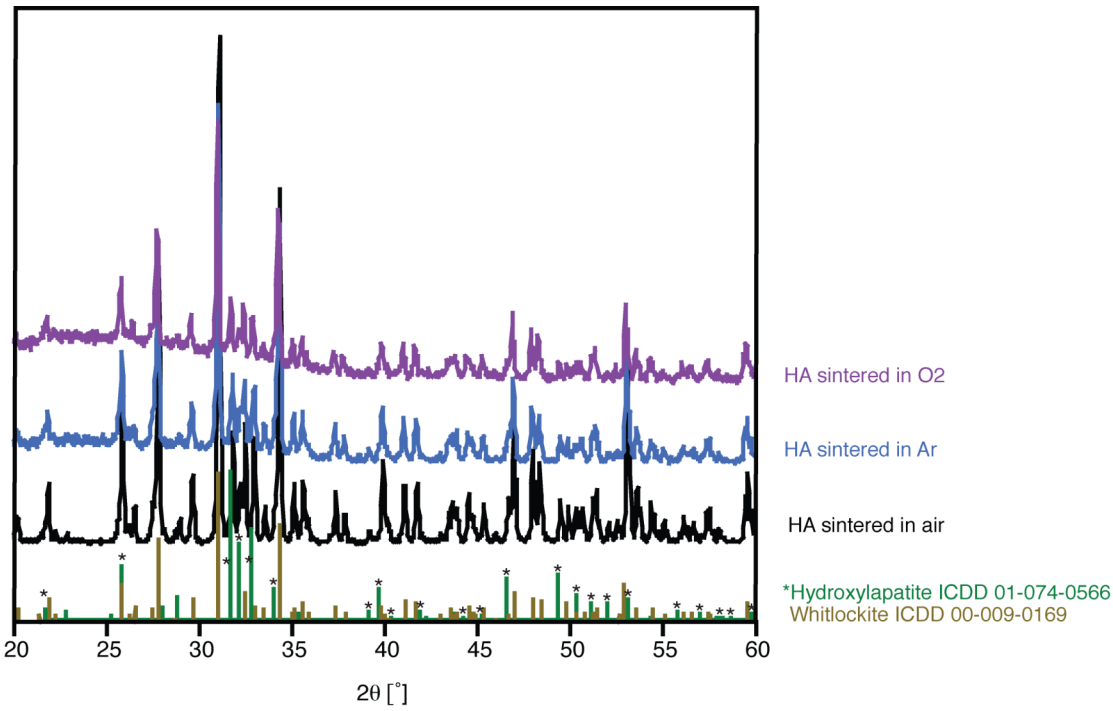

Figure 9-2 - XRD spectra of hydroxyapatite sintered at 1000°C in air, Ar and O_2 atmospheres compared to ICDD data sheets of hydroxyapatite (01-074-0566) and Whitlockite (00-009-0169)

9.3. Hydroxyapatitie - 7%KNLN pellets

Sintered samples of 7%KNLN and hydroxyapatite were prepared as described in chapter 5 and section 10.2, respectively. The samples were polished with carbon paper up to 4000 grade (~5μm) in order to enable as large and tight interaction surface as possible. The polished surfaces were placed to face each other and a small weight of few grams was placed on top of them so that pressure was induced during the thermal treatment. Three temperatures were tested for the thermal treatment: 950°C, 1000°C and 1200°C for 4 hours each.

After cooling the samples and removing the weight, the pellets spontaneously separated. SEM observations of the surfaces are presented in Figure 9-3 after treating the samples at 950°C. Un-reacted areas on hydroxyapatite and 7%KNLN

(Figure 9-3a and b, respectively) were observed. The non homogeneity of the surface is probably due to a movement of the two pellets in respect to each other so that part of the surface was not covered. Grain growth occurred in both ceramics due to the high temperature annealing. At the interaction areas, products of a chemical reaction can be observed on both hydroxyapatite and 7%KNLN (Figure 9-3c and d, respectively). Similar surfaces were detected on the samples treated at 1000°C.

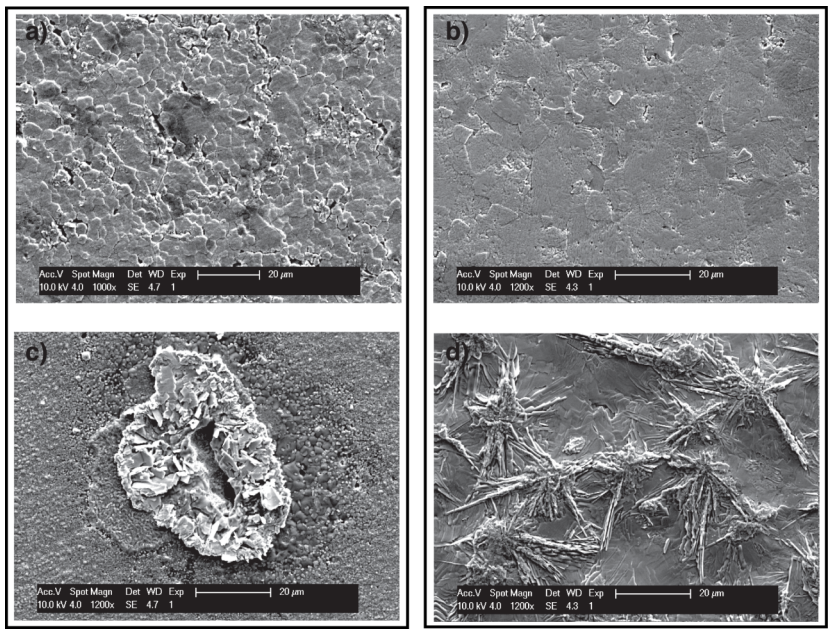

Figure 9-3 - Un-reacted and interaction areas on ((a) and (c) respectively) hydroxyapatite and ((b) and (d) respectively) 7%KNLN pressed and sintered at 950°C for 4 hours

At higher treatment temperature (1200°C) dramatic reaction occurs at the surfaces of the samples. Figure 9-4a shows the reaction on the surface of hydroxyapatite. Two products of the reaction, plate like and needle shaped particles, can be found closely packed to cubic particles (Figure 9-4b and c). Figure 9-4d is the enlargement of marked area in image Figure 9-4c. From this image the thickness of one needle can be estimated to be in the order of few hundred nanometers.

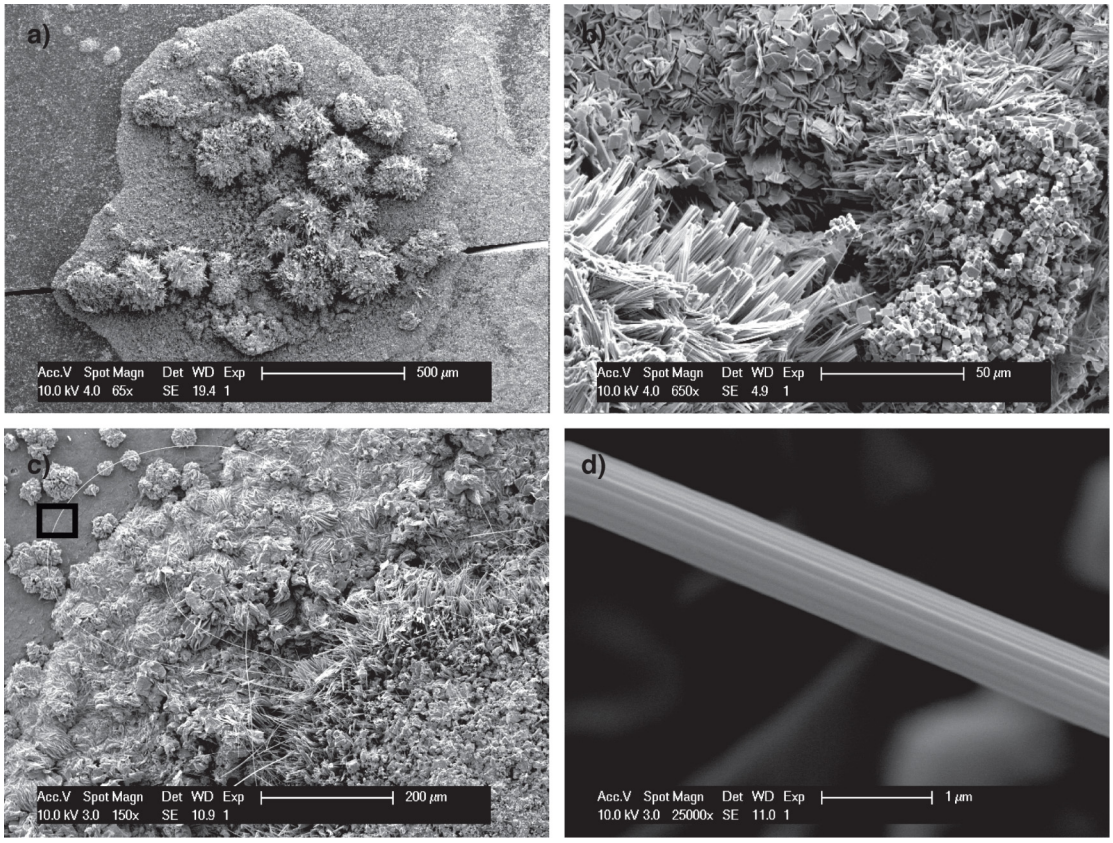

Figure 9-4 - (a) Surface of pressed hydroxyapatite after sintering at 1200°C, showing (b and c) two products of the reaction, plate like and needle shaped particles, closely packed with cubic particles (d) enlargement of marked area in (c)

The compositions of the different particles, cubic, plate and wire shaped, were examined by EDX. A comparison of the composition is given in Figure 9-5. Lithium can not be detected by EDX due to it's very low energy L-edge x-ray absorption, but since the cubic particles are of K:Na:Nb:O atomic ratio corresponding to the potassium sodium niobite family, it seems reasonable to assume the composition of these particles is indeed 7%KNLN. The composition of the wires appears to be of $KNbO_3$ with low doping concentrations of Na, Ca and P whereas the composition of the plate-like particles come across to be K, Na and P doped $CaNb_2O_3$.

Chemical reaction was previously reported[100] between barium titanate and hydroxyapatite when sintered as a composite above 900°C. Barium titanate was reported to disappear and the appearance of $CaTiO_3$ and Ba_2TiO_4 was noted as the product of the reaction.

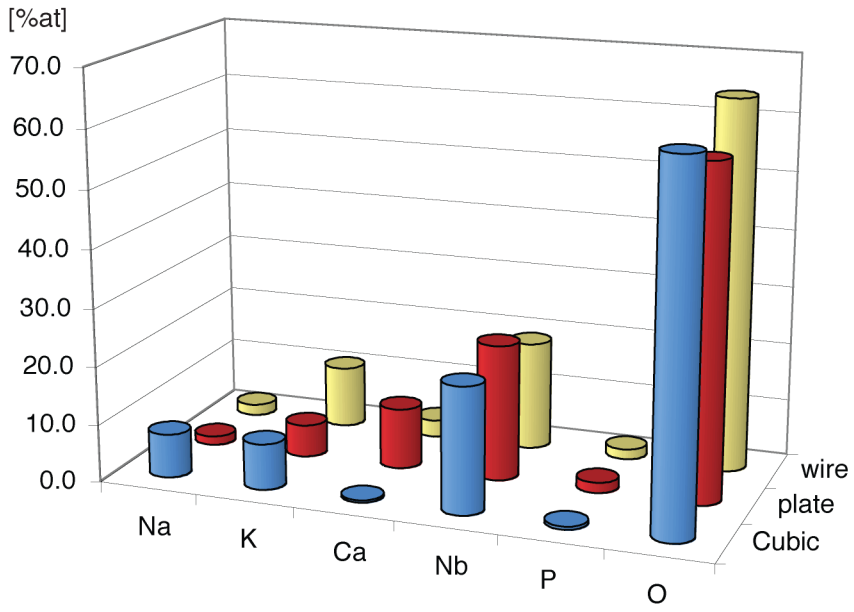

Figure 9-5 - Chemical analysis of cubic, plate and wire shaped reaction products particles

On the surface of 7%KNLN (Figure 9-6) only tube shaped particles were observed, growing from the 7%KNLN surface (cubic shaped particles), and having similar composition as the wires measured on the hydroxyapatite surface. It is believed that while handling the samples, the tubes disconnected from the 7%KNLN substrate. The radius of the tubes is of few microns, and they reach few tens of microns in length.

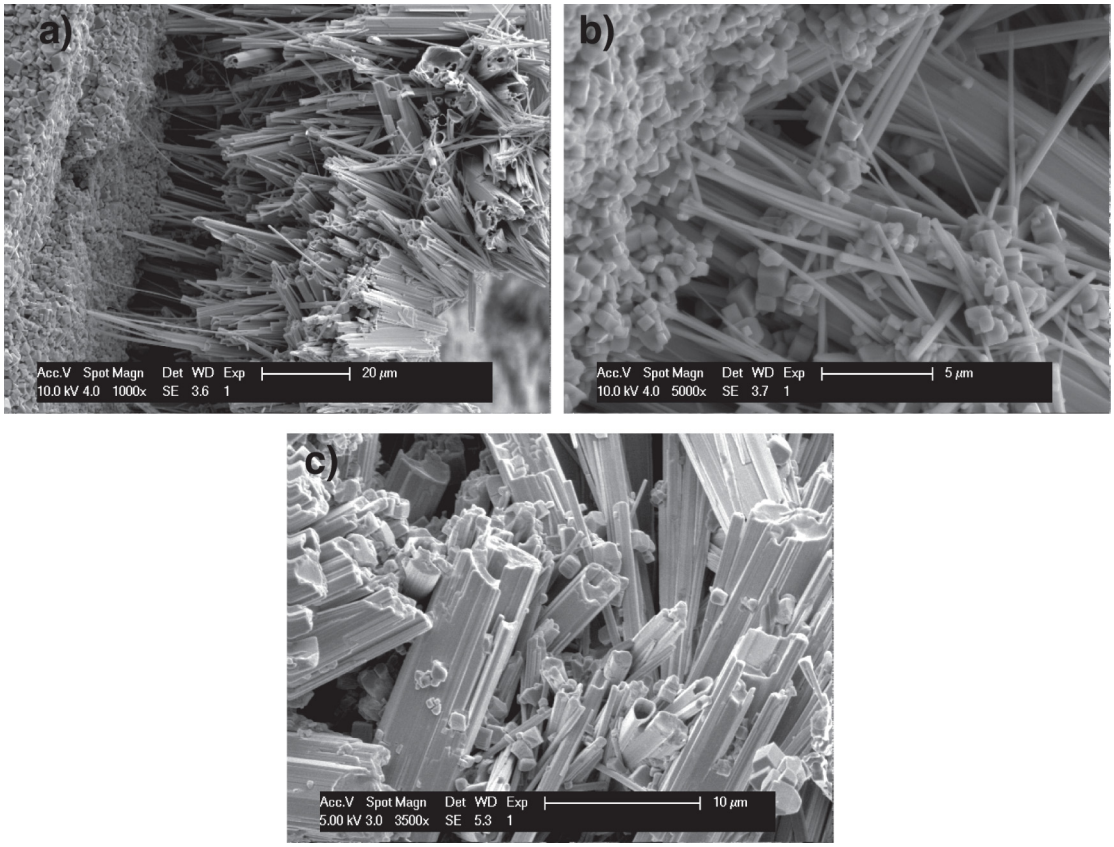

Figure 9-6 - Surface of pressed 7%KNLN showing tube shaped particals

Following these strong chemical reactions, it is unlikely KNLN pellets could be used as sensors in implants without surface chemical treatment, which would suppress the reaction with hydroxyapatite.

9.4. Powder - particle composite

Sintered pellets of 7%KNLN were crushed to particle size of few hundred microns and mixed with hydroxyapatite powder in the weight ratio 1:1 (50%wt= 86%at=41%vol). The mixture was then pressed with a uniaxial press to 7mm diameter pellets and sintered at different temperatures with dwell time of 1 hour, under oxygen flow.

SEM investigation show 7%KNLN particles imbedded in hydroxyapatite powder after sintering at 800°C (Figure 9-7a) and 1000°C (Figure 9-7b). Irregularly shaped particles are observed close to the interface separating 7%KNLN particles and hydroxyapatite. No 7%KNLN particles could be observed at 1200°C (Figure 9-7c).

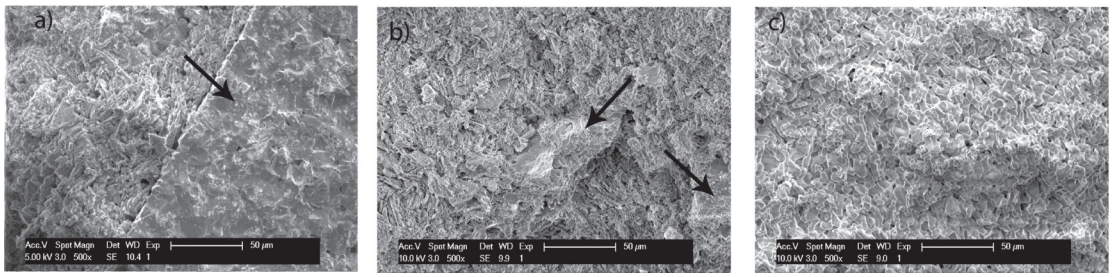

Figure 9-7 - SEM images of powder-particle composites sintered at (a) 800°C, (b) 1000°C and (c) 1200°C. Arrows indicate 7%KNLN particles.

X-ray diffraction reveals that even at sintering temperature as low as 800°C, peaks corresponding to calcium diniobium oxide phase (ICDD 01-071-2406) are present (mainly seen at 23-24 2θ indicated in Figure 9-8). As the sintering temperature increases, these peaks become bigger. At 1200°C peaks corresponding to 7%KNLN could not be traced.

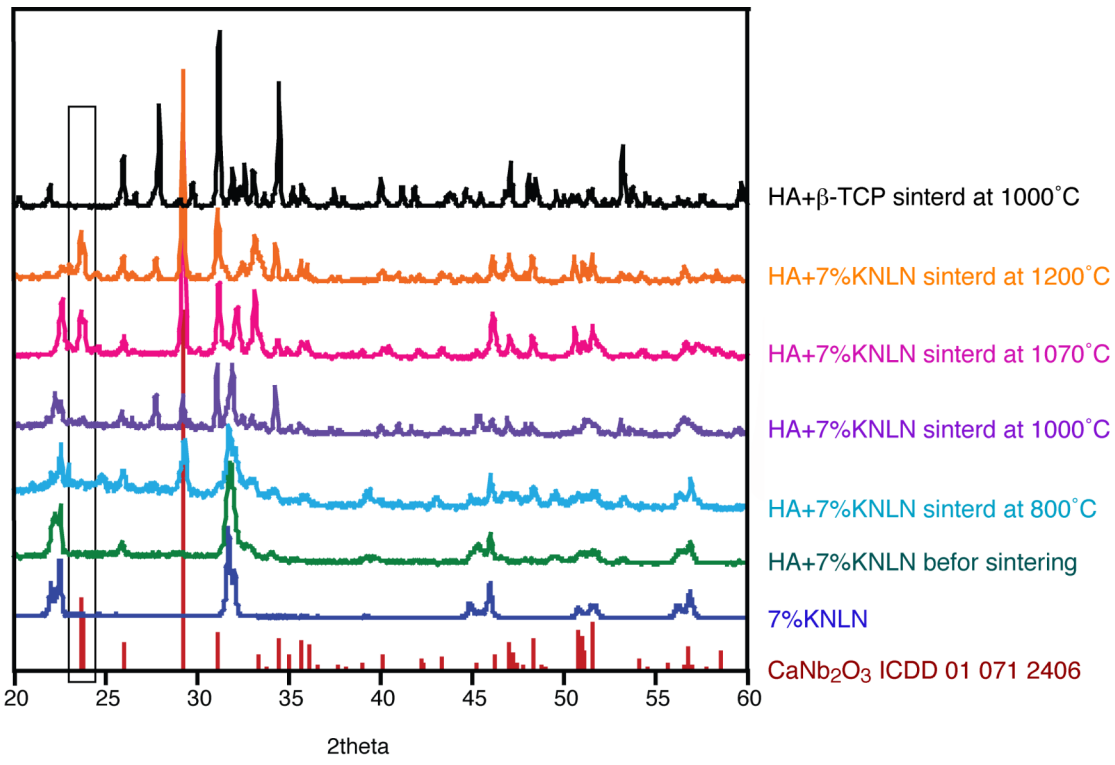

Figure 9-8 - XRD spectra of powder-particle composites sintered at different temperatures. The rectangle highlights peaks corresponding to calcium diniobium oxide phase

PFM measurements were used as a second indicator for the presence of ferroelectric 7%KNLN in the hydroxyapatite-7%KNLN composite sintered at 1000°C. The sample surface was polished with 1μm diamond paste and after cleaning with acetone, gold electrodes were deposited on one surface. Particles of 7%KNLN were detected by the optical microscope and scanned with a PFM tip, when the tip is serving as a top electrode. Domain structure could be clearly observed on the embedded 7%KNLN (Figure 9-9a) having lower domain density and bigger domain size, then observed on un-poled 7%KNLN ceramic sample (Figure 9-9b).

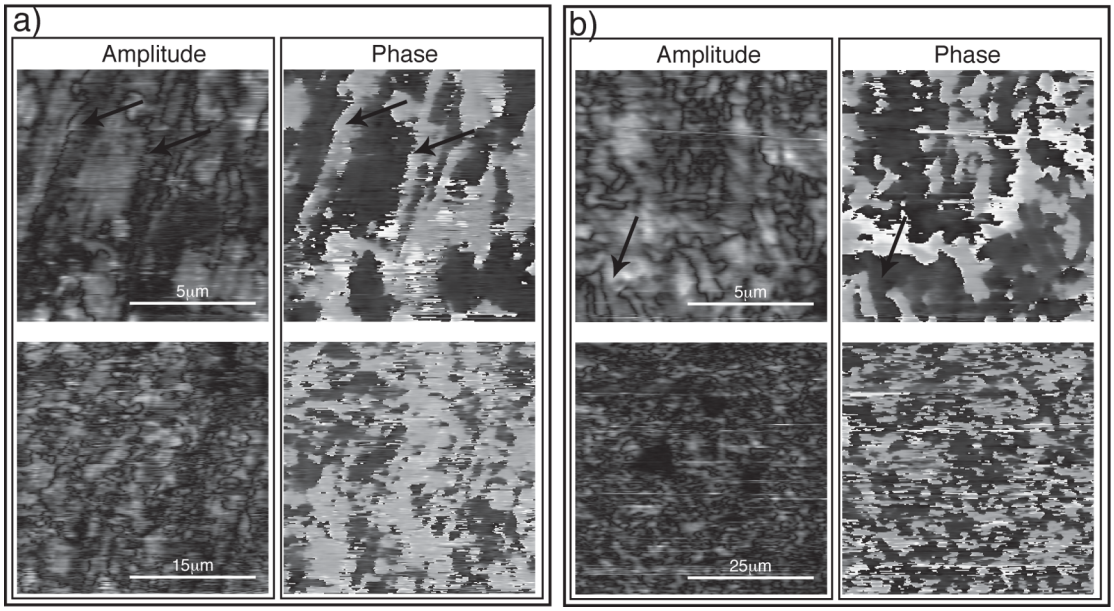

Figure 9-9 - PFM images of amplitude and phase of (a) 7%KNLN embedded in a powder-particle composite and (b) un-poled 7%KNLN ceramic. 90° and 180° domain walls are indicated by arrows

In tetragonal phase, as is the case for 7%KNLN at room temperature (see chapter 6), only 6 polarization directions are possible, perpendicular or parallel to each other. The angle between any two dipoles when encountering at the domain wall, can be either 90° or 180°. 90° domain walls are characterized by lamellar or zigzag patterns created due to the restricting 90° angles between the interacting domains. 180° dipoles can arrange in any configuration and are recognized by their irregular shape. Only 180° domain walls were spotted on the un-poled 7%KNLN, whereas the embedded 7%KNLN displays both 90° and 180° domain walls (indicated by arrows).

In ferroelectric materials, indications to phase transitions are noted by peaks in the permittivity. For 7%KNLN, a peak around 500°C was expected due to the ferroelectric-paraelectric phase transition (see chapter 6). However, the measured permittivity as a function of temperature (Figure 9-10a) on samples sintered at 1000°C reveals no such peaks.

Figure 9-10b presents a rounded loop indicating high conductivity in the sample, which is most probably imposed by the hydroxyapatite. This high conductivity prevents poling of the sample. As a consequence, since the crystallites in the piezoelectric ceramic are not oriented, the piezoelectric effect is limited.

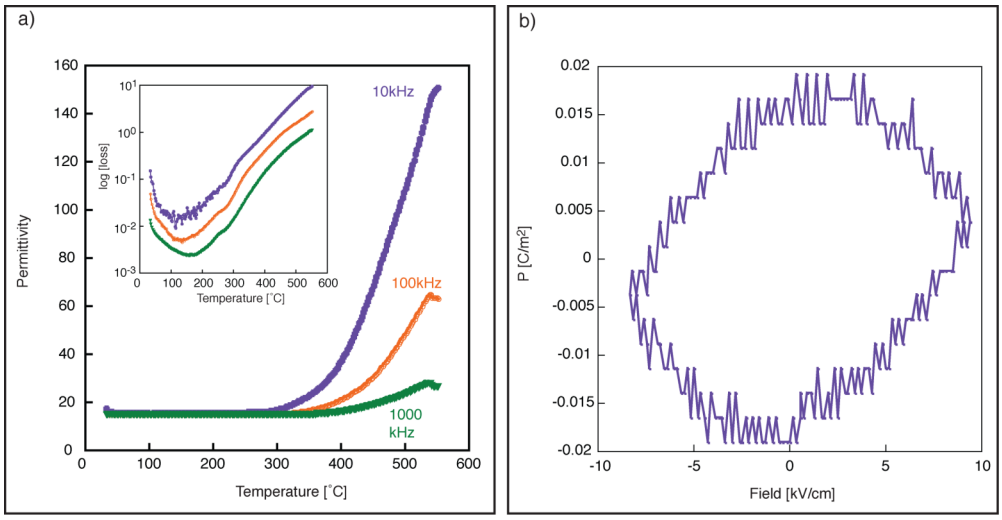

Figure 9-10 - (a) Dielectric measurement and (b) hysteresis loop of powder-particle composite sintered at 1000°C

Hence, even though piezoelectricity could be detected by PFM on a microscopic scale, piezoelectricity could not be measured on the macroscopic scale. However, since typically cells are of the order of microns, it is possible that cells could be influenced by the piezoelectric effect of the piezoelectric component in the composite.

9.5. Summary

Hydroxyapatite is the major component of the bone, and thus, artificial hydroxyapatite has been used as a bone graft material in clinics for decades. However, these implants are lacking the piezoelectric character attained in the natural bone from piezoelectric collagen fibers imbedded in the hydroxyapatite.

In this chapter two possibilities to imbed piezoelectric ceramic in hydroxyapatite were described. 7%KNLN has been chosen as the piezoelectric ceramic component after displaying reasonable and reproducible piezoelectric properties around room temperature (see chapter 5), and biocompatibility (see chapter 9).

The reaction at the interface between two polished ceramic pellets of hydroxyapatite and 7%KNLN was examined. It has been demonstrated that thermal treatment of the pellets above 950°C resulted in a chemical reaction forming pellet-like particles with the composition of K, Na and P doped $CaNb_2O_3$, and wires and tubes with the composition of Na, Ca and P doped $KNbO_3$, both verified by EDX. Therefore, unless implanted directly into bone, it is hard to believe introducing 7%KNLN pellets in a hydroxyapatite implant, interesting as *in vivo* sensors, would be possible without developing a chemical reaction, producing products that are not piezoelectric.

Composite of imbedded 7%KNLN particles in hydroxyapatite powder was sintered. XRD and SEM investigations, revealed 7%KNLN, HA and β-TCP phases when sintered at 800°C. Above 1070°C, $CaNb_2O_3$ phase was increasingly detected whereas 7%KNLN was slowly disappeared, until at 1200°C no traces of 7%KNLN are observed. PFM observations confirmed the presence of the piezoelectricity 7%KNLN phase via 90° and 180° ferroelectric domain structure.

Due to high conductivity of the samples, emerging due to proton transportation in the hydroxyapatite structure (see chapter 2.2.3), poling of the composite was not possible. As a result, the small 7%KNLN crystallites were not oriented and piezoelectric measurements were not feasible.

However, composite containing HA powder and sintered 7%KNLN particles is potentially adequate to serve as a mineral-piezoelectric composite because of its local piezoelectricity. This localized piezoelectricity might be enough to replace the piezoelectricity induced by the collagen in natural bones. The $CaNb_2O_3$ phase should still be confirmed to be biologically compatible.

Chapter 10 – Conclusions and outlook

Conclusions

The lead zirconate titanate (PZT) family of materials consists of many varieties that cover nearly the whole spectrum of piezoelectric applications. However, due to the toxicity of lead, the use of these materials has been banned in some applications and restricting regulations are implemented in medical applications. Hence, extensive studies on lead free piezoelectrics are constantly taking place.

From within the understanding of the correlation between structure, phase transitions, and properties of PZT, two lead free systems, bismuth sodium barium titanate (BNBT) and potassium sodium lithium niobate (KNLN), were investigated in this thesis. Their phase diagrams were constructed from observations on neutron, XRD and Raman spectra and measurements of dielectric and piezoelectric properties.

Figure 10-1 presents the phase diagrams of BNBT and KNLN with similar temperature and composition scales as commonly presented for PZT[2].

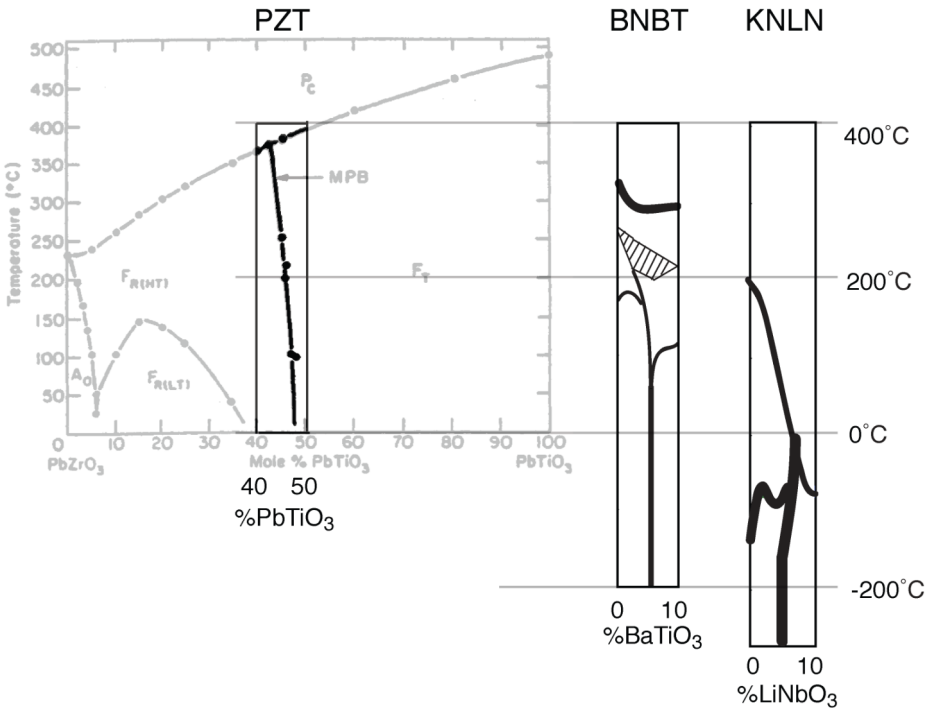

Figure 10-1 - Phase diagrams of PZT[2], BNBT and KNLN

It could be clearly seen, that the BNBT diagram shows nearly vertical phase boundary (MPB) near room temperatures, similar to PZT, and both BNBT and KNLN systems show even less inclined boundaries at low temperatures than PZT, proving MPBs could be found in lead free piezoelectrics. Figure 10-2 shows an enlargement of the composition range in the proximity of the MPBs. These MPBs are of great importance for applications requiring wide temperature range (medical devices used at room temperature and sterilized at 140°C, for example).

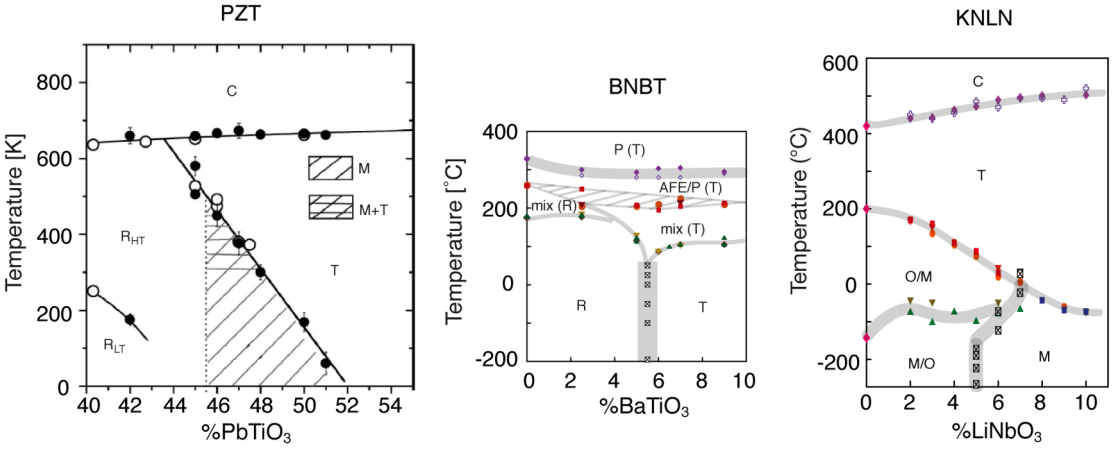

Figure 10-2 - Phase diagrams of PZT[13], BNBT and KNLN - enlargement of the regions near MPBs

Just like in PZT, a peak in properties was measured in the proximity of the MPB resulting from flattening of free energy profile, however, the properties presented in this thesis are still lower than the measured properties in PZT. The reason for this disparity could be due to the existence of two phase transitions in PZT[195], from rhombohedral to monoclinic and from monoclinic to tetragonal, within a composition range of 6%$PbTiO_3$, whereas only one phase transition exists in BNBT and in KNLN near room temperature (rhombohedral to tetragonal and orthorhombicaly distorted monoclinic to monoclinc phases, respectively).

Similarly to PZT, large domain wall contribution to the permittivity was found for BNBT ceramics at room temperature. A “soft-like” piezoelectric behavior was observed. However, as opposed to the stable ferroelectric phases up to ~400°C in PZT, in BNBT significant depolarization occurs as antiferroelectric (or paraelectric) second phase emerges at temperatures above ~200°C and ~100°C for rhombohedral

and tetragonal compositions, respectively, coexisting with the ferroelectric phases. This depolarization is a significant temperature limiting factor for some applications.

One of the greatest challenges in developing new lead free materials is to find a family with properties that are as diverse as those in PZT. At present, lead-free materials are most often developed with a specific application in mind, such as $(Na_{0.475}K_{0.475}Li_{0.05})(Nb_{0.92}Ta_{0.05}Sb_{0.03})O_3$ for ultrasonic transducers for wire-bonding applications[196], $(Na_{0.49}K_{0.49}Li_{0.02})NbO_3$+0.45mol%CuO in shear mode ultrasonic motors[197] and $x(Na_{0.5}Bi_{0.5})TiO_3$-$y(K_{0.5}Bia_{0.5})TiO_3$-$zBaTiO_3$ and KNN for single element transducers[198]. However, the narrow specialization of each composition is a serious limiting factor for presently used lead free materials as it increases development and production costs. This suggests that the search for new, more universal lead-free piezoelectrics should continue.

In this thesis, $KNbO_3$ and $(Na_{0.4116}K_{0.5684}Li_{0.02})NbO_3$ single crystals rotated away from the Z axis by θ=45° about the orthorhombic Y axis ($[001]_C$-cut) were investigated with the aim to develop materials with ultrahigh thickness coupling coefficients, kt. Large $k_t \leq 70\%$ were found in both monodomain and domain engineered crystals, exhibiting temperature stability and good mechanical and piezoelectric properties upon thinning to thickness below 60μm ($k_t \geq 65\%$). These results indicate a considerably cheaper preparation of single crystals, than preparing optical quality, monodomain, 40.5°-cut single crystals, as was required before in order to replace PZT piezoelectrics. Together with the appropriate permittivity of $(Na_{0.4116}K_{0.5684}Li_{0.02})NbO_3$ they could be also suitable for low-frequency applications (1 MHz range).

Another disadvantage of KNLN ceramics over PZT is their sensitive processing procedure. As was shown in this thesis, reproducibility of piezoelectric properties highly depends on small changes in stoichiometry. Modifications of the ceramic processing were addressed, leading to reproducible properties, however, these were still significantly lower then published properties for KNLN samples with similar compositions, and of PZT.

The research for lead free piezoelectrics focuses on solving environmental problems of toxicity during production and disposal of devices. However, other applications for lead free piezoelectrics are of interest, such as body embedded sensors and others. However, biological applications require biocompatibility as well as sufficient piezoelectric properties.

Preliminary biocompatibility tests conducted in this thesis with human cells, indicated the cells keep their viability during one week of experiment, when cultured on top of $(Na_{0.465}K_{0.465}Li_{0.07})NbO_3$ and PZT ceramics substrates. These encouraging results are the first step to establish biocompatibility of these materials.

One possibility for piezoelectric ceramics to integrate in biological applications, is as sensors in bones. However, experiments shown in this thesis indicate a strong chemical reaction between $(Na_{0.465}K_{0.465}Li_{0.07})NbO_3$ and the main mineral of the bone, hydroxyapatite. Even though piezoelectric response could be detected by PFM, it is still to be confirmed that the chemical products of the reaction are biocompatible as well.

Outlook

The study of lead free piezoelectrics is far from being exhausted. The search for piezoelectric systems, which could replace PZT in the different applications, is not restricted to the two systems suggested in this thesis. However, these are the most studied and promising ones. Still, some open issues have been identified in the course of this thesis work:

- Even though some clues regarding the nature of the polar phases in the phase diagram of bismuth sodium barium titanate have been revealed, the nature of the non polar phases is still not clear (antiferroelectric or paraelectric phases). In addition, an ongoing study on bismuth sodium titanate-bismuth potassium titanate-potasium sodium niobate has recently shown interesting results of piezoelectric response at temperatures above Tm in which the polar phase is considered not to exist. Understanding these issues is of high scientific interest.
- This thesis revealed that lead free piezoelectrics can exhibit a nearly vertical morphotropic phase boundary (MPB), but although a peak in the properties is observed in the proximity of this boundary in the lead free systems, it is still

not as high as found in PZT. It is possible that the difference in the number of phase boundaries in the MPB region is responsible for the difference in properties, however this is not yet clear. Hence the question whether the lead cation is essential for large piezoelectricity, remains unanswered.

- Reproducibility problems during the processing of potassium sodium lithium niobate were solved in this thesis, however piezoelectric properties were measured to be lower then the published ones. The cause for this might be sensitivity during processing of the powders to atmosphere or humidity. Careful investigation of processing conditions may result in higher properties and thus be of great interest for applications.
- Potassium sodium lithium niobate phase diagram exhibits a triple phase intersection around zero degree C and a morphotropic phase boundary at even lower temperatures. These phase boundaries may imply high piezoelectric properties, however, the low temperature at which they appear strongly reduce their possible applications. Hence shifting these phase transitions to more convenient temperatures by chemical doping, applied pressure or other means, could lead to practically interesting materials.
- Piezoelectric implants in bones and other organs could be used for medical diagnostics and treatment. The preliminary results of this thesis indicate that KNLN is biocompatible. However, biocompatibility of lead free materials and possible chemical reactions in the complex conditions of the body should be thoroughly investigated.

Bibliography

1. Setter, N. E., *Piezoelectric material in devices*. 2002.
2. Jaffe, B.; Cook, W. R.; Jaffe, J. H., *Piezoelectric Ceramics*. Academic press: 1971; chapter 8.
3. "Safety data sheet, Lead (II) oxide".
4. "Safety data sheet, Lead zirconium titanium oxide sputtering target".
5. "Safety data sheets, Lead coarse powder GR for analysis".
6. "EU-Directive 2002/95/EC: Restriction of the use of certain hazardous substances in electrical and electronic equipment (RoHS)". *Official J. European Union* **2003,** 46, (L37), 19-23.
7. "EU-Directive 2002/96/EC: Waste electrical and electronic equipment (WEEE)". *Official J. European Union* **2003,** 46, (L37), 24-38.
8. Glazer, A. M., Simple ways of determining perovskite structure. *Acta Cryst. A* **1975,** 31, 756-762.
9. Cohen, R. E., Origin of ferroelectricity in perovskite oxides. *Nature* **1992,** 358, 136-138.
10. Birkholz, M., Crystal-field induced dipoles in heteropolar crystals II: physical significance. *Z. Phys. B* **1995,** 96, 333-340.
11. Jaffe, B.; Roth, R. S.; Marzullo, S., Piezoelectric properties of lead zirconate - lead titanat solide-solution ceramics. *J. Appl. Phys.* **1954,** 25, 809-810.
12. Noheda, B.; Cox, D. E.; Shirane, G.; Gonzalo, J. A.; Cross, L. E.; Park, S.-E., A monoclinic ferroelectric phase in the Pb(Zr1-xTix)O3 solid solution. *Appl. Phys. Lett.* **1999,** 74, (14), 2059-2061.
13. Noheda, B.; Cox, D. E., Bridging phases at the morphotropic boundaries of lead oxide solid solutions. *Phase Transitions* **2006,** 79, (1), 5-20.
14. Guo, R.; Cross, L. E.; Park, S.-E.; Noheda, B.; Cox, D. E.; Shirane, G., Origin of the High Piezoelectric Response in PbZr1-*x*Ti*x*O3. *Phys. Rev. Lett.* **2000,** 84, (23), 5423-5426.
15. Noheda, B., Structure and high-piezoelectricity in lead oxide solid solutions. *Current Opinion Solid State Mater. Sci.* **2002,** 6, 27-34.

16. Ishibashi, Y.; Iwata, M., A theory of morphotropic phase boundary in solid-solution systems of perovskite-type oxide ferroelectrics. *Jap. J. Appl. Phys.* **1999,** 38, 800-804.
17. Damjanovic, D., Contributions to the Piezoelectric Effect in Ferroelectric Single Crystals and Ceramics. *J. Am. Ceram. Soc.* **2005,** 88, 2663-2676.
18. Haun, M. J.; Furman , E.; Jang, S. J.; Cross, L. E., Thermodynamic theory of the lead zirconate-titanate solid solution system, Part V: Theoretical calculations. *Ferroelectrics* **1989,** 99, 63-86.
19. Budimir, M.; Damjanovic, D.; Setter , N., Piezoelectric response and free-energy instability in the perovskite crystals BaTiO3, PbTiO3, and (Pb,,Zr)TiO3 *Phys. Rev. B* **2006,** 73, 174106.
20. Singh, A. K.; Mishra, S. K.; Ragini, D.; Pandey, D.; Yoon, S.; Baik , S.; Shin, N., Origin of high piezoelectric response of Pb(ZrxTi1−x)O3 at the morphotropic phase boundary: Role of elastic instability *Appl. Phys. Lett.* **2008,** 92, 022910.
21. Habal, R., Toxicity, Lead. *emedicin:* *http://www.emedicine.com/MED/topic1269.htm* **2008**.
22. SAKAI, T.; HOSHIAI, S.; NAKAMACHI, E., Biochemical compatibility of PZT piezoelectric ceramics covered with titanium thin film. *J. Optoelec. Adv. Mater.* **2006,** 8, (4), 1435-1437.
23. Hill, N. A.; Rabe, K. M., First-principles investigation of ferromagnetism and ferroelectricity in bismuth manganite. *Phys. Rev. B* **1999,** 59, (13), 8759-8769.
24. Brown, R. D., Bismuth. In *Minerals Yearbook, Vol 1. Materials & Minerals*, http://minerals.usgs.gov/minerals/pubs/commodity/bismuth/110496.pdf.
25. Rodilla, V.; Miles, A. T.; Jenner, W.; Hawksworth, G. M., Exposure of cultured human proximal tubular cells to cadmium, mercury, zinc and bismuth: toxicity and metallothionein induction. *Chem.-Biol. Interac* **1998,** 115, 71-83.
26. Sano, Y.; Satoh, H.; Chiba, M.; Okamoto, M.; Serizawa, K.; Nakashima, H.; Omae, K., Oral toxicity of bismuth in rat: single and 28-day repeated administration studies. *J. Occup. Health* **2005,** 47, 293-298.
27. Xu, Q.; Chen, X.; Chen, W.; Chen, S.; Kim, B.; Lee, J., Synthesis, ferroelectric and piezoelectric properties of some (Na0.5Bi0.5)TiO3 system compositions. *Mater. Lett.* **2005,** 59, (19-20), 2437-2441.

28. Takenaka, T.; Maruyama, K.-i.; Sakata, K., (Bi1/2Na1/2)TiO3-BaTiO3 System for Lead-Free Piezoelectric Ceramics. *Jap. J. Appl. Phys* **1991,** 30, (9B), 2236-2239.
29. Hiruma, Y.; Nagata, H.; Takenaka, T., Phase diagrams and electrical properties of (Bi1/2Na1/2)TiO3-based solid solutions. *J. Appl. Phys.* **2008,** 104, 124106.
30. Zhang, S.-T.; Kounga, A. B.; Aulbach, E.; Deng, Y., Temperature-Dependent Electrical Properties of 0.94Bi0.5Na0.5TiO3–0.06BaTiO3 Ceramics. *J. Am. Ceram. Soc.* **2008**, 1-5.
31. Fang, Z.; Yue-ying, X.; De-ju, L.; Chong-tan, H.; Min, G.; Tian-bao, W., X-Ray study on the crystallographic characterization of ferroelectric ceramics: (Na0.5Bi0.5)TiO3 and its solid solution system. *Acta Phys. Sinica* **1989,** 38, (8), 1348-1353.
32. Chu, B.-J.; Chen, D.-R.; Li, G.-R.; Yin, Q.-R., Electrical properties of Na1/2Bi1/2TiO3–BaTiO3 ceramics. *J. Eur. Ceram. Soc.* **2002,** 22, (13), 2115-2121.
33. Sakata, K.; Masuda, Y., Ferroelectric and antiferroelectric properties of (Na0.5Bi0.5)TiO3-SrTiO3 solid solution ceramics. *Ferroelectrics* **1974,** 7, 347-349.
34. Zvirgzds, J. A.; Kapostins, P. P.; Zvirgzde, J. V., X-Ray study of phase transitions in ferroelectric Na0.5Bi0.5TiO3. *Ferroelectrics* **1982,** 40, 75-77.
35. Pronin, I. P.; Syrnikov, P. P.; Isupov, V. A.; Egorov, V. M.; Zaitseva, N. V., Peculiarities of phase transitions in sodium-bismuth titanate. *Ferroelectrics* **1980,** 25, 395-397.
36. Kittel, C., Theory of Antiferroelectirc crystals. *Phys. Rev.* **1951,** 82, (5), 729-732.
37. Vakhrushev, S. B.; Isupov, V. A.; Kvyatkovsky, B. E.; Okuneva, N. M.; Pronin, I. P.; Smolensky, G. A.; Syrnikov, P. P., Phase transitions and soft modes in sodium bismouth titanate. *Ferroelectrics* **1985,** 63, 153-160.
38. Zhang, M.-S.; Scott, J. F., Raman spectroscopy of Na0.5Bi0.5TiO3. *Ferroelectrics* **1986,** 6, 147-152.
39. Suchanicz, J.; Roleder, K.; Kania, A.; Handerek, J., Elecrostrictive strain and pyroeffect in the region of phase coexistence in Na0.5Bi0.5TiO3. *Ferroelectrics* **1988,** 77, 107-110.

40. Roleder, K.; Suchanicz, J.; Kania, A., Time dependence of electric permittivity in Na0.5Bi0.5TiO3 single crystals. *Ferroelectrics* **1989,** 89, 1-5.
41. Shirane, G.; Newnham, R.; Pepinsky, R., Dielectric properties and phase transition of NaNbO3 and (Na,K)NbO3. *Phys. Rev.* **1954,** 96, (3), 581-588.
42. Tennery, V. J.; Hang, K. W., Thermal and X-rey diffraction studies of the NaNbO3-KNbO3 system. *J. Appl. Phys.* **1968,** 39, (10), 4749-4753.
43. Ahtee, M., Phase transitions in sodium niobate potasium niobate solid solutions. *Ferroelectrics* **1974,** 7, 93-95.
44. Tellier, J.; Malic, B.; Dakhil, B.; Jenko, D.; Cilensek, J.; Kosec, M., Crystal structure and phase transitions of sodium potassium niobate perovskites *Solid State Sci.* **2009,** 11, 320-324.
45. Shiratori, Y.; Magrez, A.; Pithan, C., Particle size effect on the crystal structure symmetry of K0.5Na0.5NbO3. *J. Eur. Ceram. Soc.* **2005,** 25, (12), 2075-2079.
46. Baker, D. W.; Thomas, P. A.; Zhangb, N.; Glazerb, A. M., Structural study of KxNa1-xNbO3 (KNN) for compositions in the range x = 0.24–0.36. *Acta Cryst.* **2009,** B65, 22-28.
47. Attia, J.; Bellaiche, L.; Gemeiner, P.; Dkhil, B.; Malic, B., Study of potassium sodium niobate alloys: A combined experimental and theoretical approch. *J. Phys. IV* **2005,** 128, (55-60).
48. Trodahl, H. J.; Klein, N.; Damjanovic, D.; Setter , N.; Ludbrook, B.; Rytz, D.; Kuball, M., Raman spectroscopy of (K,Na)NbO3 and (K,Na)1−xLixNbO3. *Appl. Phys. Lett.* **2008,** 93, 262901.
49. Cho, D. H.; Ryu, M. K.; Park, S. S.; Cho, S. Y.; Choi, J. G.; Jang, M. S.; Kim, J. P.; Cho, C. R., A study of ferroelectric properties in NaxK1-xNbO3 ceramic compounds. *J. Korean Phys. Soc.* **2005,** 46, (1), 151-154.
50. Birol, H.; Damjanovic, D.; Setter, N., preparation and characterization of KNbO3 ceramics. *J. Am. Ceram. Soc.* **2005,** 88, (7), 1754-1749.
51. Du, H.; Li, Z.; Tang, F.; Qu, S.; Pei, Z.; Zhou, W., Preparation and piezoelectric properties of $(K_{0.5}Na_{0.5})NbO_3$ lead-free piezoelectric ceramics with pressure-less sintering. *Mater. Sci. Eng. B* **2006,** 131, (1-3), 83-87.
52. Ringgaard, E.; Wurlitzer, T., Lead-free piezoceramics based on alkali niobates *J. Eur. Ceram. Soc.* **2005,** 25, 2701-2706.

53. Singh, K.; Lingwal, V.; Bhatt, S. C.; Panwar, N. S.; Semwal, B. S., Dielectric properties of potassium sodium niobate mixed system. *Mater. Res. Bull.* **2001,** 36, (13-14), 2365-2374.
54. Kosec, M.; Kolar, D., On activated sintering and electrical properties of NaKNbO3. *Mat. Res. Bull.* **1975,** 10, 335-340.
55. Jaeger, R. E.; Egerton, L., Hot pressing of potassium-sodium niobates. *J. Am. Ceram. Soc.* **1962,** 45, (5), 209-213.
56. Haerling, G. H., Properties of hot-pressed ferroelectric alkali niobate ceramics. *J. Am. Ceram. Soc.* **1967,** 50, (6), 329-330.
57. Egerton, L.; Dillon, D. M., Piezoelectric and dielectric properties of ceramics in the system potassium-sodium niobate. *J. Am. Cearm. Soc* **1959,** 42, (9), 438-442.
58. Turik, A. V.; Tais'eva, V. A.; Raevskii, I. P.; Reznichenko, L. A.; Prokopalo, O. I., Dielectric properties of hot-pressed (K,N)NbO3 ceramic. *Izv Akad Nauk SSSR Neorg Mater* **1978,** 14, (5), 912-914.
59. Saito, Y.; Takao, H.; Tani, T.; Nonoyama, T.; Takatori, K.; Homma, T.; Nagaya, T.; Nakamura, M., Lead-free piezoceramics. *Nature* **2004,** 432, (7013), 84-87.
60. Guo, Y.; Kakimoto, K. I.; Ohsato, H., Phase transitional behavior and piezoelectric properties of (Na0.5K0.5)NbO3–LiNbO3 ceramics. *Appl. Phys. Lett.* **2004,** 85, (18), 4121-4123.
61. Liu, D.; Du, H.; Tang, F.; Luo, F.; Zhu, D.; Zhou , W., Effect of heating rate on the structure evolution of (K0.5Na0.5) NbO3–LiNbO3 lead-free piezoelectric ceramics. *J. Electroceramics* **2008,** 20, (2), 107-111.
62. Tang, F.-S.; Du, H.-T.; Li, Z.-M.; Zhou, W.-C.; Qu, S.-B.; Pei, Z.-B., Preparation and properties of (K0.5Na0.5)NbO3-LiNbO3 ceramics. *Trans. Nonferrous. Met. Soc. China* **2006,** 16, (supp), 466-469.
63. Du, H.; Tang, F.; Luo, F.; Zhu, D.; Qu, S.; Pei, Z.; Zhou , W., Influence of sintering temperature on piezoelectric properties of (KNa)NbO3–LiNbO3 lead-free piezoelectric ceramics. *Mater. Res. Bull.* **2007,** 42, (9), 1594.
64. Du, H.; Tang, F.; Luoa, F.; Zhoua, W.; Qub, S.; Pei, Z., Effect of poling condition on piezoelectric properties of (K0.5Na0.5)NbO3–LiNbO3 lead-free piezoelectric ceramics. *Mater. Sci. Eng. B* **2007,** 137, 175-179.

65. Du, H.; Zhou, W.; Luo, F.; Zhu, D.; Qu, S.; Pei, Z., An approach to further improve piezoelectric properties of (K0.5Na0.5)NbO3-based lead-free ceramics. *Appl. Phys. Lett.* **2007,** 91, 202907.
66. Wang, K.; Li, J.-F., Analysis of crystallographic evolution in (Na,K)NbO3-based lead-free piezoceramics by x-ray diffraction. *Appl. Phys. Lett.* **2007,** 91, 262902.
67. Zhao, P.; Zhang, B.-P.; Li, J.-F., High piezoelectric d33 coefficient in Li-modified lead-free (Na,K)NbO3 ceramics sintered at optimal temperature. *Appl. Phys. Lett.* **2007,** 90, 242909.
68. Song, H.-C.; Cho, K.-H.; Park, H.-Y.; Ahn, C.-W.; Nahmw, S.; Uchino, K.; Park, S.-H.; Lee, H.-G., Microstructure and Piezoelectric Properties of (1-x)(Na0.5K0.5)NbO3–xLiNbO3 Ceramics. *J. Am. Ceram. Soc.* **2007,** 90, (6), 1812-1816.
69. Zhen, Y.; Li, J.-F., Normal Sintering of (K,Na)NbO3-Based Ceramics: Influence of Sintering Temperature on Densification, Microstructure, and Electrical Properties. *J. Am. Ceram. Soc.* **2006,** 89, (12), 3669-3675.
70. Niu, X. K.; Zhang, J. L.; Wu, L.; Zheng, P.; Zhao, M. L.; Wang, C. L., Crystalline structural phase boundaries in (K,Na,Li)NbO3 ceramics. *Solid State Commun.* **2008,** 146, 395-398.
71. Hollenstein, E.; Davis, M.; Damjanovic, D.; Setter, N., Piezoelectric properties of Li- and Ta-modified $(K_{0.5}Na_{0.5})NbO_3$ ceramics. *Appl. Phys. Lett.* **2005,** 87, 182905.
72. Marino, A. A.; Becker, R. O., Piezoelectricity in Bone as a Function of Age. *Calc. Tiss. Res.* **1974,** 14, 327-331.
73. Marino, A. A.; Becker, R. O.; Soderholm, S. C., Origin of the piezoelectric effect in bone. *Calc. Tiss. Res.* **1971,** 8, 177-180.
74. Bassett, C. A. L.; Becker, R. O., Generation of electric potentials by bone in response to mechanical stress. *Science* **1962,** 137, 1063-1064.
75. Fukada, E.; Yasuda, I., On the piezoelectric effect of bone. *J. Phys. Soc. Japan* **1957,** 12, (10), 1158-1162.
76. Ghosh, S.; Z. Mei, B.; Lubkin, V.; Scheinbeim, J. I.; Newman, B. A.; Kramer, P.; Bennett, G.; Feit, N., Piezoelectric response of scleral collagen. *J. Biomed. Mat. Res. B* **1998,** 39, 453-457.

77. Lang, S. B.; Marino, A. A.; Berkovic, G.; Fowler, M.; Abreo, K. D., Piezoelectricity in the human pineal gland *Bioelectrochemistry and Bioenergetics* **1996,** 41, 191-195.
78. Wang, T.; Feng, Z.; Song, Y.; Chen, X., Piezoelectric properties of human dentin and some influencing factors. *Dental Mater.* **2007,** 23, 450-453.
79. Coleman, N. J.; Nicholson, J. W., Glass Bones. *http://www.rsc.org/Education/EiC/issues/2006Nov/GlassBones.asp* **2006**.
80. health, U. S. n. c. i. o., Structure of bone tissue. In.
81. Watson, J., The Electrical Stimulation of Bone Healing. *Proc. IEEE* **1979,** 67, (10), 1339-1352.
82. Tofail, S. A. M.; Haverty, D.; Cox, F.; Erhart, J.; Hána, P.; Ryzhenko, V., Direct and ultrasonic measurements of macroscopic piezoelectricity in sintered hydroxyapatite. *J. Appl. Phys.* **2009,** 105, 064103.
83. Bassett, L. A. C.; Pawluk, R. J.; Becker, R. O., Effects of electric currents on bone in vivo. *Nature* **1964,** 204, 652-654.
84. Friedenberg, Z. B.; Roberts, P. G.; Didizian, J., N. H. ; Brighton, C. T., Stimulation of Fracture Healing by Direct Current in the Rabbit Fibula. *J. Bone Joint Surg.* **1971,** 53-A, (7), 1400-1408.
85. Nakamura, S.; Takeda, H.; Yamashita, K., Proton transport polarization and depolarization of hydroxyapatite ceramics. *J. Appl. Phys.* **2001,** 89, (10), 5386-5392.
86. Kobayashi, T.; Nakamura, S.; Yamashita, K., Enhanced osteobonding by negative surface charges of electrically polarized hydroxyapatite. *J. Biomed. Mat. Res.* **2001,** 57, (4), 447-484.
87. Teng, N. C.; Nakamura, S.; Takagi, Y.; Yamashita, Y.; Ohgaki , M.; Yamashita, K., A new approach to enhancement of bone formation by electrically polarized hydroxya patite. *J. Dent. Res.* **2001,** 80, (1), 1925-1929.
88. Yamashita, K.; Oikawa, N.; Umegaki, T., Acceleration and Deceleration of Bone-Like Crystal Growth on Ceramic Hydroxyapatite by Electric Poling. *Chem. Mater.* **1996,** 8, 2697-2700.
89. Itoh, S.; Nakamura, S.; Kobayashi, T.; Shinomiya, K.; Yamashita, K., The effects of electrically polarized hydroxyapatite on osteogenic cell activity and bone formation. *Key Eng. Mater.* **2006,** 309-311, 153-156.

90. Itoh, S.; Nakamura, S.; Nakamurab, M.; Shinomiya, K.; Yamashita, K., Enhanced bone ingrowth into hydroxyapatite with interconnected pores by Electrical Polarization. *Biomaterials* **2006,** 27, 5572-5579.
91. Vallet-Regi, M.; Gonzalez-Calbet, J. M., Calcium phosphates as substitution of bone tissues. *Prog. Solid. Chem.* **2004,** 32, 1-31.
92. Furuzono, T.; Walsh, D.; Yasuda, S.; Sato, K.; Tanaka, J.; Kishida, A., Preparation of plated β-tricalcium phosphate containing hydroxyapatite for use in bonded inorganic-organic composites. *J. Mater. Sci.* **2005,** 40, 2595-2597.
93. Monroe, E. A.; Votava, w.; Bass, D. B.; Mcmullen, J., New Calcium Phosphate Ceramic Material for Bone and Tooth Implants *J. Dent. Res.* **1971,** 50, 860-861.
94. Mahabole, M. P.; Aiyer, R. C.; Ramakrishna, C. V.; Sreedhar, B.; Khairnar, R. S., Synthesis, characterization and gas sensing property of hydroxyapatite ceramic. *Bull. Mater. Sci.* **2005,** 28, (6), 535-545.
95. Jarcho, M.; Bolen, C. H.; Thomas, M. B.; Bobick, J.; Key, J. F.; Doremus, R. H., Hydroxylapatite synthesis and characterization in dense polycrystalline form. *J. Mater. Sci.* **1976,** 11, 2027-2035.
96. Feng, J.; Shao, Q.; Weng, J.; Li, Y.; Li, J.; Zhang, X., An investigation on the ceramic composite of the biological piezoelectric implants. *Polymers and Biomater.* **1991**, 367-371.
97. Feng, J.; Yuan, H.; Zhang, X., Promotion of osteogenesis by a piezoelectric biological ceramic. *Biomaterials* **1997,** 18, 1531-1534.
98. Bowen, C. R.; Gittings, J.; Turner, I. G.; Baxter, F.; Chaudhuri , J. B., Dielectric and piezoelectric properties of hydroxyapatite-BaTiO3 composites. *Appl. Phys. Lett.* **2006,** 89, 132906.
99. Gittings, J. P.; Bowen, C. R.; Turner, I. G.; Baxter, F.; Chaudhuri, J., Characterisation of ferroelectric-calcium phosphate composites and ceramics. *J. Eur. Ceram. Soc.* **2007,** 27, 4187-4190.
100. Aba, A.; Ergun, C., Phase Stability in Hydroxyapatite / Barium Titanate Piezo Bioceramics. *Defect and Diffusion Forum* **2008,** 273-276, 1-7.
101. Damjanovic, D., Ferroelectric, dielectric and piezoelectric properties of ferroelectric thin films and ceramics. *Reports on Progress in Physics* **1998,** 61, (9), 1267.

102. Krupka, J.; Zychowicz, T.; Bovtun, V.; Veljko, S., Complex Permittivity Measurements of Ferroelectrics Employing Composite Dielectric Resonator Technique *IEEE Trans. Ultra. Ferro. Freq. Control* **2006,** 53, (10), 1883-1888.
103. Barzegar, A.; Damjanovic, D.; Setter, N., Analytical Modeling of the Apparent d33 Piezoelectric Coefficient Determined by the Direct Quasistatic Method for Different Boundary Conditions. *IEEE Trans. Ultra. Ferro. Freq. Control* **2005,** 52, (11), 1897-1903.
104. Barzegar, A. F.; Damjanovic, D.; Setter, N., The effect of boundary conditions and sample aspect ratio on apparent d33 piezoelectric coefficient determined by direct quasistatic method. *IEEE Trans. Ultra. Ferro. Freq. Control* **2004,** 51, (3), 262-270.
105. Schrader, B. E., *Infrafed and Raman spectroscopy*. 1995.
106. Bowley, H. J.; Gardiner, D. J.; Gerrard, D. L.; Graves, P. R.; Louden, J. D.; Turrell, G., *Practical Raman spectroscopy*. 1989.
107. Cullity, B. D., *Elements of X-Ray diffraction*. second edition ed.; 1978.
108. Hong, S.; Woo, J.; Shin, H.; Jeon, J. U.; Pak, Y. E.; Colla, E. L.; Setter, N.; Kim, E.; No, K., Principle of ferroelectric domain imaging using atomic force microscope. *J. Appl. Phys.* **2001,** 89, (2), 1377-1386.
109. Jarvis, K. E.; Williams, J. G., Laser ablation inductively coupled plasma mass spectrometry (LA-ICP-MS): a rapid technique for the direct, quantitative determination of major, trace and rare-earth elements in geological samples. *Chem. Geo.* **1993,** 106, 251-262.
110. Denoyer, E. R.; Fredeen, K. J.; Hager, J. W., Laser solid sampling for inductively coupled plasma mass spectrometry. *Analy. Chem* **1991,** 63, (8), 445-457.
111. Longerich, H. P.; Jackson, S. E.; Fryer, B. J.; Strong, D. F., The laser ablation microprobe-inductively coupled plasma mass spectromoeter. *Geosci. Canada* **1993,** 20, (1), 21-27.
112. Xu, C.; Lin, D.; Kwok, K. W., Structure, electrical properties and depolarization temperature of (Bi0.5Na0.5)TiO3eBaTiO3 lead-free piezoelectric ceramics. *Solid State Sci.* **2008,** 10, 934-940.
113. McNeal, M. P.; Jang, S.-J.; Newnham, R. E., The effect of grain and particle size on the microwave properties of barium titanate (BaTiO3) *J. Appl. Phys.* **1998,** 83, (6), 3288-3297.

114. Suchanicz, J., Behaviour of Na0.5Bi0.5TiO3 ceramics in the A.C. electric field. *Ferroelectrics* **1998,** 209, 561-568.
115. Robert, G.; Demartin, M.; Damjanovic, D., Phase Diagram for the 0.4Pb(Ni1/3,Nb1/3)O3–0.6Pb(Zr,Ti)O3 Solid Solution in the Vicinity of a Morphotropic Phase Boundary. *J. Am. Ceram. Soc.* **1998,** 81, (3), 749-753.
116. Setter, N.; Cross, E., The role of B-site cation disorder in diffuse phase transition behavior of perovskite ferroelectrics. *J. Appl. Phys.* **1980,** 51, (8), 4356-4360.
117. Tu, C.-S.; Siny, I. G.; Schmidt, V. H., Sequemce of dielectric anomalies and high-temperature relaxation behavior in Na1/2Bi1/2TiO3. *Phys. Rev. B* **1994,** 49, (17), 11550-11559.
118. Wang, X. X.; Or, S. W.; Tang, X. G.; Chan, H. L. W.; Choy, P. K.; Liu, P. C. K., TiO2-nonstoichiometry dependence on piezoelectric properties and depolarization temperature of (Bi0.5Na0.5)0.94Ba0.06TiO3 lead-free ceramics *Solid State Commun.* **2005,** 134, 659-663.
119. Wang, X. X.; Kwok, K. W.; Tang, X. G.; Chan, H. L. W.; Choy, C. L., Electromechanical properties and dielectric behavior of (Bi1/2Na1/2)(1-1.5x)BixTiO3 lead-free piezoelectric ceramics. *Solid State Commun.* **2004,** 129, 319-323.
120. Hiruma, Y.; Nagata, H.; Takenaka, T., Phase Transition Temperatures and Piezoelectric Properties of (Bi1/2 Na1/2)TiO3 –(Bi1/2 K1/2)TiO3 –BaTiO3 Lead-Free Piezoelectric Ceramics *Jap. J. Appl. Phys* **2006,** 45, (9B), 7409-7412.
121. Hiruma, Y.; Yoshii, K.; Nagata, H.; Takenaka, T., Investigation of Phase Transition Temperatures on (Bi1/2Na1/2)TiO3-(Bi1/2K1/2)TiO3 and (Bi1/2Na1/2)TiO3-BaTiO3 Lead-free Piezoelectric Ceramics by Electrical Measurements. *Ferroelectrics* **2007,** 346, 114-119.
122. Zhou, C.-R.; Liu, X.-Y., Piezoelectric properties and dielectric behavior of Bi1/2Na1/2[Ti1−x(Sb1/2Nb1/2)x]O3 lead-free piezoelectric ceramics. *J. Electroceramics* **2007,** 19, 237-240.
123. Xu, G.; Duan, Z.; Wang, X.; Yang, D., Growth and some electrical properties of lead-free piezoelectric crystals (Na1/2Bi1/2)TiO3 and (Na1/2Bi1/2)TiO3–BaTiO3 prepared by a Bridgman method. *J. Crys. Grow.* **2005,** 275, 113-119.
124. Suchanicz, J., Investigations of the phase transitions in Na0.5Bi0.5TiO3 *Ferroelectrics* **1995,** 172, 455-458.

125. Zhao, M.-L.; Zhong, W.-L.; Wang, C.-L.; Wang, J.-F.; Zhang, P.-L., Investigation of phase transition in (Ba0.5Na0.5)TiO3 based materials. *Acta Phys. Sinica* **2002,** 51, (8), 1856-1869.
126. Arlt, G.; Bottger, U.; Witte, S., Dielectric dispersion of ferroelectric ceramics and single crystals at microwave frequencies. *Ann. Physik* **1994,** 3, 578-588.
127. Kittel, C., Domain boundary motion in ferroelectric crystals and the dielectric constant at high frequency. *Phys. Rev.* **1951,** 83, (458).
128. Pertsev, N. A.; Arlt, G., Forced translational vibrations of 90" domain walls and the dielectric dispersion in ferroelectric ceramics *J. Appl. Phys.* **1993,** 74, 4105-4111.
129. Arlt, G.; Bottger, U.; Witte, S., Emission of GHz shear waves by ferroelastic domain walls in ferroelectrics *Appl. Phys. Lett.* **1993,** 63, (602-604).
130. Xi, Y.; McKinstry, H.; Cross, L. E., The Influence of Piezoelectric Grain Resonance on the Dielectric Spectra of LiNbO3 Ceramics. *J. Am. Ceram. Soc.* **1983,** 637-641.
131. Damjanovic, D.; Demartin, M., Contribution of the irreversible displacement of domain walls to the piezoelectric effect in barium titanate and lead zirconate titanate ceramics. *J. Phys: Cond. Matter* **1997,** 9, 4943-4953.
132. Maglione, M.; Bohmer, R.; Loidl, A.; Hochli, U. T., Polar relaxation in pure and iron-doped barium titanate. *Phys. Rev. B* **1989,** 40, (16), 11441.
133. Roleder, K.; Franke, I.; Glazer, A. M.; Thomas, P. A.; Miga, S.; Suchanicz, J., The piezoelectric effect in Na05Bi05TiO3 ceramics. *J. Phys. Cond. Matter* **2002,** 14, 5399-5406.
134. Jones, G. O.; Thomas, P. A., Investigation of the structure and phase transitions in the novel A-site substituted distorted perovskite compound Na1/2Bi1/2TiO3. *Acta Cryst. B. Struct. Sci.* **2002,** 58, 168-178.
135. Zhang, M.-S.; Scott, F., Raman Spectroscopy of Na0.5Bi0.5TiO3. *Ferroelectrics Lett.* **1986,** 6, 147-152.
136. Kreisel, J.; Glazer, A. M.; Jones, G.; Thomas, P. A.; Abello, L.; Lucazeau, G., An x-ray diffraction and Raman spectroscopy investigation of A-site substituted perovskite compounds: the (Na1−xKx)0.5 Bi0.5 TiO3 (0<. *J. Phys: Cond. Matter* **2000,** 12, 3267-3280.

137. Dorcet, V.; Trolliard, G.; Boullay, P., Reinvestigation of Phase Transitions in Na0.5Bi0.5TiO3 by TEM. Part I: First Order Rhombohedral to Orthorhombic Phase Transition. *Chem. Mater.* **2008,** 20, 5061-5073.
138. Trolliard, G.; Dorcet, V., Reinvestigation of Phase Transitions in Na0.5Bi0.5TiO3 by TEM. Part II: Second Order Orthorhombic to Tetragonal Phase Transition. *Chem. Mater.* **2008,** 20, 5074-5082.
139. Fukuda, T.; Hirano, H.; Uematsu, Y.; Ito, T., Dielectric Constant of Orthorhombic KNbO3 Single Domain Crystal. *Jap. J. Appl. Phys* **1974,** 13, 1021-1022.
140. Higashide, K.; Kakimoto, K.-i.; Ohsato, H., Temperature dependence on the piezoelectric property of (1-x)(Na0.5K0.5)NbO3–xLiNbO3 ceramics. *J. Eur. Ceram. Soc.* **2007,** 27, 4107-4110.
141. Hollenstein, E. preparation and properties of KNbO3-based piezoelectric ceramics. EPFL, Lausanne, 2007.
142. Hagh, N. M.; Jadidian, B.; Safari , A., Property-processing relationship in lead-free (K, Na, Li)NbO3-solid solution system. *J. Electroceramics* **2007,** 18, 339-346.
143. Wang, Y.; Damjanovic, D.; Klein, N.; Hollenstein, E.; Setter, N., Compositional Inhomogeneity in Li- and Ta-Modified (K, Na)NbO3 Ceramics. *J. Am. Ceram. Soc.* **2007,** 1–5.
144. Li, J.-F.; Zhen, Y.; Zhang, B.-P.; Zhang, L.-M.; Wang, K., Normal sintering of (K, Na)NbO3-based lead-free piezoelectric ceramics. *Ceram. Intern.* **2008,** 34, 783-786.
145. Shigemi, A.; Wada, T., Evaluations of Phases and Vacancy Formation Energies in KNbO3 by First-Principles Calculation. *Jap. J. Appl. Phys* **2005,** 44, (11), 8048-8054.
146. Shigemi, A.; Wada, T., Enthalpy of Formation of Various Phases and Formation Energy of Point Defects in Perovskite-Type NaNbO3 by First-Principles Calculation. *Jap. J. Appl. Phys* **2004,** 43, (9B), 6793-6798.
147. Saito, Y.; Takao, H., High preformance lead free piezoelectric ceramics in the (K,Na)NbO3-LiTaO3 solid solution system. *Ferroelectrics* **2006,** 338, (17-32).
148. Noheda, B., Structure and high-piezoelectricity in lead oxide solid solutions. *Current Opinion Solid State Mater. Sci.* **2002,** 6, (1), 27-34.

149. Chu, S.-Y.; Water, W.; Juang, Y.-D.; Liaw, J.-T., Properties of (Na,K)NbO3 and (Li,Na,K)NbO3 ceramic mixed systems. *Ferroelectrics* **2003,** 287, 23-33.
150. Kakimoto, K.; Akao, K.; Guo, Y.; Ohsato, H., Raman Scattering Study of Piezoelectric (Na0:5K0:5)NbO3-LiNbO3 Ceramics. *Jap. J. Appl. Phys* **2005,** 44, (9B), 7064-7067.
151. Matsubara, M.; Yamaguchi, T.; Kikuta, K.; Hirano, S. I., Effect of Li Substitution on the Piezoelectric Properties of Potassium Sodium Niobate Ceramics. *Jap. J. Appl. Phys* **2005,** 44, (8), 6136-6142.
152. Hewat, A. W., Cubic-tetragonal-orthorhombic-rhombohedral ferroelectric transitions in perovskite potassium niobate : neutron powder profile refinement of the structures. *J. Phys. C: Solid State Phys.* **1973,** 6, 2559-2572.
153. Ahtee, M.; Glazer, A. M., Lattice parameters and tilted octahedra in sodium-potassium niobate solid solutions. *Acta Cryst. A* **1976,** 32, 434-446.
154. Baier-Saip, J. A.; Ramos-Moor, E.; Cabrera, A. L., Raman study of phase transitions in KNbO3. *Solid State Commun.* **2005,** 135, 367-372.
155. Rouquette, J.; Haines, J.; Bornand, V.; Pintard, M.; Papet, P.; Astier, R.; Leger, J. M.; Gorelli, F., Transition to a cubic phase with symmetry-breaking disorder in PbZr_{0.52}Ti_{0.48}O_{3} at high pressure. *Phys. Rev. B* **2002,** 65, (21), 214102.
156. Stokes, H. T.; Kisi, E. H.; Hatch, D. M.; Howardc, C. J., Group-theoretical analysis of octahedral tilting in ferroelectric perovskites. *Acta Cryst.* **2002,** B58, 934-938.
157. Howard, C. J.; Stokes, H. T., Structures and phase transitions in perovskites - a group theoretical approach. *Acta Cryst.* **2005,** A61, 93-111.
158. Bilc, D. I.; Singh, D. J., Frustration of Tilts and *A*-Site Driven Ferroelectricity in KNbO3-LiNbO3 Alloys. *Phys. Rev. Lett.* **2006,** 96, 147602.
159. Glazer, A., The classification of tilted octahedra in perovskites. *Acta Cryst. Section B* **1972,** 28, (11 %R doi:10.1107/S0567740872007976), 3384-3392.
160. Berlincourt, D.; Krueger, H. H. A.; Jaffe, B., Stability of phases in modified lead zirconate with variation in pressure, electric field, temperature and composition. *J. Phys. Chem. Solids* **1964,** 25, (7), 659-674.
161. Cross, L. E.; Fouskova, A.; Cummins, S. E., Gadolinium Molybdate, a New Type of Ferroelectric Crystal. *Phys. Rev. Lett.* **1968,** 21, (12), 812.

162. Park, S. E.; Shrout, T. R., Ultrahigh strain and piezoelectric behavior in relaxor based ferroelectric single crystals. *J. Appl. Phys.* **1997,** 82, (4), 1804-1811.
163. Wu, Z.; Cohen, R. E., Pressure-Induced Anomalous Phase Transitions and Colossal Enhancement of Piezoelectricity in PbTiO3. *Phys. Rev. Lett.* **2005,** 95, 037601.
164. Nakamura, K.; Oshiki, M., Theoretical analysis of horizontal shear mode piezoelectric surface acoustic waves in potassium niobate. *Appl. Phys. Lett.* **1997,** 71, 3203.
165. Nakamura, K.; Kawamura, Y., Orientation dependence of electromechanical coupling factors in KNbO3. *IEEE Trans. Ultrason. Ferroelectr. Frequ. Control* **2000,** 47, (3), 750-755.
166. Nakamura, K.; Tokiwa, T.; Kawamura, Y., Domain structures in KNbO3 crystals and their piezoelectric properties. *J. Appl. Phys.* **2002,** 91, (11), 9272-9276.
167. Davis, M.; Damjanovic, D.; Setter, N.; Rytz, D., Domain-engineering of [001]c-oriented KNbO3 and Li-modified (K0.5Na0.5)NbO3 by electrical and mechanical poling. *yet to be published*.
168. Hirohashi, J.; Yamada, K.; Kamio, H.; Uchida, M.; Shichijyo, S., Control of specific domain in KNbO3 single crystals by differential vector poling method. *J. Appl. Phys.* **2005,** 98, 034107.
169. Wada, S.; Seike, A.; Tsurumi, T., Poling Treatment and Piezoelectric Properties of Potassium Niobate Ferroelectric Single Crystals. *Jap. J. Appl. Phys.* **2001,** 40, (9B part 1), 5690-5697.
170. Daglish, M., A dynamic method for determining the pyroelectric response of this films. *Integr. Ferroelectrics* **1998,** 22, 473-488.
171. Hollenstein, E.; Damjanovic, D.; Setter , N., Temperature stability of the piezoelectric properties of Li-modified KNN ceramics *J. Eur. Ceram. Soc.* **2007,** 27, 4093-4097.
172. Deshmukh, K. G.; Ingle, S. G., Interferometric studies of domain structures in potassium niobate single crystals. *J. Phys. D: Appl. Phys.* **1971**, (1), 124.
173. Lian, L.; Chong, T. C.; Kumagai, H.; Hirano, M.; Taijing, L.; Ng, S. C., Temperature evolution of domains in potassium niobate single crystals. *J. Appl. Phys.* **1996,** 80, (1), 376-381.

174. Ingle, S. G.; Dutta, H. S.; David, A. P., Domain wall nucleation by impurity ions in KNbO3 single crystals. *J. Appl. Phys.* **1988,** 64, (9), 4640-4645.
175. Wiesendanger, E., Domain structures in orthorhombic KNbO3 and characterisation of single domaincrystals. *Czech. J. Phys. B* **1973,** 23, 91-99.
176. Chen, K.; Xu, G.; Yang, D.; Wang, X.; Li, J., Dielectric and piezoelectric properties of lead-free 0.95(K0.5Na0.5)NbO3–0.05LiNbO3 crystals grown by the Bridgman method. *J. Appl. Phys.* **2007,** 101, 044103.
177. Polak, J.; Hench, L., Gene Therapy Progress and Prospects: In tissue engineering. *Gene Ther.* **2005,** 12, 1725-1733.
178. Hench, L. L., Bioceramics: From Concept to Clinic. *J. Am. Ceram. Soc.* **1991,** 74, (7), 1487-1510.
179. Hench, L. L., Bioceramics. *J. Am. Ceram. Soc.* **1998,** 81, 1705-1728.
180. Bansiddhi, A.; Sargeant, T. D.; Stupp, S. I.; Dunand, D. C., Porous NiTi for bone implants: A review. *Acta Biomater.* **2008,** 4, 773-782.
181. Kisi, E. H.; Piltz, R. O.; Forrester, J. S.; Howard, C. J., The giant piezoelectric effect: electric field induced monoclinic phase or piezoelectric distortion of the rhombohedral parent? *J. Phys: Cond. Matter* **2003,** 15, 3631-3640.
182. Hlady, V.; Ho, C.-H., Human Low Density Lipoprotein (LDL) and Human Serum Albumin (HSA) Co-Adsorption Onto the C18-Silica Gradient Surface. *Mat.-wiss Werkstofftech* **2001,** 32, 185-192.
183. Morgenthaler, S.; Zink, C.; Spencer, N. D., Surface-chemical and -morphological gradients. *Soft Matter* **2008,** 4, 419-434.
184. Elwing, H.; Glander, C.-G., Protein and detergent intercation phenomena on solid surfaces with gradients in chamical composition. *Adv. Colloid Interface Sci.* **1990,** 32, 317-339.
185. Gunawan, R. C.; Silvestre, J.; Gaskins, H. R.; Kenis, Paul J. A. ; Leckband, D. E., Cell Migration and Polarity on Microfabricated Gradients of Extracellular Matrix Proteins. *Langmuir* **2006,** 22, 4250-4258.
186. Zhuang, Z. Q.; Haun, M. J.; Jang, S. J.; Cross, L. E., Low temperature dielectric, piezoelectric and elastic properties of pure (unpoled) PZT ceramics. *IEEE* **1986**.
187. Sajin, G.; Petrescu, D.; Sajin, M.; Craciunoiu, F.; Gavrila, R., Interactions between Biological Media and Piezoelectric Ceramic in Micromixing Applications. *Bomanian J. Info. Sci. Tech.* **2007,** 10, (3), 279-289.

188. Chu, T.-M. G.; Halloran, J. W.; Hollister, S. J.; Feinberg, S. E., Hydroxyapatite implants with designed internal architecture. *J. Mater. Sci.: Mater. Med.* **2001,** 12, 471-478.

189. Cruz, F.; Colle, T.; Bocking, C.; simoes, J., Selective laser sintering of customised medical implants using biocomposite materials. *Tehnicki Vjesnik* **2003,** 10, (2), 23-27.

190. Inkster, C. F.; Ng, S. G. J.; Leatherbarrow, B., Primary Banked Scleral Patch Graft in the Prevention of Exposure of Hydroxyapatite Orbital Implants *Ophthamology* **2002,** 109, (2), 389-391.

191. Ruys, A. J.; Wei, M.; Sorrell, C. C.; Dickson, M. R.; Brandwood, A.; Milthome, B. K., Sintering effects on the strength of hydroxyapatite. *Biomaterials* **1995,** 16, 409-415.

192. Nagai, M.; Shibuya, Y.; Nishino, T.; Saeki, T.; Owada, H.; Yamashita, K.; Umegaki, T., Electrical conductivity of calcium phosphate ceramics with various Ca/P ratios. *J. Mater. Sci.* **1991,** 26, 2949-2953.

193. Ruys, A. J.; Sorrell , C. C.; Brandwood, A.; Milthorpe, B. K., Hydroxyapatite sintering characteristics: correlation with powder morphology by high-resolution microscopy. *J. Mater. Sci. Lett.* **1995,** 14, 744-747.

194. Bett, J. A. S.; Christner, L. G.; Hall, W. K., Studies of the Hydrogen Held by Solids. XII. Hydroxyapatite Catalysts. *J. Am. Chem. Soc.* **1967,** 89, 5535-5541.

195. Damjanovic, D., Comments on origins of enhanced piezoelectric properties in ferroelectrics. *IEEE Trans. Ultra. Ferro. Freq. Control* **2009,** 56, (8), 1574-1585.

196. Lee, T.; Kwok, K. W.; Li, H. L.; Chan, H. L. W., Lead-free alkaline niobate-based transducer for ultrasonic wirebonding applications. *Sensor and Actuator A* **2009,** 150, 267-271.

197. Li, E.; Kakemoto, H.; Hoshina, T.; Tsurumi, T., A Shear-Mode Ultrasonic Motor Using Potassium Sodium Niobate-Based Ceramics with High Mechanical Quality Factor. *Jap. J. Appl. Phys* **2008,** 47, (9), 7702-7706.

198. Snook, K. A.; Zhang, S.; Shrout , T. R., Lead Free Piezoelectric Ceramics for Medical Ultrasound Transducers. *Proc. IEEE Ulatrasonic Symposium* **2006,** 1, (4151955), 351-354.

List of publications

N. Klein, D. Damjanovic, N. Setter, B. Wiley-van Eerd, J. Trodahl, BNT-BT phase diagram examined by Raman spectroscopy, to be submitted (2009)

N. Klein, A. Lesman, S. Levenberg, D. Damjanovic, Preliminary biocompatibility tests of KNLN and PZT ceramics, submitted (2009).

H. J. Trodahl, N. Klein, D. Damjanovic, N. Setter, B. Ludbrook, D. Rytz, M. Kuball, Raman spectroscopy of $(K,Na)NbO_3$ and $(K,Na)_{1-x}Li_xNbO_3$, *Appl. Phys. Lett,* vol. 93, (2008), pp. 262901

Y. Wang, D. Damjanovic, N. Klein, N. Setter, High-Temperature Instability of Li- and Ta-Modified $(K,Na)NbO_3$ Piezoceramics, *J. Am. Ceram. Soc*., (2008), pp. 1-9

N. Klein, E. Hollenstein, D. Damjanovic, H. J. Trodahl, N. Setter, M. Kuball, A study of the phase diagram of $(K,Na,Li)NbO_3$ determined by dielectric and piezoelectric measurements, and Raman spectroscopy, *J. Appl. Phys*, vol. 102, (2007), pp. 014112

M. Davis, N. Klein, D. Damjanovic, N. Setter, A. Gross, V. Wesemann, S. Vernay, D. Rytz, Large and stable thickness coupling coefficients of <001>C-oriented $KNbO_3$ and Li-modified $(K,Na)NbO_3$ single crystals, *Appl. Phys. Lett*, vol. 90, (2007), pp. 062904

Y. Wang, D. Damjanovic, N. Klein, E. Hollenstein, N. Setter, Compositional Inhomogeneity in Li- and Ta-Modified $(K,Na)NbO_3$ Ceramics, *J. Am. Ceram. Soc.*, vol. 1–5, (2007)

Curriculum Vitae

Name: Naama Klein

Date of birth: 3rd of May, 1980

Nationality: Israeli

Education

2005-2009 Ph.D student and assistant at Ceramics Laboratory
Doctoral School of Materials Science, EPFL, Switzerland

2000-2005 B.Sc and B.A in materials engineering and chemistry
Materials Engineering Faculty, Technion, Israel

Industrial experience

2002-2005 Student position, Israel
R&D in boron carbide ceramics for shielding

Awards

2008 One of six best works in the 9th European Conference on Applications of Polar Dielectrics

Languages

Hebrew Mother tongue

English Fluent in writing and speaking

French Intermediate knowledge